Semiconductor ring lasers

by
Andrzej Florentyn Jezierski, M.Eng.

A Thesis
submitted to the Faculty of Engineering
of the University of Glasgow
for the degree of
Doctor of Philosophy

Your hearts know in silence the secrets of the days and the nights.
But your ears thirst for the sound of your heart's knowledge.
Say not, "I have found the truth," but rather, "I have found a truth."

The Prophet by Kahlil Gibran

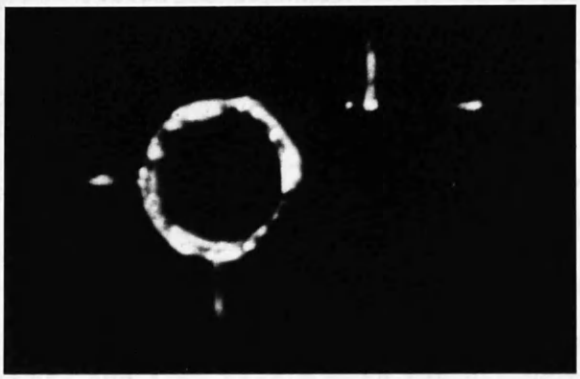

Dla Mamy, Taty, Ani, Teresy i Eli

ACKNOWLEDGEMENTS.

I wish to express my appreciation to Professor John Lamb for providing me with the facilities of the Department of Electronics and Electrical Engineering and for his supervision during the initial year of my research. I thank my supervisor, Professor Peter J R Laybourn for his advice, guidance, encouragement, friendship and sailing expeditions. I would also like to thank Professor Richard M De La Rue for his supervision in Professor Laybourn's absence, for his active interest, discussions and hillwalking trips.

I am indebted to Professor Chris D W Wilkinson, Professor Stephen P Beaumont, Dr Gordon Doughty, Dr Stephen Thoms, Dr John Davies, Dr Mary O'Neil, Dr John H Marsh, Dr Charles N Ironside and Dr Clivia M Sotomayor-Torres for useful discussions and enthusiastic assistance. I thank also Professor Lawrence Challis and Dr Mike Heath from the University of Nottingham for the encouragement and patience in waiting for the final outcome of my work.

I am grateful for the help and company of Jimmi Young, George Boyle, Ray Hutchins, Dave Gourlay and Andy Stark, who tought me the art of processing. Thanks also for the discussions and technical support provided by other members of the technical staff, in particular David Clifton, Tom Wright, Ray Harkins, Kazimierz Piechowiak, Harry Anderson, John Cochrane, Douglas Mackintyre, Ann MacKinnon, Bill Monaghan, and Roy Turnbull. Other members of the academic and technical staff whose help was particularly appreciated are Dr John Richter, Dr David Muir, Lois Hobbs, Ray Darkin and Lawrence Bradley.

I am grateful to Dr Colin Stanley, Dr Nigel Johnson, Dr Alistair Kean, Dr John Roberts and Dr Nigel Mason from the epitaxial growth groups in Glasgow and Sheffield Universities, and to Dr Rick Glew from STC Technology for providing the materials on which the devices were made.

The analysis of the optical waveguides was aided by Professor Peter Laybourn, Kam Lee, Bhindi Bhumbra and Azan Kassim with the use of their modelling software. The analysis of the semiconductor properties was supported by Jeremy Pepin and Wei Chen with their software. The damage of the dry etching was assesed with the help of Mohammed Rahman.

Ken Thomas, Clive Reeves, Jim Adams, Kim Lee, Wei Chen, Rebecca Cheung, Michal Kaminski, Kam Lee and Tin Cheng shared their time with me on useful discussions and gave me friendship. All the members of the Polish folk-dance group, Rysy, and Father Marian Lekawa taught me how to make life interesting. Ian Thayne, David Halliday, Daniel Lau, Bhindi Bhumbra, Alistair Meney, Jennifer Bates, Ivair Gontijo, Andy Jennings, Mohammed Rahman, Thomas Krauss and other mates stood by me, all shared similar anxieties while we studied and made my stay in Glasgow enjoyable. Thanks also to auntie Maria Czajkowska, Ann Laybourn, Rosemary Young, Colin Matthews, Tin Cheng, Allen Page, Trevor Benson, Mike Barlow, Douglas Halliday, Penny Gowland, Mark McJury, Philip Hawker, Jonathan Sharp, John Middleton, Stuart Hawksworth, and others for helping hands and for making life in Nottingham pleasurable.

Financial support was provided by the IEE through a Robinson Research Fellowship, and the Lucas Research Centre, where my industrial supervisors were Cy Hughes and Roger Merryweather.

Finally, my warmest thanks to my family and my girlfriend, Ela, for being...

ABSTRACT.

Miniature rib ring waveguide and pill−box laser structures as small as 12μm in diameter were investigated. Output stripe waveguides were coupled to the rings via Y−junctions. Optical properties of the component structures were analysed using the finite difference method. The original waveguides were defined in GaAs/ AlGaAs heterostructure materials by reactive ion etching through the pattern of the guide contacts with the connected bonding pads. The fabrication was then simplified by embedding the etched guides in polyimide and overcoating with a gold bonding layer. Temperature stable ohmic contacts were designed to improve the stability of the devices. Material designed with a localised gain region quantum well and an additional coupled passive guide provided single mode operation even for the broad area devices. The performance of the rib ring laser structures was comparable to that of similar size straight lasers. Standard structures defined by optical lithography in DH and QW materials lased successfully. E−beam defined devices with successively narrower ribs down to 0.4μm, and shorter ring cavities down to 12μm in diameter, increased the optical loss. This resulted in increased threshold density up to 220kA/ cm^2 for ring lasers made of DH material, and a lack of lasing for small structures made of QW material, where the relation is more critical. The QW devices showed evidence of both first and second quantised state operation. This type of ring laser structure is suitable for use as a light source in monolithic integrated optics, although absorption loss due to the gold bonding layer must be eliminated to reduce threshold current of the devices.

INTRODUCTION TO RING RIB LASERS.

An optical gain region within a chosen forward biassed p– n semiconductor junction, configured to form a resonator, provides optical oscillation and lasing action. Commonly, the feedback mechanism is formed by cleaving the crystal in two parallel {110} planes, perpendicular to the required <110> lasing direction lying in a {100} plane. This puts a constraint on the incorporation of semiconductor lasers with other integrated optical devices in a monolithic optical circuit, where the laser is formed on a much larger substrate. Various solutions have been proposed [Merz– 1]: a single– frequency laser source with distributed feedback (Bragg reflection) is an example, but involves problems concerned with producing very fine and accurate gratings over a large area and subsequent material regrowth. If lasing is confined to a stripe waveguide structure with strong lateral guiding, the waveguide may be formed in a continous ring and thus eliminate the need for any other optical feedback mechanism [Matsumoto– 2, Liao– 3, Wang– 4]. The waveguide ring laser can be fabricated at the same time as other waveguide structures on the semiconductor substrate. The optical power can be extracted from the resonator via a Y– junction to the output branching waveguide. As an alternative to rings with smooth waveguide bends, polygonal structures may be employed with reflecting facets redirecting the guided light at the corners [5].

We have been investigating the design, preparation and experimental properties of resonant ring waveguide structures to be used as laser cavities in GaAs/GaAlAs heterostructure material, where the need for high quality mirrors is eliminated and the influence of the laser output termination is low. The lasers could be produced together with the output guide, by relatively straightforward planar technology at any location in a monolithic integrated optical circuit [Jezierski– 5, Jezierski– 6]. The performance of the ring lasers that were fabricated was comparable with that of similar– sized straight lasers.

The optical guides existing within the semiconductor ring lasers are discussed in section 1. The analysis of the properties of the complex ring resonator with a Y– junction coupler required the investigation and optimisation of simpler structures. These were: slab guide, straight stripe guide, curved guide and both directional and Y– junction guide couplers. The finite difference method was used to evaluate local normal modes available within some of the structures. Losses of the structures were discussed. The use of low loss materials and high quality pattern definition are not sufficient to produce low– loss devices. In addition, within the directional coupler a

low index step between the guides and the cladding media will be needed if the guide separation and widths are not to be too narrow. Most of the losses within other devices could be considerably reduced with strong confinement, allowing only a small proportion of the decaying field to travel outside the guide. High index step and adequately wide guides are thus required to produce low–loss devices. The resonators with Y–junction output guides introduce contra–rotating oscillations within the ring and additionally require the ring guide being wider than the output guide, to reduce loss of the Y–junction in the constructive direction and eliminate the domination of the unused oscillations.

The investigations into the various designs of the light and carrier confinement region within the materials used for the ring lasers has been pursued and the threshold current conditions of the resulting structures are discussed in section 2. This includes a double heterostructure, a localised gain region separate confinement quantum well material and a structure with an additional passive guide directionally coupled to the lasing region. Strong light and carrier confinements with high index steps and optimised width of the structures may improve light–carrier interaction and thus reduce threshold density of the final devices. Reduced confinement, increased loss and reduced cavity length, produce almost proportional increases in the threshold current density of a double heterostructure laser, and almost exponential, within a quantum well device. Materials were designed and grown, and then evaluated by measuring the properties of the manufactured broad area lasers. The optimised structures resulted in lasers with threshold current densities down to $400A/cm^2$ for a 7.6nm quantum well material, with a closed optical path of $800\mu m$. The shorter devices increased the threshold current, and quantum well lasers with a closed path shorter than $220\mu m$ were not able to lase. Laser material with an additional coupled passive guide restricted the oscillation conditions, resulting in single mode operation of the broad area lasers produced, while other structures operated in multimode operation.

The fabrication processes for ring lasers have been investigated and optimised, from the wafer to a ready packaged device (section 3). Cleaning determined the quality of all the further processes. High quality smooth ring patterns of $0.4\mu m$ wide stripes were obtained using electron–beam lithography; photo–lithography was used for devices wider than $2\mu m$. Deposition of thin insulator and contact films and their annealing were examined. Spinning of liquid insulators allowed coverage of the high ratio pattern, with a reduced thickness on the top of the pattern. The reliability of the final devices was improved with the development of a stable ohmic contact

between metal and semiconductor, capable of operation at 350°C. The development of a controlled annealer allowed for the optimised annealing parameters for each ohmic contact composition. A contact composition producing ohmic contacts to both n– and p–type GaAs, thus reducing the number of metallisation steps, was developed. Wet chemical etching was used to selectively remove various layers, produce a recess or remove damage. Selective anisotropic etching of the devices through the ohmic contact pattern was performed using reactive ion etching with $SiCl_4$, while the insulator was etched using plasma etching with oxygen. High aspect ratio, low damage, smooth surface patterns down to 0.4μm wide, 7μm deep and 400μm long incorporating a ring laser structure were successfully produced. Cleavage of a wafer supporting a fragile pattern into separate devices was successfully studied. Finally, packaging, improving strength of the device and heat dissipation, were investigated.

Various stripe rib ring lasers with Y–junction coupled output guides were designed, manufactured and tested (section 4). The strong confinement used should result in an acceptable loss in the bend structures considered. Nevertherless, the practical ring lasers with smaller radii increased the threshold current density, probably due to the short cavity length. This was highly aggravated within rib guides narrower than 3 to 4μm. With a decreased guide width, a considerable part of the light travels outside the guide, being susceptible to scattering loss on the guide boundary and absorption loss in the outside medium. The threshold current density dependence on loss of the devices made in DH material is almost linear and even very lossy short cavities (12μm diamater) and narrow guides (1μm) were observed to lase, although at a threshold density increased from 1.7 to 220kA/cm^2. Much stronger, almost exponential dependence within the devices made in QW material prevented the lasing action within similar structures. Second quantised state operation was observed for high–loss QW lasers, while peaks of the spectra corresponding to both first and second state operation were visible for excessively lossy, non–lasing QW structures.

The investigations into the ring laser are summarised in section 5 and future work is proposed in section 6.

REFERENCES.

[1] Merz J.: Monolithic integration of optical sources and detectors, Proc.SPIE, Vol.239, pp.53–60 (1980).

[2] Matsumoto N., Kawaguchi H., Kumabe K.: Oscillation characteristics of semiconducor lasers with circular waveguides, Proc.IOOC'77, B1.2, pp.189–192

(1977).

[3] Liao A.H., Wang S.: Semiconductor injection lasers with a circular resonator, Appl.Phys.Lett., Vol.36, pp.801–803 (1980).

[4] Wang S, Choi H.K., Fattah I.H.A.: Studies of semiconductor lasers of the interferometric and ring types, IEEE JQE, Vol.18, pp.610–617 (1982).

[5] Jezierski A.F., Laybourn P.J.R.: Integrated semiconductor ring lasers, IEE Proc., Vol.135, pt.J. (1), pp.17–24 (1988).

[6] Jezierski, A.F. Laybourn, P.J.R.: Polyimide–embedded semiconductor ring lasers, 5th European Conference on Integrated Optics, Paris, Paper no.3 (1989). Published in proceedings of SPIE, 1141, pp.7–11 (1989).

1. OPTICAL GUIDING WITHIN THE RING LASER DEVICES.

1.0. INTRODUCTION.

A laser device may be considered as an active waveguide, using an interaction of emitted light and carriers, to stimulate the emission of further photons. Strong optical confinement within the guide improves the lasing properties.

Various optical structures were investigated in order to understand the complexity of the ring laser system, with a Y– junction branching output waveguide (fig.1.1). A directional coupler from a lasing region to a closely positioned passive waveguide was also considered as another method of coupling out light resonating within the ring. The finite difference method (section 1.3) was used to evaluate field distribution within various structures and the spread of light away from the guide. Confinement increased with a higher index step. The optimal width of the guide was chosen where the field spreading was least. The properties of the laser materials may be established by analysis of two–dimensional broad area devices, representing a slab optical waveguide. A stripe laser is represented by a stripe guide structure. The ring configuration with the branching straight output guide requires investigations into both bent and straight guides. The bent guide enables redirection of the optical beam, making integration of the optical devices easier, and allows for the formation of a circular optical resonator. Coupling of the optical power out of the resonator to the output waveguide may be achieved via a Y– junction, which at the same time redirects and splits the power of the optical modes available within the circuit. For coupling purposes, directional coupling to the closely positioned guide may also be used. The experimental results of the above structures are presented in sections 2.4 and 4. Losses of the structures were studied. They are determined by the quality of materials used, definition of the guides and a spread of the light away from the guide to other, absorbing regions. Most of the losses were found to reduce with strong light confinement, achieved with a high index step and adequately wide guides. In addition, the resonator guide should be wider than the output guide for constructive oscillations.

Throughout this section, the waveguiding properties of a laser structure lasing at a wavelength of 0.844μm are described. The laser is produced from a material incorporating a 7.6nm wide GaAs well sandwiched between two layers of $Al_{.25}Ga_{.75}As$ of 105nm each, subsequently sandwiched between two 1.5μm thick layers of $Al_{.6}Ga_{.4}As$ (fig.1.2) (section 2). The final device can be made using etched

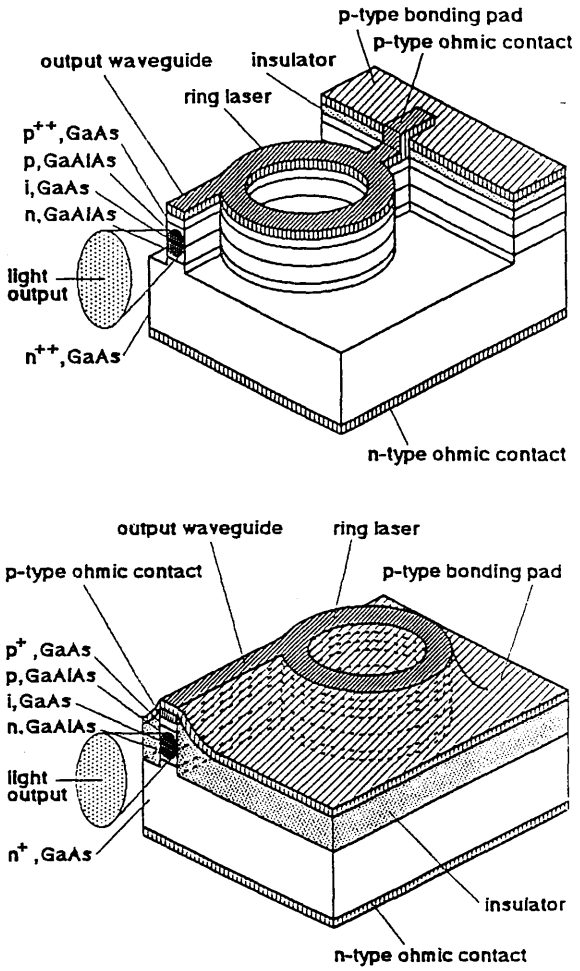

Fig.1.1. Rib ring laser and polyimide embedded ring laser.

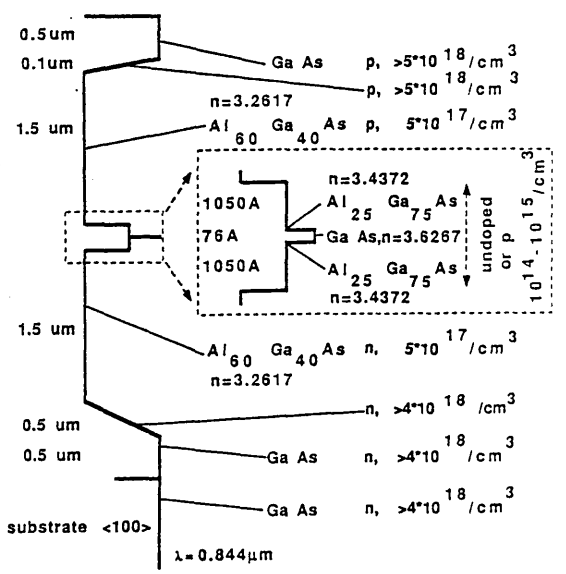

Fig.1.2. Quantum well laser material providing strong optical, carrier and power confinement.

rib waveguides 1 to 10μm wide, surrounded with air or polyimide, and bent to form the ring resonator and Y– junction section (fig.1.1). The structure can be represented by a guiding region 0.2176μm wide and with refractive index of 3.44 sandwiched between the 1.5μm thick cladding regions of refractive index 3.26, formed into a rib and surrounded with a material of refractive index 1 (air) or 1.614 (polyimide).

1.1. SLAB LASER WAVEGUIDE.

A simple planar waveguide, representing a broad area laser device, consists of a layer of constant refractive index n_a sandwiched between two layers of a lower refractive index n_{c1} and n_{c2} (fig.1.3). According to ray–optical theory [Tien–1, MacBean–2, Kogelnik–3], the light travels within the central region in a zig–zag path and is reflected from the boundaries with the cladding layers. Total internal reflection requires the conditions [Laybourn–4]:

$$Q > \sin^{-1}(n_{c1}/n_a) \text{ and } Q > \sin^{-1}(n_{c2}/n_a) \qquad (1.1)$$

Example: $n_{c2}=3.26$, $n_a=3.44 \rightarrow Q > 71^o$

The propagation constant β of the mode along the waveguide and in the perpendicular direction k_a are defined [MacBean–2]:

$$\beta = \frac{2*\pi}{\lambda_o} * n_a * \sin Q = k_o * n_{eff} \qquad (1.2)$$

$$k_a = \frac{2*\pi}{\lambda_o} * n_a * \cos Q = \sqrt{(k_o^2 * n_a^2 - \beta^2)} = k_o * \sqrt{(n_a^2 - n_{eff}^2)} \qquad (1.3)$$

where: $k_o = \frac{2*\pi}{\lambda_o}$ is the free space wave number, (1.4)

n_{eff} is the effective refractive index,

$$n_c < n_{eff} < n_a \qquad (1.5)$$

The guiding conditions require that the total phase change in the perpendicular direction, that is the path phase change $2*k_a*d$ and the phase changes due to reflections at the interfaces ($2*Q_{c1,a} + 2*Q_{c2,a}$), equal $2*m*\pi$:

$$2*k_a*d - 2*Q_{c1,a} - 2*Q_{c2,a} = 2*m*\pi \qquad (1.6)$$

where: m= 0, 1, 2...

and d is the thickness of the active layer.

The values of the propagation constant of subsequent modes are discrete. The equation (1.6) may be presented in a different form, enabling a determination of the

propagation contant β and the effective refractive index n_{eff} of the waveguide from the refractive indexes of the active layer n_a, cladding layers n_{c1}, n_{c2} and the thickness of the central layer d [Marcatilli– 5]:

$$2*k_a*d = 2*\tan^{-1}(Y_{c1}*\frac{k_{c1}}{k_a}) + 2*\tan^{-1}(Y_{c2}*\frac{k_{c2}}{k_a}) + 2*m*\pi \quad (1.7)$$

where: m=0,1,2...

Y=1 for TE mode, $Y=(n_a/n_c)^2$ for TM mode, (1.8)

$$k_c = k_o * \sqrt{(n_{eff}^2-n_c^2)} \quad (1.9)$$

The n_{eff} may be computed by scanning its value and calculating the corresponding thickness $d(n_{eff})$ until the value is the same as in the required guide. High accuracy of the refractive index must be known to satisfy the equations for more complex, two dimensional structures. Examples are calculated in Table 1.1.

Table 1.1. Effective refractive indexes and propagation constants of the guides described in section 1.0 (fig.1.2) operating at a wavelength of $\lambda = 0.844\,\mu m$.

n_a	n_c	d μm	n_{eff}	k_a μm^{-1}	k_c μm^{-1}
3.443854	3.261709	0.2176	3.336863	6.34608787	5.242500154
3.443854	1.0	1.0	3.4184329	3.11997266	7.617244236

In practice, the optical wave is bound to the waveguide and travels both within the active and cladding layers (fig.1.4). The wave equation, representing the local normal mode within the cross–section of the slab waveguide, must describe the wave within each of the waveguide regions and satisfy the boundary conditions [Marcatilli– 5, Wilkinson– 6]:

$$\frac{\delta^2 E_y}{\delta x^2} - (\frac{2*\pi}{\lambda_o})^2*(n_{eff}^2-n_{a,c1,c2}^2)*E_y = 0 \quad (1.10)$$

$$E_y(x\to-\infty) = E_y(x\to+\infty) = 0 \quad (1.11)$$

$$E_y(x\to0^-) = E_y(x\to0^+) \quad (1.12)$$

$$E_y(x\to-d^-) = E_y(x\to-d^+) \quad (1.13)$$

$$\frac{\delta E_y}{\delta x}(x\to0^-) = \frac{\delta E_y}{\delta x}(x\to0^+) \quad (1.14)$$

$$\frac{\delta E_y}{\delta x}(x\to-d^-) = \frac{\delta E_y}{\delta x}(x\to-d^+) \quad (1.15)$$

The solutions of the equation 1.10 take the form of exponentials within the cladding layers and of sines/cosines within the active layer [Wilkinson– 6]:

$$E_y = A * \exp(-k_{c1}*x), \text{ within the first, cladding layer,}$$
$$= D * \exp(-k_{c2}*(d-x)), \text{ within the third, cladding layer}$$
$$= B * \cos(-k_a*x) + C * \sin(-k_a*x), \text{ within the second, active layer,} \quad (1.16)$$

where: A, B, C, D are constants.

By shifting the position of the x axis to the central point of the active layer (fig.1.4), for symmetric waveguides, the solutions of the equation 1.10 for the zero order mode are simplified to:

$$E_y = B_1 * \cos(k_a*x), \text{ for: } -0.5*d \leqslant x \leqslant 0.5*d,$$
$$= A_1 * \exp(-k_c*(x-0.5*d)), \text{ for: } x \geqslant 0.5*d,$$
$$= A_1 * \exp(-k_c*(-x+0.5*d)), \text{ for: } x \leqslant -0.5*d. \quad (1.17)$$

Let: $B_1=1$, then at $x=0.5*d$,

$$A_1=\cos(k_a*0.5*d)=\cos\left(\frac{2*\pi}{\lambda_o}*\sqrt{(n_a^2-n_{eff}^2)}*0.5*d\right)$$

finally:

$$E_y = \cos\left[\frac{2*\pi}{\lambda_o}*\sqrt{(n_a^2-n_{eff}^2)}*x\right], \text{ for: } -0.5*d \leqslant x \leqslant 0.5*d,$$

$$= A_1 * \exp\left[\frac{-2*\pi}{\lambda_o}*\sqrt{(n_{eff}^2-n_c^2)}*(x-0.5*d)\right], \text{ for: } x \geqslant 0.5*d,$$

$$= A_1 * \exp\left[\frac{-2*\pi}{\lambda_o}*\sqrt{(n_{eff}^2-n_c^2)}*(-x+0.5*d)\right], \text{ for: } x \leqslant -0.5*d \quad (1.18)$$

Example (fig.1.2):
For the guide of $n_c=3.26$, $n_a=3.44$, $d=0.22\mu m$
→ $n_{eff}=3.34$, $k_a=6.13\mu m^{-1}$, $k_c=5.41\mu m^{-1}$, $B_1=1$, $A_1=0.78$ and the equations are (fig.1.4):

$$E_y = \cos(6.13*x), \text{ for: } -0.11 \leqslant x \leqslant 0.11,$$
$$= 0.78 * \exp(-5.41*(x-0.11)), \text{ for: } x \geqslant 0.11,$$
$$= 0.78 * \exp(-5.41*(-x+0.11)), \text{ for: } x \leqslant -0.11.$$

where x is in μm. (1.19)

Guides which are narrow or have a small refractive index step, result in a large spread of the light into the cladding regions. A guide which is too wide, or with a high refractive index step, may promote multimode operation.

Calculations using the above equations enabled evaluation of various waveguides and resulted in the design of high quality laser material structures (e.g. figs.1.2) (section 2). More complex solutions of two-dimensional guides are considered in section 1.3 by calculations using a finite difference method.

1.2. STRIPE LASER WAVEGUIDE.

Stripe lasers are the structures which form the basis of ring configuration, discussed in this work. Let us first consider a simple straight stripe laser waveguide. Practical devices (fig.1.1) use vertical confinement supporting a single mode only, while the lateral confinement often supports multimode operation. Consequently although practical devices maintain single mode operation at the threshold current (the shortest optical path), excitation of other modes is observed for higher current (section 2.4).

The local normal modes within the stripe waveguides can be modelled by the two perpendicular slab waveguides approximating the original rectangular cross-section. [Marcatilli-5] modelled the stripe waveguide using the two uncoupled corresponding slab waveguides, while [Knox and Toulios-7] modified his theory to couple the two fields by using the effective index method (fig.1.5). This was further improved by [Koshiba and Suzuki-8].

The effective index method (fig.1.5) involves calculation of the propagation constant and the effective refractive index n_{eff1} in the direction with stronger guiding (higher refractive index step), assuming a slab configuration in the orthogonal direction. A second slab guide is then created in a perpendicular direction, with a central layer of refractive index = n_{eff1}. The propagation constant and the effective refractive index n_{eff2} of this structure approximate the original rectangular waveguide. Note that being mutually perpendicular, one of the solutions is for a TM mode and the other for a TE mode.

The stripe waveguide problem may be solved using numerical computer analysis, using for example a finite difference method.

1.3. FINITE DIFFERENCE METHOD FOR LASER WAVEGUIDE CALCULATIONS.

The propagation of an electromagnetic wave within the dielectric stripe laser waveguide can be numerically calculated by replacing the wave equation with a finite

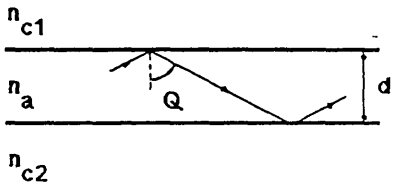

Fig.1.3. Slab waveguide.

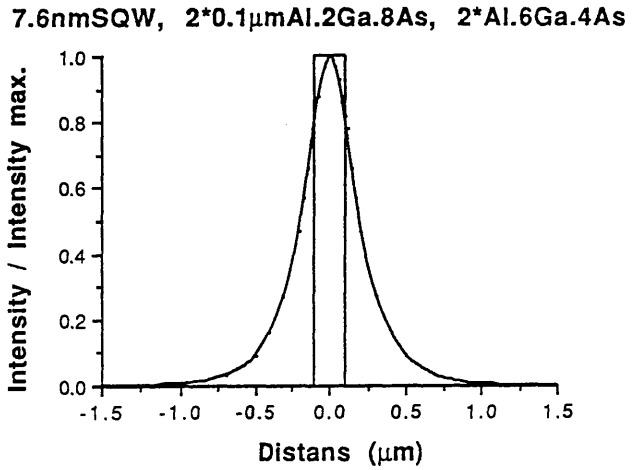

Fig.1.4. Field distribution of the wave travelling within the slab waveguide presented in fig.1.2. ($\lambda = 0.844\mu m$)

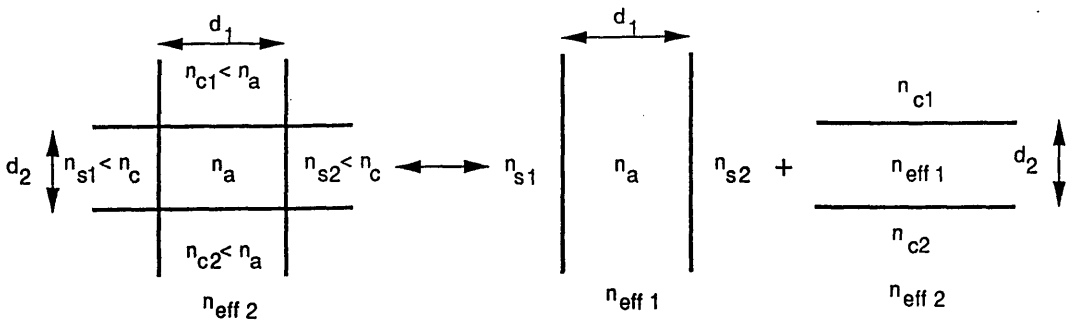

Fig.1.5. Representation of a rectangular guide by two perpendicular slab guides using an effective refractive index method.

difference relation at discrete mesh points. The program calculates the effective index of the waveguide by iteration and field overwriting [Benson– 9]. The shape of the guide is introduced by assigning refractive index values to the matrix mesh points. The boundary conditions at the walls must be considered to avoid significant errors [Lee– 10].

The initial default field values assigned to the matrix can be practically set to any values. The calculations of the propagation constants and the effective refractive indices are followed by the calculations of the mesh point field distribution of the two perpendicular substitutional slab guides and their multiplication to produce the initial guess for the field within the stripe guide. A better approximation of the effective refractive index is then calculated and the field is recalculated using the finite difference expression of the wave equation [Benson– 9], where the discrete values of each point depend on the values of the neighbouring points. The new field determines a new refractive index, that forces the field to be changed again and the process is continued until the change of the effective refractive index is smaller than the tolerance:

$$\frac{N_{effnew}-N_{effold}}{N_{effnew}} < \text{Tolerance} \qquad (1.20)$$

The two dimensional wave equation is [Marcatilli– 6]:

$$\frac{\delta^2 E_y}{\delta x^2} + \frac{\delta^2 E_y}{\delta y^2} + k_o{}^2*(n^2-n_{eff}{}^2)*E_y = 0 \qquad (1.21)$$

The finite difference expression of the wave equation (1.20) for most of the points is:

$$E(I,J) = \frac{\dfrac{E(I+1,J)+E(I-1,J)}{\Delta X^2} + \dfrac{E(I,J+1)+E(I,J-1)}{\Delta Y^2}}{\dfrac{2}{\Delta X^2} + \dfrac{2}{\Delta Y^2} - k_o{}^2*(N^2(I,J)-N_{eff}{}^2)} \qquad (1.22)$$

since:

$$\delta E_y/\delta x = \frac{E(I+1,J)-E(I,J)}{\Delta X} - \frac{E(I,J)-E(I-1,J)}{\Delta X} \qquad (1.23)$$

$$\delta^2 E_y/\delta x^2 = \frac{E(I+1,J)+E(I-1,J)-2*E(I,J)}{\Delta X^2} \qquad (1.24)$$

where: ΔX, ΔY are the mesh distances in x and y directions,
N(I,J) is the refractive index at the point (I*ΔX,J*ΔY),
N_{eff} is the effective refractive index.

The function takes different values near the boundaries of the structure. The analysis of symmetrical structures is often limited to those parts which are unique. Additional corrections are then needed [Lee−10] to define the values on those boundaries of the matrix and their corners, requiring "mirrors", while other boundaries are usually forced to zero (fig.1.6).

The effective refractive index N_{eff} (1.21, 1.22) is created by summing the entire field matrix of the expression [Benson−9].The index N_{eff} should increase and improve as the trial function for E_y approaches the actual mode distribution.

$$n_{eff} \geq \left[\frac{\iint_{\text{cross-section}} (\delta^2 E_y/\delta x^2 + \delta^2 E_y/\delta y^2 + k_o^2 * n^2 * E_y) * E_y dxdy}{k_o^2 * \iint_{\text{cross-section}} E_y^2 dxdy} \right]^{1/2} \qquad (1.25)$$

For most of the points:

$$N_{eff} \geq \left[\frac{\sum_{ji} [\{E1 + E2 + k_o^2 * (N^2(I,J) * E(I,J))\} * E(I,J)]}{k_o * \sum_{ji} E^2(I,J)} \right]^{1/2} \qquad (1.26)$$

where:

$$E1 = \frac{E(I+1,J)+E(I-1,J)-2*E(I,J))}{\Delta X^2} \qquad (1.27)$$

$$E2 = \frac{E(I,J+1)+E(I,J-1)-2*E(I,J))}{\Delta Y^2} \qquad (1.28)$$

The field on the boundaries of the matrix, again, must be considered separately.

The program written by [Lee−10] was modified, by providing the Marcatilli's default field values to speed up the calculations, using a limited number of the mesh points of 50 *150, and was adopted to the specific shapes of the waveguides, by changing the refractive index matrix and the boundary conditions. Stripe rib laser waveguide structures surrounded with air or polyimide (fig.1.1) were modelled, considering zero and first order modes, calculating their effective refractive indexes for each mode, and producing a two or three−dimensional plot of the local normal modes, available within the cross−section of the structure (figs.1.6, 1.7, 1.8). The field distribution of the structure incorporating quantum wells changes very little with the number of wells, due to their narrowness compared to the total guide width.

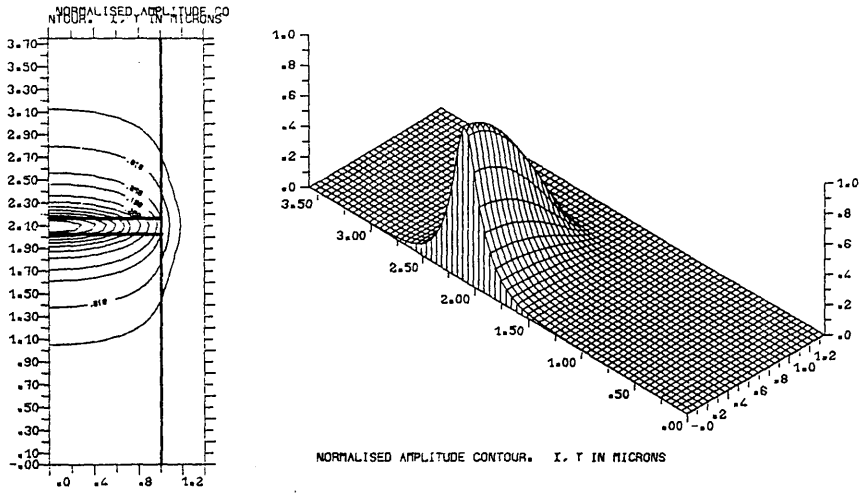

Fig.1.6. Two– and three–dimensional plot of the zero order local normal mode, within a 0.152μm wide waveguide of GaAs (n_c= 3.600886) sandwiched between cladding layers of $Al_{.6}Ga_{.4}As$ (n_c= 3.248774) and surrounded on both sides of the 2μm wide guide with polyimide (n_s= 1.615) (λ= 0.8674597).

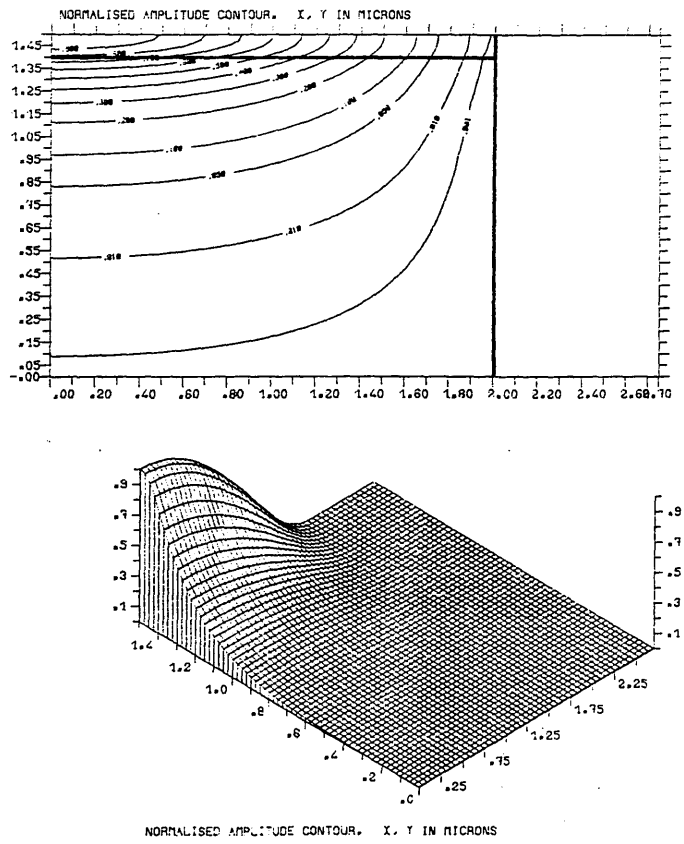

Fig.1.7. Two– and three–dimensional plot of the zero order local normal mode, within a waveguide of 7.6nm wide GaAs well sandwiched between 0.105μm thick layers of $Al_{.25}Ga_{.75}As$ (n_{w+c}= 3.443854), sandwiched in turn between cladding layers of $Al_{.6}Ga_{.4}As$ (n_c= 3.261709) and surrounded on both sides of the 4μm wide guide with polyimide (n_s= 1.615).

The thickness of cladding layers needs to be sufficient to confine most of the light and prevent the light coupling out of the active layer to the absorbing contact layers (see section 1.4). The zero order mode field within an optimised double heterostructure laser material (section 2.1.1) (0.15μm GaAs, 1.5μm $Al_{.6}Ga_{.4}As$ cladding layers) decayed within the cladding layers down to below 0.1% of its peak value within a distance of 1.05μm (fig.1.6). Typical, non-optimised structures (e.g. .2μm GaAs, 2μm $Al_{.2}Ga_{.8}As$) resulted in a decay within the cladding layers to 2% within 1μm and down to below 0.1% within the distance of 1.7 to 1.9μm. A similar observation applies to the quantum well laser material (section 2.1.2), where in an optimised light confinement region (GaAs well, 2*0.1μm $Al_{.25}Ga_{.75}As$ first cladding layers, 2*1.5μm $Al_{.6}Ga_{.4}As$ second cladding layers) the zero order mode field decayed to below 1% of its peak value within a cladding layer distance of 1μm and below 0.1% within a distance of 1.4μm (fig.1.7).

The influence of the width of the optimised quantum well rib guides on the lateral field spread was investigated for air (n=1) or polyimide (n=1.614) surroundings (figs.1.7, 1.8). The proportion of light travelling outside the guide, within the surrounding environment, increases rapidly as the width of the guide is decreased (table.1.2).

Table 1.2. Spread of the light away from the rib waveguide.

1) Zero order mode:

width of the guide (μm)	0.3	0.6	1.0	2.0	4.0
field level on the boundary (%)	35	22	12	7	<0.1
decay length down to 0.1% (μm)	.28	.24	.22	.18	-

2) First order mode:

width of the guide	(μm)		1.0	2.0
field level on the boundary	(%)		90	23
decay length down to 0.1%	(μm)		.6	.26

Within a rib guide of thickness 4μm, the field of the zero order mode decays down to below 0.1% (fig.1.7). Guides narrower than 4μm result in a much smaller field decay within the guide and consequently a much larger fraction of the field travelling in the outside medium (fig.1.8). This may result in a highly increased loss of the wave travelling within narrower guides, due to the outside medium absorption loss and scattering on walls. This was confirmed by the behaviour of 1μm wide rib laser

structures embedded with polyimide (fig.1.1), which were found to be very lossy, often preventing the lasing action for shorter, curved devices (section 4.4). On the other hand, wider 4μm wide rib lasers operated successfully. Note that the polyimide on the side of the guide was only some 0.1 to 0.2μm thick and was covered with a highly optically absorbing gold layer (fig.1.1).

The fraction of the light travelling outside the guide rapidly increases for higher order modes, discriminating against them, if the wall and outside media losses are excessive (table.1.2), particularly for curved guides. The optimally designed double heterostructure possesses a higher refractive index step and consequent increased light confinement over that of the quantum well material (section 2.1). This results in a faster decay, not only within the cladding layers, but towards the outside of the guide as well (e.g. a 2μm rib guide of .15μm GaAs sandwiched between the two 1.5μm $Al_{.6}Ga_{.4}As$, resulted in a field decaying down to 3% at the boundary with air; this was 7% in the case of the quantum well guide).

The finite difference program was succesfully used to present the local normal modes available within a structure incorporating two waveguiding regions (see section 1.4) and could be used to calculate the field distribution within the cross-section of a bent guide, by using a conformally transformed refractive index field distribution, which, generally, increases towards the outside of the guide (section 1.6.1).

1.4. DIRECTIONAL COUPLING OF TWO WAVEGUIDES.

The spread of the light away from the guide and its coupling to the outer region through too narrow or too small barrier cladding regions degrades the quality of the laser guide (fig.1.2). To prevent it, the thickness of the cladding layers must be sufficient to allow the evanescent optical field to decay almost down to zero within the cladding layer. The coupling, on the other hand can be utilised in an integrated optical circuit, where the light created in the active lasing region is coupled to the closely positioned passive waveguide (fig.1.9).

Two waveguiding regions of widths $a_1 = a_2 = a$, with a separation c form a directional coupler with a characteristic interaction length L_c [Marcatilli-5, Marcuse-11]. The structure supports both a symmetric and an asymmetric normal mode. Over the length L_c, the power (square of the amplitude) is transferred from one guide to another due to slightly different phase velocities of the two normal modes , and varies as $\cos^2(k^*z)$ in the first guide and as $\sin^2(k^*z)$ in the second guide, for the

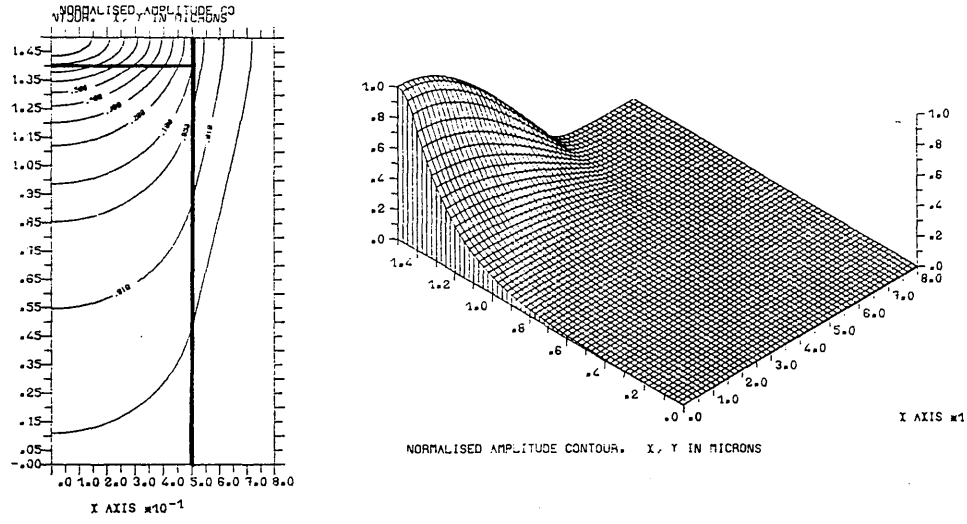

Fig.1.8. Two– and three–dimensional plot of the zero order local normal mode, within a waveguide of 7.6nm wide GaAs well sandwiched between 0.105μm thick layers of $Al_{.25}Ga_{.75}As$ (n_{w+c}= 3.443854), sandwiched in turn between cladding layers of $Al_{.6}Ga_{.4}As$ (n_c= 3.261709) and surrounded on both sides of the 1μm wide guide with polyimide (n_s= 1.615).

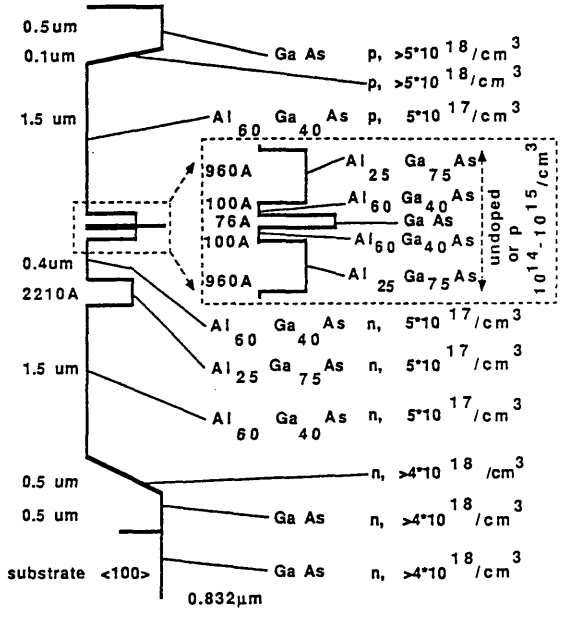

Fig.1.9. Laser structure incorporating a passive guide coupled to the lasing layer. and an improved carrier confinement region.

symmetrical structure [Marcatilli– 5, Marcuse– 11, Walker– 12]:

$k = \frac{\beta_s - \beta_a}{2}$ is the coupling coefficient, (1.29)

$$L_c = \frac{\pi}{2*k} = \frac{\pi}{\beta_s - \beta_a} = \frac{\lambda_o}{2*(n_{effs} - n_{effa})} \quad (1.30)$$

where: β_s, β_a are propagation constants of symmetric and assymetric modes.

For low– loss guides, 25% of the coupling length is sufficient for proper coupling action [Walker– 13].

The interaction between two closely positioned guides (fig.1.9) may be observed by analysing the local normal mode distribution within the structures, e.g. using a finite difference method. When introducing a field into one of the guides only, and stopping the program randomly, the field evolution from the unstable mode to that of the stable symmetric local normal mode was observed (fig.1.10).

As an example, consider the experimental laser devices with coupled guides (fig.1.9), presented in section 2.4.4. Two guides of 0.2196μm widths and refractive indexes 3.443854 and 3.437237 ($Al_{.25}Ga_{.75}As$ + GaAs well, and $Al_{.25}Ga_{.75}As$), separated by the 0.4 μm thick $Al_{.6}Ga_{.4}As$ of the refractive index 3.261709, produce the effective refractive index of the achieved symmetric mode equal to 3.3394928, while that of the other stable asymmetric mode is equal to 3.3255339. The coupling lenth is then:
$L_c = 0.84 / (2*(3.3394928-3.3255339)) = 30\mu m$.

The values of the effective refractive index of various slightly asymmetric structures and their coupling lengths, obtained by the finite difference method were similar to those calculated using a program [Bhumbra– 14] for a symmetrical slab directional coupler which uses a coupling coefficient equation [Kuznetsov– 15]. The coupling length of two closely positioned guides, presented above (fig.1.9), strongly decreases with the increased spacing between them, as seen in Table.1.3.

Longer devices with too close guides transfer the power away from the active region [Furuya– 16]. The ring optical path within the longer devices may be of the order of 1600μm. The cladding layers should therefore be thicker than 1.5μm to prevent light loss and consequently increased threshold current (fig.1.11). This was confirmed with experimental laser devices.

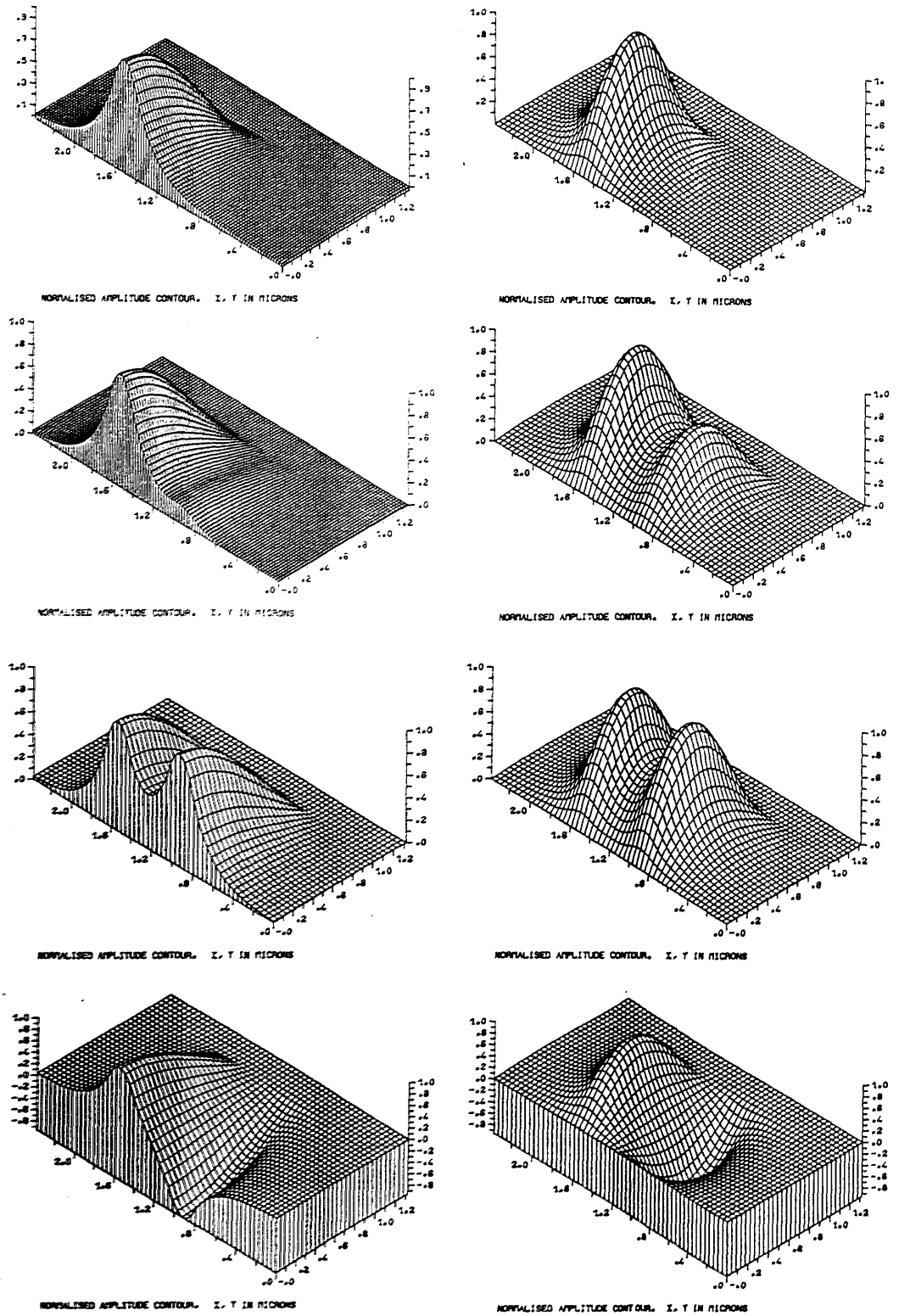

Fig.1.10. Evolution of the zero and first order local normal modes from the unstable mode to the stable symmetric mode within the structure of the directionally coupled laser to the passive guide, similar to that, presented in fig.1.9. Plots were produced using the excited single guide by a finite difference method. The plots represent the interaction between the two 0.2176μm wide guides of n_{ga}= 3.443854 and n_{gp}= 3.437237 ($Al_{.25}Ga_{.75}As$ + 7.6nm thick GaAs well, and $Al_{.25}Ga_{.75}As$) separated by the 0.4μm thick barrier layer of n_s= 3.261709 ($Al_{.6}Ga_{.4}As$). Also, stable asymmetric modes within the structure.

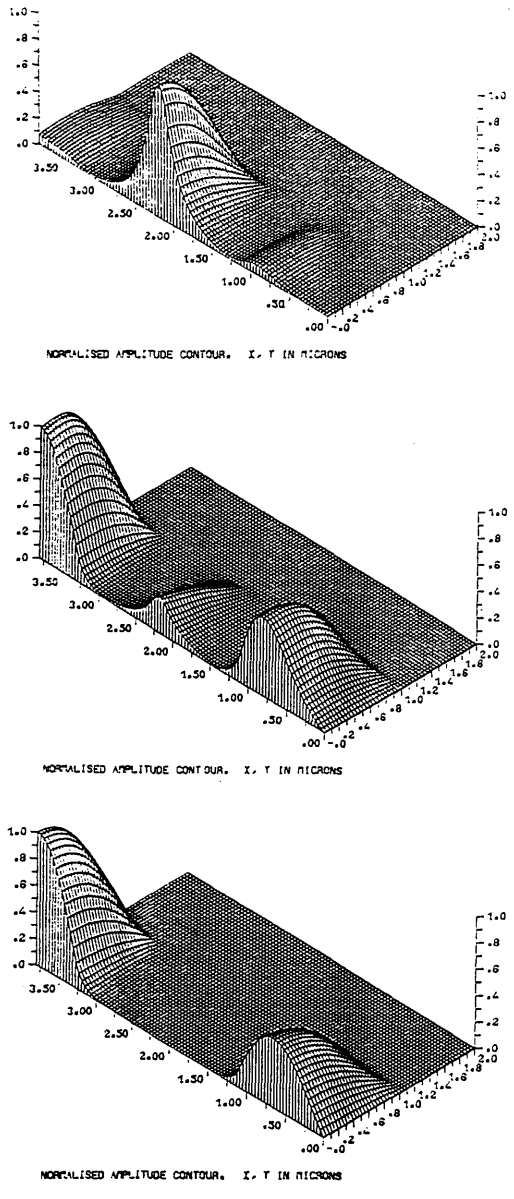

Fig.1.11. Stable local normal mode evolution within the laser structure with excited middle guide of $Al_{.25}Ga_{.75}As$ + 7.6nm GaAs well sandwiched between the thin cladding layers of 1 μm wide $Al_{.6}Ga_{.4}As$, with subsequent contact layers made of GaAs.

Table.1.3. Coupling length of the weakly coupled structure presented in fig.1.9, TE polarisation.

spacing (μm)	.1	.3	.5	.7	.9	1.1	1.3	1.5	1.7
coupling length (μm)	6.6	18.6	52.5	147.8	416	1171	3297	9283	26133
guide field level (%)	49	19	7	3	.95	.45	.1		

The coupling depends on both the thicknesses of the guides and the spacing between them, particularly in the case of the high index step materials used. Weak confinement (fig.1.9) (table.1.3) provides coupling within the practical length of the device. Table.1.4 presents the rapid increase of the coupling length with increased width of both the guides and the spacing, for the strongly confined structures (fig.1.12). The guides and the spacing are of refractive indexes of 3.444195 and 1.0 respectively. Again, the decreased width of the guide corresponds to the rapidly increased field decay.

Table.1.4. Coupling length of the strongly coupled structure presented in fig.1.12. TE polarisation.

guide width (μm)	.2	.2	.3	.3	.3	.3	.3	.4	.5
spacing (μm)	.1	.2	.1	.2	.3	.5	1.	.1	.1
coupling length (μm)	11.7	112	32	340	3700	$436*10^3$	$64*10^6$	67	121
guide field level (%)			4.5	.8	.08				

The high refractive index step results in the possibility of directional coupling between the guides only for devices with very small transverse dimensions. The experimental guide ribs down to 0.4μm width spaced by 0.4μm of air or polyimide (fig.1.12) were ineffective (section 4.4). The guides were very lossy due to the spread of the optical signal into the Au overcoat.

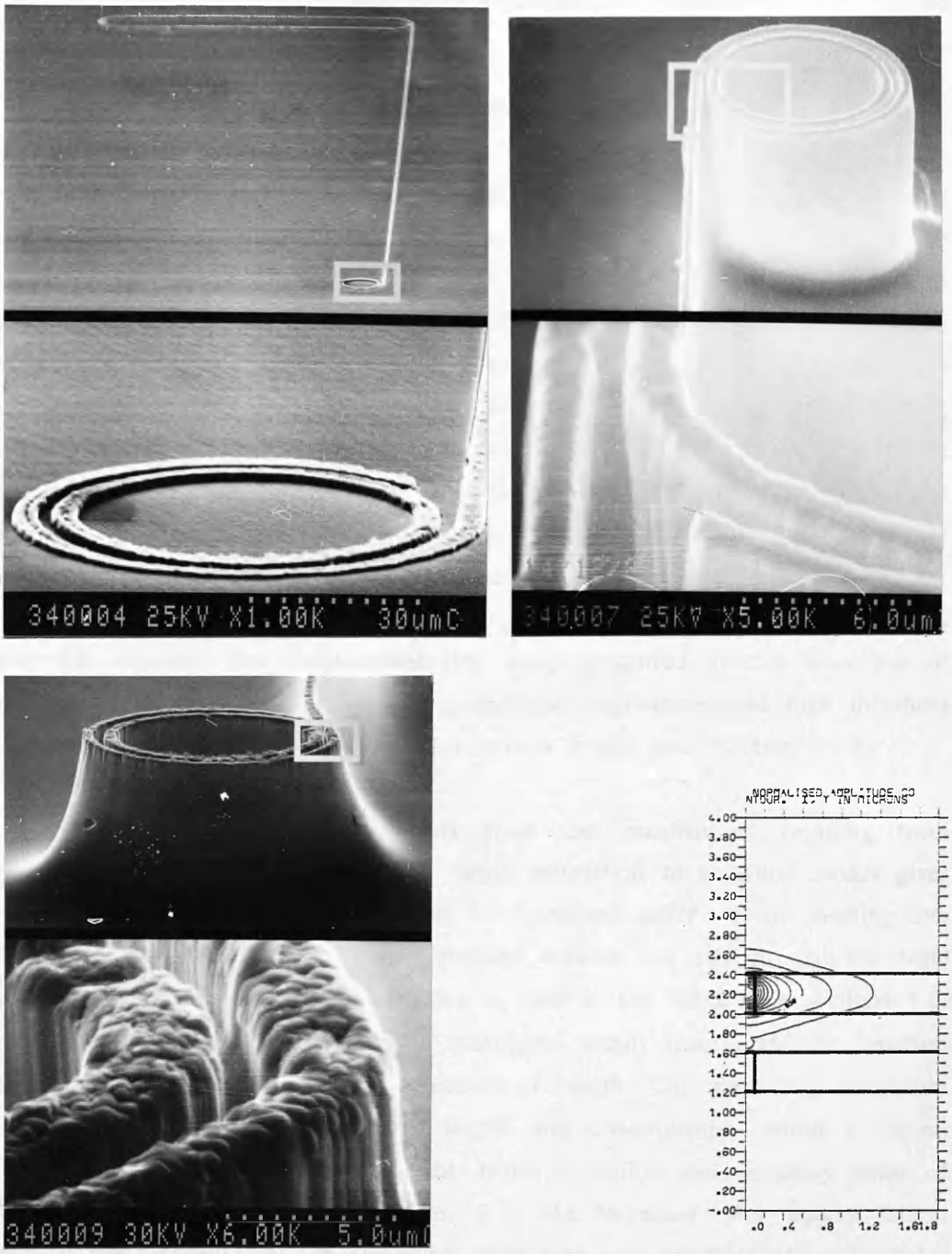

Fig.1.12. Steps of processing the ring laser configuration of polyimide– embedded directional coupler between two 0.4μm wide guides separated with the 0.4μm wide polyimide spacer, made in material presented in fig.1.2. The device did not operate. Also shown, the computation of the local normal mode of the structure with the excited single guide.

1.5. WAVEGUIDE TOTAL LOSS.

Low-threshold-current ring laser devices (fig.1.13) require strong waveguiding properties with small losses to minimise the necessary gain. The performance of the guides is determined by the quality, configuration and doping of the materials (section 2) as well as by their lateral confinement and shape. Straight stripe structures are easily described, while the theory of curved guides, closed loop resonators and Y-junctions is still the subject of much attention. The existing theories allow estimates to be made of waveguide parameters such as the minimum radius of the chosen guide structure, that would not introduce excessive losses. The theoretical work is presented in sections 1.6, 1.7, 1.8 and 1.9. Some practical research into the subject has been undertaken by [Takeuchi-17, Matsumoto-18, Kawaguchi-19, Shuh-Huei-20, Austin-21, Scifer-22, Sansonetti-23 and Jezierski-24, 25, 26]. The experimental ring lasers presented in this work are of various configurations and the smallest rings incurred large losses and high threshold current, mainly due to the short cavities and narrow guides used (section 4.3.4).

Light propagating in a waveguide suffers from loss mechanisms resulting from absorption α_a and scattering α_s (fig.1.14). Mode conversion to radiation modes gives rise to a loss α_{mc}. Curved waveguides (or Y-junctions) suffer from coupling loss α_c due to conversion of the mode field profiles between the straight and the bend region (or Y-junction), and radiation losses α_r due to the bends [see sections 1.6, 1.7 and relevant references]. Measurement techniques usually incorporate the insertion loss of the light into the guide α_i, independent of length. The scattering, absorption and radiation are proportional to guide length and consequently, within a curved guide or closed ring, to the radius of the bend. Radiation and coupling losses of both bends and Y-junctions (sections.1.6, 1.7) are increased with poorer lateral confinement and smaller radius of curvature. Note that poor lateral confinement (also due to the narrow guides) means that a larger part of the wave travels outside the guide, where it may be subject to scattering loss on the guide surface and absorption loss within the outside medium (section 1.3).

The total loss of the guide α_g can therefore be expressed as (see sections 1.6, 1.7):

$$\alpha_g = \alpha_i + \alpha_{mc} + \alpha_a + \alpha_s + \alpha_c + \alpha_r$$
$$= \alpha_i + C*\pi*R_c*(\alpha_{mcc}+\alpha_{ac}+\alpha_{sc}+\alpha_{rad}(R_c)) + 2*C_\alpha*c^2$$
$$= \alpha_i + C*\pi*R_c*[\alpha_{mcc}+\alpha_{ac}+\alpha_{sc}+A_1*R^{-3/2}*\exp(-B*R_c)] +$$
$$+ 2*C_\alpha*[\pi*n_1^2 * \frac{a^3}{\lambda^2*R_c}]^2 \text{ (section 1.6.1);} \qquad (1.31)$$

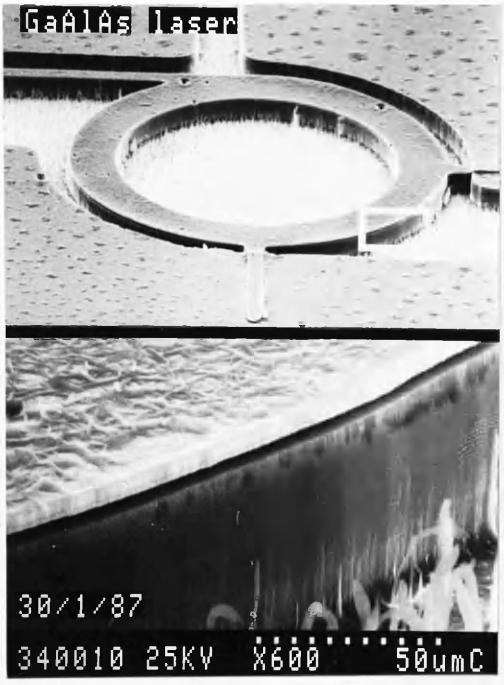

Fig.1.13. Practical ring laser with an output guide connected via a Y— junction.

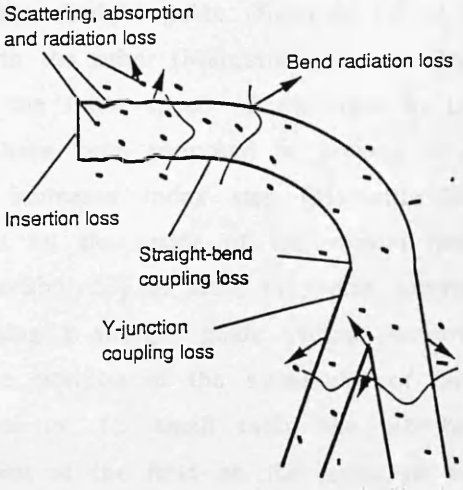

Fig.1.14. Losses within the optical waveguide.

(for a slab guide, the factor $A_1{}^*R^{-3/2}$ should be replaced with a factor A_3),
where: C_α is a coefficient, describing the lost power,
$C = 1$ for 180^o bend,

$$B = 2*\zeta*\frac{n_{eo}-n_s}{n_s} \qquad (1.32)$$

The analysis of practical curved devices, optimising the radius of the bend to assure reasonable loss, was presented by [Austin– 21]. As explained previously, the coupling and radiation losses could be minimised, and in some cases eliminated [see sections 1.6, 1.7 and relevant references]. Wider and stronger guides with not too small bend radii, reduced the absorption and scattering losses and produced low threshold current ring laser devices (section 4).

1.6. RING LASER WAVEGUIDE BENDING LOSS.

A ring laser device incorporates a curved closed loop guide (fig.1.13), which uses total reflection of the light from the external boundary of the bend and results in a shift of the field outwards (figs.1.14, 1.15 [Kassim– 27]). The shift of the field produces a mismatch of the field to that of the straight guide (figs.1.6, 1.7, 1.8) and consequent insertion loss from one section to the other [Marcatili– 28] (fig.1.14). Additionally, radiation loss is observed due to the finite speed of the light in the outer region [Neumann– 29]. Various solutions have been proposed to prevent those losses. These include: the strong guide with increased index step [Marcatili– 30]; using a guide with increased dielectric constant on the inside of the central bend region [Marcuse– 31, Neumann+ Richter– 32, Gerisho– 33] to shift the wave towards the inside of the bend, [Neumann– 34]; and using a straight guide shifted outwards with respect to the curved guide, to match the position of the maximums of both sections [Penning– 35]. In addition, wider guides or, for small radii, the pill– box structures, were proposed to reduce the constraint of the field on the inside of the guide [Neumann– 34], while guiding the "whispering gallery" modes [Sheem+ Whinnery– 36]. Above a certain value of guide width there is little reduction of the loss [Marcatili– 28] and the pill box structures, having a larger total area may increase the necessary threshold current of the ring lasers. Nevertheless, the experimental structure of diamater 12μm operated succesfully with a reasonable threshold current (section 4.3.3).

1.6.1. Radiation loss.

A model of the curved guide is represented by the straight guide with the same propagation constant n_{es}, but with the conformally transformed refractive index profile, as shown in fig.1.16 [Heiblum– 37].

The relation between the losses existing within the curved structure, namely coupling α_c and radiation α_r losses, and the radius of the curvature are not easily derived [Kendall– 38], particularly for a small radius and large dielectric constant step (fig.1.13), where the general variation can only be assumed.

In approximation, a wave function of the stripe guide, is separable in two directions, and outside the guide edge, the field amplitude decays exponentially. This may be easily described in cylindrical coordinates ρ, Φ. For a constant angular phase velocity of the wave travelling within the curved guide and at a certain distance D from the outside guide boundary R_c, the linear phase velocity v_p would need to exceed the velocity of light to keep up with the rest of the field. This part of the field is lost by radiation [Neumann– 29]. Assuming:

$$v_p = v_{pc} * \frac{\rho}{R_c} \qquad (1.33)$$

$$n_e = n_{ec} * \frac{R_c}{\rho} \qquad (1.34)$$

$$\text{then: } D = \rho_D - R_c = R_c * \left(\frac{n_{ec}}{n_s} - 1\right) \qquad (1.35)$$

where: n_{ec}, v_{ec} are the effective index and linear phase velocity at R_c,
ρ_D is a radius larger than R_c by D, above which the loss occurs,
n_s is a substrate index.

To achieve a small bending loss, the radius of curvature R_c, and the step of dielectric constants between the guide and the outside layer, must be large. The complex equations describing the bend loss coefficients may be then simplified [Kendall– 38] for:

$$R_c > \frac{k_{outside} * W}{\beta - k_{outside}} \text{ and } \delta_{outside} \text{ large,} \qquad (1.36)$$

$$\text{where: } \delta_{outside} = \sqrt{(\beta^2 - k_{outside}^2)} * R_c \qquad (1.37)$$

$$k_{outside} = \omega * \sqrt{(\varepsilon_{outside} * \mu)} \qquad (1.38)$$

$\beta = \beta_{eff} * \frac{2*\pi}{\lambda_o}$ is a propagation constant of
a straight guide. (1.39)

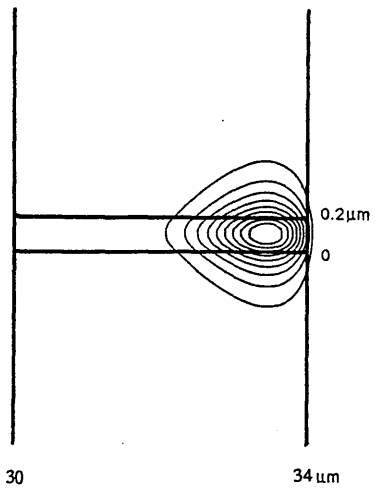

Fig.1.15. An example of a wave field distribution within the curved guide with strong confinement [After Kassim– 27].

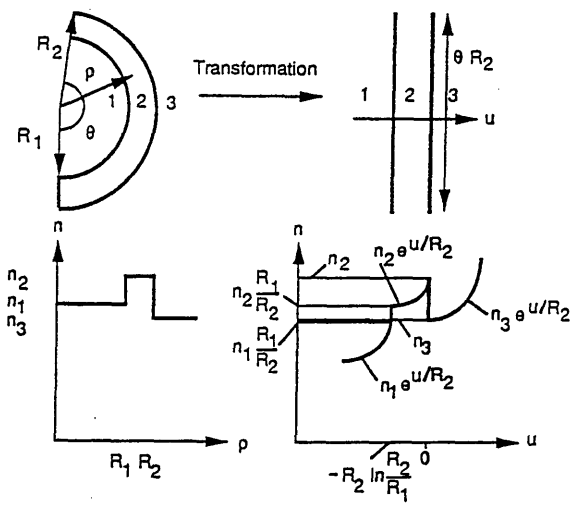

Fig.1.16. Refractive index conformal transformation of a bend guide [After Heilblum– 37].

Curvature loss formulas take different forms for the attenuation coefficients of a curved slab α_{sl}, a curved stripe guide with a low dielectric step to the outside layer α_{ls} (compared to the refractive index of the guide) and a curved stripe guide with a large dielectric step α_{bs} (comparable to the refractive index of the guide):

$$\alpha_{bs} = A_1 * R_c^{-3/2} * \exp(-B*R_c) \quad (1.40)$$

$$\alpha_{ls} = A_2 * R_c^{-1/2} * \exp(-B*R_c) \quad (1.41)$$

$$\alpha_{sl} = A_3 * \exp(-B*R_c) \quad (1.42)$$

α_{sl} is significant for: $R_{sl} < \frac{1}{B} * \ln A_3$

where: A_1, A_2, A_3, B are factors independent of radius, and dependent on lateral confinement between the guide and the outside region (decaying factors) and are large,

W is the halfwidth of the guide,

Note that: $A_1 * R_c^{-3/2}$, $A_2 * R_c^{-1/2}$ and A_3 are slowly varying quantities, while: $\exp(-B*R_c)$ varies rapidly.

The radiation loss of the stripe guide allows therefore for smaller radius than that offered by a slab guide, before the radiation loss α becomes intolerable.

The exponential coefficient B depends on [Walker–12]:

$$B = 2*\zeta*\frac{n_{eo}-n_s}{n_s} \quad (1.43)$$

$$A_3 = \frac{A_{33}}{\zeta} \quad (1.44)$$

where A_{33} is a constant,

n_{eo}, n_s are effective indexes of the guide mode and the surrounding media,

ζ is a field decay factor (e.g. $2.5\mu m^{-1}$),

$$\text{Parameter } A_3 = 2*k*\zeta*\frac{n_{eo}-n_s}{\pi*\alpha_1*n_s} \quad (1.45)$$

without the insertion loss, where: α_1 is small, of the order of $2*10^{-4}$dB/μm. The value of $\ln(A_3)$ decreases slowly with increased losses.

Loss of the slab guide (1.42) can be described as:

$$\alpha_{slab} = 2*k*\zeta*\frac{n_{eo}-n_s}{\pi*\alpha_1*n_s} * \exp[-2*\zeta*R_c*\frac{n_{eo}-n_s}{n_s}] \quad (1.46)$$

$$h^{\alpha}slab = 2*k*\zeta*\frac{n_{eo}-n_s}{\pi*\alpha_1*n_s} * \exp[-2*\zeta*R_c*\frac{n_{eo}-n_s}{n_s}] \text{elow the critical:}$$

$$R_{slab} < 1/[2*\zeta*\frac{n_{eo}-n_s}{n_s}] * \ln A_3 \quad (1.47)$$

With increased refractive index step, a value of α_{slab} achieves a peak at a certain value of the index step that becomes smaller as the radius increases. Also, the critical radius is mainly dependent on 1/B and increases with decreased refractive index step (table.1.5).

[Walker's–12] calculations of parameters B and A_3 are based on the total loss within the slab bent guide and assume an arbitrary value of the coefficient k of his practical guide ($\Delta n = 0.09$, $n_{eo} - n_s = 0.012$, k= 11200dB). The total radiation loss α_r is dependent on both radiation loss coefficient (e.g. α_{bs}) and R_c and so the coefficient k should be R_c dependent. The complete expression for total waveguide loss of a stripe bent guide is much more complex than for the slab guide and is not easy to calculate. Function analysis indicates that lnX should take a smaller value of between $\ln A_3 \simeq$ 9 to 12, for low loss guide.

Table.1.5. Calculated minimum bend radius providing small losses, using Walker's solutions.

n_s	3.2	1.5	3.2	1.5	3.2	3.2	1
$n_{eff}-n_s$	0.0002	0.0002	0.01	0.01	0.1	0.35	2.4
1/B	3050	1500	64	30	6.4	1.8	0.08
lnA	9	9	13	13	15	16	18
$R_{slabmin}$ (μm)	27450	13500	832	390	96	28	1.44

Walker's calculations may be compared with a simple estimate of the minimum radius of a ring waveguide R_{cmin} to provide a low bending loss coefficient $\alpha_r/(C*R_c)$ (fig.1.17) (table 1.6). The estimate assumes a 50% loss of the transmitted power on each reflection on the outside wall, neglects the exponential field spread into the outside medium, assumes uniform divergence of light and that a ring transmits the light along the shortest path:

$$R_{cmin} = s * \frac{n_2}{2*dn} \qquad (1.48)$$

where: $dn = n_2 - n_1$ is a refractive index step,

n_2, n_1 are refractive index of core and outside layer,

s is a width of a tranverse field width, dependent on the optical confinement and the radius.

Table.1.6. Calculated minimum bend radius providing small losses, using simple estimate, with 5μm field.

n_2	3.4	1.5.	3.4	1.5	3.4	3.4	3.4
Δn	0.0002	0.0002	0.01	0.01	0.1	0.35	2.4
R_{opt} (μm)	85000	37500	1700	750	170	48	7
R_{min} (μm)	42500	18750	850	375	85	24	3.5

From the above, the rib ring lasers considered (figs.1.1, 1.13), with diameters down to 12μm, should produce acceptable radiation loss, due to the high index step provided. Still, the practical small diameter laser devices operated at greatly increased threshold current density, probably due to the short cavities used (section 2.2.3).

The radiation loss α_r is proportional to radius R_c and the bend loss coefficient:

$$\alpha_r = C * \alpha_{bs,ls,s} * R_c \qquad (1.49)$$

where: the loss coefficient α refers to the particular waveguide (slab, with a low index step and with a high index step), and C is a constant determined by length,

1.6.2. Straight– to– curve section coupling loss.

The waveguide structure incorporating the curve to straight sections [e.g. the racetrack of Walker–12] results in losses, additional to those described above, due to mode transitions at the straight– to– curve and curve– to straight sections, increasing the value of minimal radius necessary for low lossy guiding. Wider guides may support many modes, and transition sections result in loss due to mode inter– conversion. Narrower guides, supporting a single mode, are lossy at the transition sections due to conversion to a mode that is no longer supported by the further section.

Mode conversion loss was analysed by [Marcatili–28] and [Neumann–34] using coupled– mode theory, and could be reduced with increased radius R_c, improved light confinement and reduced decay factor.

The system analysed in our work uses a ring resonator with a Y– junction branching output waveguide. This configuration does not introduce the straight to curve section mode conversion, and therefore this problem is not to be considered further. Instead, a mode conversion loss within a Y– junction is discussed (section 1.7).

1.7. Y- JUNCTIONS WITHIN THE RING LASERS.

Y- junctions were used in our work as means of splitting and redirecting part of the optical beam oscillating within a ring laser to the output guide (figs.1.1, 1.12), or for combining two beams together [Cullen- 39].

The analysis of a Y- junction is complex and is not well developed, particularly for multimode and high refractive index step guides, the non- symmetric Y- junction made of non- identical guides and guides which are positioned at different angles to the junction [Thurston- 40]. It involves the calculations of the local normal modes available within the subsequent cross- sections and their related levels of excitation, followed by evaluation of loss due to their convergence and their different effective propagation constants [Marcuse- 41, Burns- 42]. The analysis usually neglects the junction loss due to transition length and back- reflection.

There are three distinctive Y- junction regions: a junction region of two converging guides, and a tapered region down to the third region of a single guide [Anderson- 43] (fig.1.18). The junction region may be represented by a series of two parallel guides with decreasing separation [Burns- 42], and the tapered section by a series of waveguides with different widths [Marcuse- 41].

There are two contra- rotating waves oscillating within the ring laser with the Y- junction (fig.1.19) (section 1.8). These waves approach the Y- junction from different directions: from the side of the fork and the side of the single guide respectively and may therefore suffer different losses. The round trip transition loss of each of the waves determines the required gain and threshold current for supporting lasing oscillations. The wave suffering the smaller loss will determine the lasing action direction. At higher currents, the device may additionally lase in the second direction, but providing small optical power. At further increased gain the dominating oscillations may damage the structure. To couple the light out of the resonator to the output guide, the dominating wave should approach the Y- junction from the side of the single guide (fig.1.19).

Let us compare wave propagation within the junction illuminated from each of the directions.

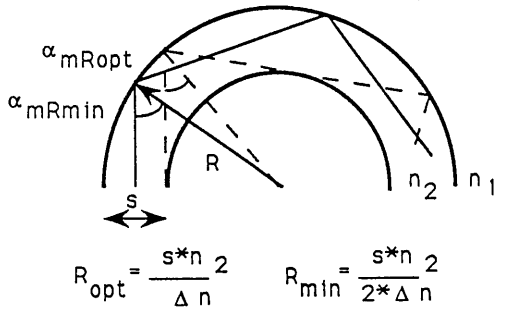

Fig.1.17. Diagram used for a simple estima e of the minimum radius of a ring waveguide R_{cmin}, providing a low bending loss coefficient.

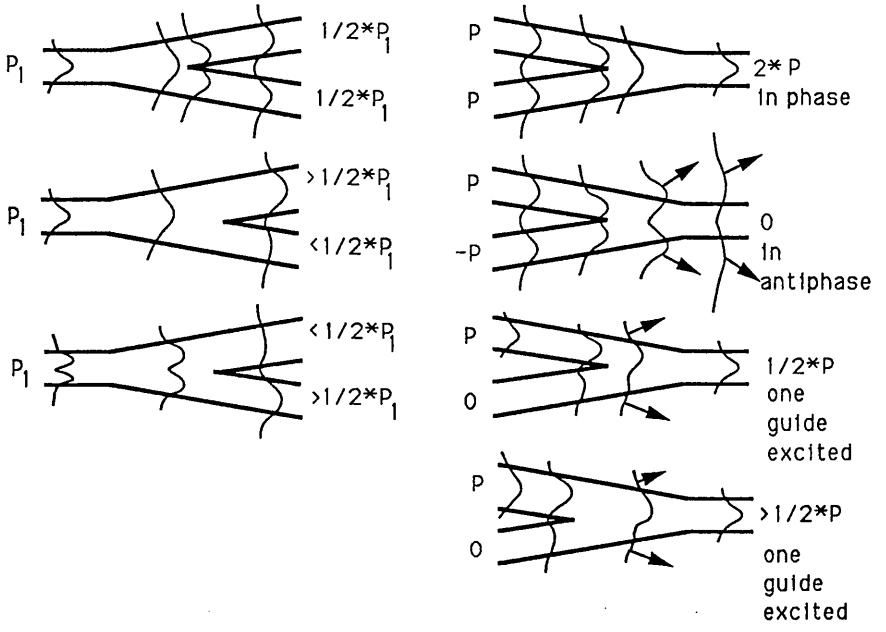

Fig.1.18. Y– junction illuminated from the side of a fork or a single guide. [After Cullen– 39, Thurston– 40].

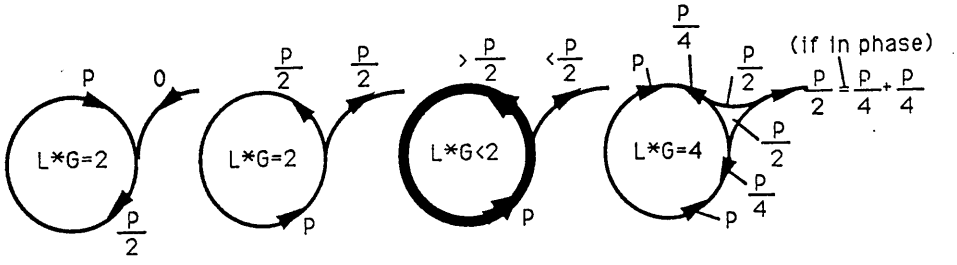

Fig.1.19. Contrarotating waves oscillating within the ring laser.

1.7.1. Y– junction illuminated from the side of the fork.

A Y– junction illuminated from the side of the fork can be discussed in two stages: a junction region of two converging guides and a tapered region (fig.1.18). Within the junction region, close proximity of the guides and a larger width of the taper than that of the guides may result in mode conversion from those available within the input guides into additional higher order modes supported by the wider junction [Cullen– 39, Thurston– 40]. This is determined by the configuration and parameters of the specific structure. The overall power transmission through the junction decreases at increased angle between the branches due to a phase mismatch of the corresponding fields. However, the mismatch is less important even for larger branch angles, in a high index step system [Anderson– 43].

On the way through the taper, the higher order modes, which cannot be supported by the narrower output guide, are radiated into the substrate, while the lower order modes are transmitted to the output guide reducing the ratio of output to input power (fig.1.18) [Cullen– 39].

Even an ideal symmetric Y– junction made of single– mode guides may result in different levels of power convergence, transmittance and loss, due to different levels of excitation of the odd– and even– modes within the wider part of the taper. It should be noted that the available modes within the guide depend on both the dimensions and the index step of the guides. The guide section whose width is twice the width of a single– mode guide may be therefore either single or multimode.

The simplest case, where an ideal symmetric, small branch– angle Y– junction was made of single mode guides and the even– and odd– modes were excited equally within the taper, was analysed by [Cullen – 39]. The structure assumed lack of reflection, taper and phase– shift losses. Although not very compatible with our complex case of multimode, non– symmetric, large branch– angle Y– junction, it allows us to understand the approach to the problem. The output power within the basic Y– junction varies as:

$$P_{out} = 0.5 * [P_{in1} + P_{in2} + 2*/(P_{in1}*P_{in2}*\cos\Phi_{in1,in2})] \qquad (1.50)$$

where: P – power, $P=\Psi^2$,

Ψ is a field amplitude,

Φ is a phase shift between the two input waves.

Note that with equal power and phase in input guide waves, the output power equals a sum of both input powers (fig.1.18):

$$\Psi_{in1}=\Psi_{in2}=\Psi_{in} \rightarrow \Psi_{out}=\frac{2}{\sqrt{2}}*\Psi_{in},\ P_{out}=2*P_{in} \text{ and } P_{radiation}=0. \quad (1.51)$$

With equal power and antiphase between the waves, the output power is zero (fig.1.18):

$$\Psi_{in1}=-\Psi_{in2} \rightarrow \Psi_{out}=0,\ P_{out}=0 \text{ and } P_{radiation}=2*P_{in}. \quad (1.52)$$

With illumination from one of the branches only, only half of the power is transmitted (fig.1.18):

$$\Psi_{in2}=0 \rightarrow \Psi_{out}=\Psi_{i1}*\frac{1}{\sqrt{2}},\ P_{out}=0.5*P_{in1} \text{ and } P_{radiation}=0.5*P_{in1} \quad (1.53)$$

Experiments proved the Y–junction to be the source of highest intensity scattered light within the device (fig.1.20). The high index step structure of the practical ring laser guide with a branching guide assures a low loss due to phase mismatch, even at higher and asymmetric branch angle [Anderson–43]. The waves in the converging guides of the Y–junction are not expected to be of similar power and in–phase. Higher order modes than those provided by the input guides are expected to be excited in the junction region, where the dimension of the taper is greater than those of the guides. This may be enhanced by the asymmetry of the guide dimensions with the ring guide wider then the other branching guide. On the way along the taper, modes of higher–order than those supported by the output guide would be lost. The approximate Y–junction loss value for a single mode ring guide would be 50%, but may differ for experimental multimode non–symmetric guides. As explained in section 1.7.2, the transmittance along the ring in a contra–rotating direction should be larger for a useful laser operation, and could be achieved by using a ring guide, which is wider than the branching guide.

1.7.2. Y–junction illuminated from the side of the single guide.

A Y–junction illuminated from the side of the single guide may be considered in two stages: a taper region and a junction region of two diverging guides (fig.1.18). The taper may introduce mode conversion from those modes available within the input guide, into additional higher order modes available within the wider part of the taper.

Overall taper transmission losses decrease with increased length of the taper and improved confinement due to an increased index step. Assuming that the output guide can support the taper modes, [Marcuse- 41] determined conditions for low loss taper transition.

The overall diverging guide losses exist even for a very small separate branch angle, due to coupling between the branches outside the junction region (e.g. 2% [Anderson- 43]). The overall power transmission loss of the junction region is increased at increased angle between the branches and consequent phase mismatch of the corresponding fields [Sasaki- 44, Kuznetsov- 45]. This is drastically reduced, even at larger branch angles, with an improved confinement due to a high index step [Anderson- 43] (Table.1.7).

Table.1.7. Overall power transmission through the Y-junction with an increased index step.

Index step	0.0004?	0.01	0.43
Branch half-angle (°)	1	8	15
Overal power transmission (%)	50	50	95

A small junction overall power loss is therefore expected at the index step of $\Delta n = 2.4$, used in our experiments.

An increased step may allow multimode operation, unless the guides are narrower. However, narrower guides increase scattering, absorption and radiation losses due to Y- junction or guide bends and should be avoided (section.1.5).

The distribution of power to the output waveguides depends on the symmetry of the output guides. The power of each optical mode may be divided equally between the output guides, if they are identical, with identical propagation constants (fig.1.18) [Kapon- 46, Thurston- 40].

The system incorporating output guides configured at a different angle to the input guide may result in a phase mismatch of the high angle branch and consequent asymmetric power transmission to each guide [Sasaki- 47, Frenette- 48]. In a higher index step system, this can be negligible, even for larger branch angles [Anderson- 43]. This may be further reduced with a long interaction region and

curved guides replacing the short, straight guides [Forbes- 49], and decreased refractive index near the branching regions [Hanaizumi- 50].

In a multimode junction described by [Thurston- 40], the power of the available optical modes is transferred to selected different guides, if they are of different widths and propagation constants. A junction of single mode guides transfers the lowest order mode of the common section into the widest guide with the highest propagation constant, while higher order modes are converted to modes supported by the weaker guides (fig.1.21) [Thurston- 40]. The situation is more complex for multimode guides, which will distort this mode splitting.

The Y- junction within the ring laser with a branching guide should favour the transfer of power to the ring guide over that to the branching guide, to maximise the ring oscillating power (fig.1.19). The practical high index step laser guides assure negligible loss due to asymmetry of the angles of the output guides and negligible phase shift loss, even at larger angles. The Y- junction with single mode guides can be treated as a power divider, if the junction is symmetric, or as a mode splitter, if assymetry is introduced. Multimode practical laser guides disturb the power distribution to the output guides, even though bending losses within the ring discriminate against the higher order modes. Using a ring guide wider than the branching guide should assure that a larger part of the power is transferred around the ring [Thurston- 40] (fig.1.18). Too wide a ring guide leads to the pill- box structure, which does not improve the guiding mode capability (section.1.6). The output guide should be sufficiently wide to reduce losses and avoid the possibility of coupling very high modes only (see above). Experimental ring lasers with guide widths of 6 to 10 μm and branching output guide widths of 4 to 6μm operated succesfully, while those narrower with guide widths of 1μm did not lase (section.4.3.4).

1.8. RING LASER RESONATOR WITH A Y- JUNCTION COUPLER.

The ring resonator structure supports a circulating wave in a closed waveguide loop with a phase shift (β*L) proportional to the propagation constant β and the ring path length L. The loss per loop results in a decay factor σ in the amplitude of the wave- front Ψ and depends on the resonator radiation, absorption and scattering losses, as well as coupling and bend losses due to conversion of the mode profiles at any straight- to- bend section and at the Y- junctions. The losses were described in sections 1.5, 1.6, 1.7. After many circuits, the steady- state amplitude at a chosen

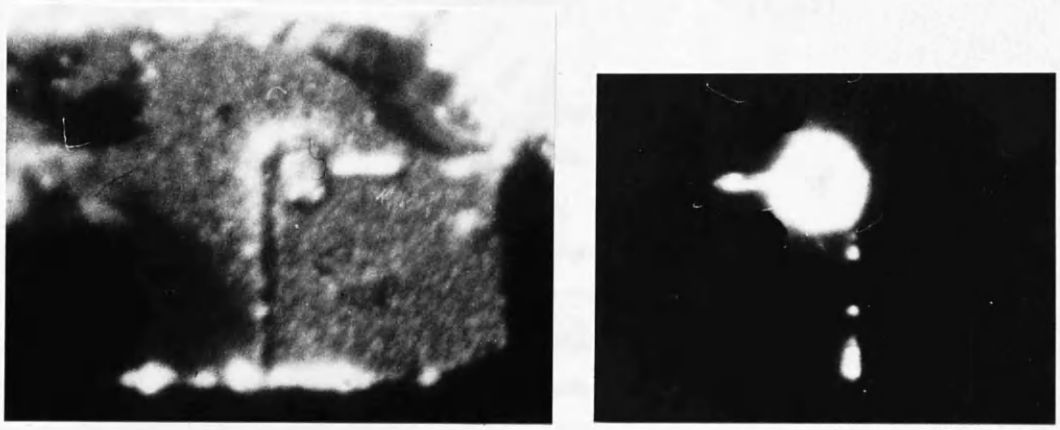

Fig.1.20. Luminescence of the scattered light emitted from the practical ring laser device.

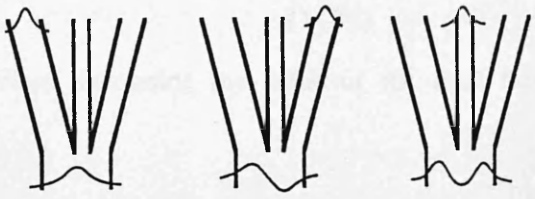

Fig.1.21. Multiguide Y– junction with the single mode guides of different widths [After Thurston– 40].

point is a sum of all the decaying waves [Walker− 13]:

$$\Psi_r = \Psi_o * \sum_{n=0}^{\infty} [\sigma^n * \exp(-j*n*\beta*L)] \qquad (1.54)$$

$$\Psi_r = \Psi_o * \sum_{n=0}^{\infty} [\sigma^n * (\cos(n*\beta*L) + j\sin(n*\beta*L))] \qquad (1.55)$$

where: Ψ_o is an initial field amplitude,
σ is a decay factor equal to 0 for infinitely lossy guides and equal 1 for lossless guides. The power lost on a round trip is therefore equal to $(1-\sigma)$.

This is maximised for $\beta*L = 2*m*\pi$ (even number of half− wavelengths) and minimised for $\beta*L = 2*(m-1/2)*\pi$ (odd number of the optical half− wavelengths), where m= 1, 2, 3..., giving the resonance and antiresonance conditions for different lengths of the closed optical path. The comb spacing $\Delta\lambda$ of the supported resonating wavelengths is presented in Appendix 1.

At resonance, the wave amplitude in the resonator, ignoring the laser gain, is:

$$\Psi_{rp} = \Psi_o * \sum_{n=0}^{\infty} \sigma^n = \Psi_o * \frac{1}{1-\sigma} \qquad (1.56)$$

while including the gain:

$$\Psi_{ra} = \Psi_o * \sum_{n=0}^{\infty} \sigma^n * G^n = \Psi_o * \frac{1}{1-\sigma*G} \qquad (1.57)$$

where: G is the gain due to injected carriers, increasing the value of the final field amplitude.

A practical ring laser resonator should have a means of power extraction to the output guide. This may take place via a Y− junction (fig.1.19). The decay factor σ per loop may be then presented as:

$$\sigma = (1-\sqrt{a})*(1-\sqrt{L}) \qquad (1.58)$$

where: a is a loss factor describing power lost to the ring oscillations while traversing the output junction, $0 \leqslant a \leqslant 1$,
L is a loss factor describing power lost due to guide attenuation, curvature, etc., and $0 \leqslant L \leqslant 1$.

At resonance, the steady state amplitude of the field at a chosen waveguide point is therefore:

$$\Psi_{ra} = \Psi_o * \sum_{n=0}^{\infty} (1-\sqrt{a})^n * (1-\sqrt{L})^n * \sqrt{G}^n = \Psi_o * \frac{1}{1-(1-\sqrt{a})*(1-\sqrt{L})*\sqrt{G}} \qquad (1.59)$$

The transmittance to the output guide is then:

$$\Psi_{outra} = \Psi_o * \frac{\sqrt{a}}{1-(1-\sqrt{a})*(1-\sqrt{L})*\sqrt{G}} \qquad (1.60)$$

1.9. CONTRA− ROTATING OSCILLATIONS WITHIN THE RING LASER.

Within the ring laser resonator there are two independent waves travelling in opposite directions [Wang− 51] (fig.1.19). The one that is subject to a smaller loss within the ring becomes dominant, with a larger amplitude. The dominating wave results in lasing action at a lower threshold current, overtaking the lasing action of the opposite wave.

The contra− rotating waves may have identical propagation constants, if the paths are symmetrical and then may interfere with each other at resonance, giving the standing wave pattern.

The symmetrical configuration may be analysed within the system of a resonating ring laser with light directionally coupled out of the ring to an adjacent passive guide which is coupled to the output guide (figs.1.9, 1.12). This configuration was suggested as an alternative to Y− junction coupling (see section 1.4), but was not investigated experimentally.

The incorporation of the Y− junction coupler into the ring, introduces asymmetry into the system, like mode coupling, different loss (see section 1.7), and possible different propagation constants of each wave. For constructive coupling of the light out of the ring, the circulating wave subjected to smaller loss and therefore dominant in lasing action should be the one which approaches the junction from the side of the single guide. This was discussed in section 1.7.

Two Y− junctions may be used to couple the light out of the two oscillating directions and combine them to the output guide (fig.1.19). Mismatch of the resonances in both directions may have been observed experimentally producing complex resonating spectra (section 4.3.3). Also the power collected from the two oscillating directions was smaller than that of a simple resonator with a single Y− junction directing part of the power to the output guide. This confirmed that the Y− junction is not only asymmetric, but also introduces loss in both transmittance directions (see section 1.7.).

1.10. SUMMARY.

The performance of the ring laser device is determined by the properties of the original laser material. The broad area two-dimensional structure was represented and investigated as a slab waveguide. Subsequently, the waveguiding properties of straight and bent stripe guides were investigated using a finite difference method. Two methods of coupling the light out of the stripe guide were studied: via a Y-junction and a directional coupler. This was followed with the analysis of the ring laser resonator with the incorporated Y-junction coupler.

Within a waveguide of any configuration there are losses due to absorption, scattering, mode conversion and mismatch, bend radiation and coupling. Low loss within the waveguide structures resulted in lower threshold current density and improved lasing properties of the final device. Strong confinment of the light to the guide and a small proportion of the decaying field travelling outside the guide may considerably decrease most of the losses.

A typical GaAs lasing guide of thickness 0.15 to 0.2μm requires cladding layers of a lower index material (e.g. $Al_{.6}Ga_{.4}As$) and sufficiently thick (e.g. $>$ 1.5μm) to prevent loss to outer layers. Stripe guides surrounded with a low index material, e.g. polyimide, typically should be wider than 4μm to avoid loss of the light travelling outside the guide due to scattering on the surface, absorption and bend radiation. Intentional directional coupling from one to another guide is possible, and for 0.2μm GaAs guides a spacing of 0.4μm of $Al_{.6}Ga_{.4}As$ results in a coupling length of 30μm. Bend radiation loss increases rapidly with a decrease in light confinement. The minimum radius providing acceptable loss, is of the order of 27 000μm for an index step of $2*10^{-4}$, 800μm for an index step of 10^{-2} and 28μm for an index step of 0.35. The Y-junction coupler is an asymmetric device lossy in both directions of transmission. It behaves as a power divider for symmetric structures or as a mode splitter for assymetric guides. Large angle branches may result in mode tilt loss but this can be neglected for large index step structures. Within the ring laser resonator there are two contra-rotating waves; the one subject to the smaller loss dominates the lasing action. A Y-junction incorporated into the ring resonator should direct part of the dominant wave to the output guide. The oscillating power may be increased for ring branches wider than the output guide. A variety of ring laser resonating devices were manufactured and their performance confirmed the theoretical predictions (section 4).

1.11. REFERENCES.

[1] Tien P.K.: Integrated optics and new wave phenomena in optical waveguides, Reviews of modern physics, Vol.49(2), pp.361–420 (1977).

[2] MacBean M.D.A.: Multiple quantum well structures as optical waveguides, PhD thesis, Glasgow University (1986).

[3] Kogelnik H.: Theory of dielectric waveguides, Topics in Applied optics, Vol.7: Integrated optics, ed. Tamir T., Springer–Verlag, Berlin, Heidelberg, NY (1975).

[4] Laybourn P.J.R., Lamb J.: Integrated optics: a tutorial review, The Radio and Electr.Eng., Vol.51 (7/8), pp.397–413 (1981).

[5] Marcatilli E.A.J.: Dielectric rectangular waveguide and directional coupler for integrated optics, Bell Syst.Techn.J., 48, pp.2071–2103 (1969).

[6] Wilkinson C.D.W: Theory of slab waveguides, tutorial, Glasgow University (1986).

[7] Knox R.M., Toulios P.P.: Proceedings of MRI Symposium on submilimiter Waves, ed. J.Fox, Polytechnic Press, Brooklyn, (1970).

[8] Koshiba M., Suzuki M.: Equivalent network analysis of dielectric thin–film waveguides for optical integrated circuits and its applications, Radio Sci., 17, pp.99–107 (1982).

[9] Benson T.M.: Integrated optical components produced in GaAs and InP epitaxial layers using the photo–elastic effect, PhD. thesis, Sheffield University (1982).

[10] Lee K.T.: M.Sc. thesis, Glasgow University (1987).

[11] Marćuse D.: The coupling of degenerate modes in two parallel dielectric waveguides, The Bell Sys.Techn.J., Vol.50 (6), pp.1791–1816 (1971).

[12] Walker R.G., Wilkinson C.D.W.: Integrated optical waveguiding structures made by silver ion–exchange in glass 2: Directional coupler and bends, Appl.Optics, Vol.22 (12), pp.1929–1936 (1983).

[13] Walker R.G., Wilkinson C.D.W.: Integrated optical ring resonators made by silver ion–exchange in glass, Appl.Optics, Vol.22, pp.1029–1035 (1983).

[14] Bhumbra B.: private communucation, Glasgow University (1987).

[15] Kuznetsov M.: Expressions for the coupling of a rectangular–waveguide directional coupler, Optics lett., Vol.8 (9) pp.499–501 (1983).

[16] Furuya K., Miller B.I., Coldren L.A., Howard R.E.: A novel deposit/spin waveguide interconnection (DSWI) for semiconductor integrated optics, IEEE JQE–18, 10, pp.1783–1789 (1982).

[17] Takeuchi H., Oe K., Imamura Y.: A very low–loss GaAs/AlGaAs miniature bending waveguide with curvature radii less than 1mm, Second Optoelectr.Conf., (OEC'88), Techn.Digest, Tokyo, 10 (1988).

[18] Matsumoto N., Kumabi K.: AlGaAs–GaAs semiconductor ring laser,

Japan.J.Appl.Phys., Vol.16 (8), pp.1395–1398 (1977).

[19] Kawaguchi H., Kawakami T.: GaAs–AlGaAs half–ring laser fabricated by deep Zn diffusion, Japan.J.Appl.Phys., Vol.16 (12), pp.2281–2282 (1977).

[20] Liao S–H.,A., Wang S.: Semiconductor injection lasers with a circular resonator, Appl.Phys.Lett., 36(10), pp.801–803 (1980).

[21] Austin M., Flavin P.G.: Small–radii curved rib waveguides in GaAs/ GaAlAs using Electron–beam lithography, J.Lightwave Techn., Vol.LT–1 (1), pp.236–240 (1983).

[22] Scifres D.R., Burnham R.D., Streifer W.: Grating–coupled GaAs single heterostructure ring laser, Appl.Phys.lett., Vol.28 (11), pp.681–683 (1976).

[23] Sansonetti P., Ribot H., Brandon J., Menigaux L., Dugrand L., Bouadma N.: Low–threshold GaAs/ GaAlAs buried heterostructure laser with an ion–beam–etched quarter ring cavity, Electr.Lett., Vol.23 (10), pp.485–487 (1987).

[24] Jezierski A.F., Laybourn P.J.R.: Integrated semiconductor ring lasers, IEE Proc., Vol.135, pt.J (1) pp.17–24 (1988).

[25] Jezierski A.F. Laybourn P.J.R.: Polyimide–embedded semiconductor ring lasers, 5th European Conference on Integrated Optics, Paris, Paper no.3 (1989). Published in proceedings of SPIE, 1141, 7–11 (1989).

[26] Jezierski A.F., Laybourn P.J.R., Stanley C.R., Roberts J., Lamb J.: Effects of high cavity losses in ring semiconductor lasers, Semiconductor and Integrated Optoelectronics conference, Cardiff, paper no.39 (1989).

[27] Kassim N.M.: private communication, Nottingham University (1989).

[28] Marcatili E.A.J., Miller S.E.: Improved relations describing directional control in electromagnetic wave guidance, The Bell Syst.Tech.J., (9), pp.2161–2188 (1969).

[29] Neumann E.G., Rudolph H.D.: Radiation from bends in dielectric rod transmission lines, IEEE TRans.Microwave Theory and Techniques, Vol.MTT–23 (1), pp.142–149 (1975).

[30] Marcatili E.A.J.: Bends in optical dielectric guides, The bell Syst.Tech.J., (9), pp.2103–2132 (1969).

[31] Marcuse D.: Bending loss of the assymetric slab waveguides, The bell Syst.Tech.J., Vol.15, pp.2551–2563 (1971).

[32] Neumann E.G., Richter W.: Sharp bends with low losses in dielectric optical waveguides, Appl.Opt., Vol.22, pp.1016–1022 (1983).

[33] Geshiro M., Sawa S.: A method for diminishing total transmission losses in curved dielectric optical waveguides, IEEE Trans.Microwave theory Tech., MTT–29, pp.1182–1187 (1981).

[34] Neumann E.G : Curved dielectric optical waveguides with reduced transition losses, IEE Proc., pt.H, Vol.129, pp.278–280 (1982).

[35] Pennings E.C.M., Manhoudt G.H., Smit M.K.: Low–loss bends in planar

optical ridge waveguides, Electr.Lett., Vol.24 (16), pp.998–999 (1988).

[36] Sheem S., Whinnery J.R.: Guiding by single curved boundaries in integrated optics, Wave electr., Elsevier Sc.Publ.Co., Vol.1, pp.61–68 (1974/ 75).

[37] Heiblum M., Harris J.H.: Analysis of curved optical waveguides by conformal transformation, IEEE J.QE–11 (2), pp.75–83 (1975).

[38] Kendall P.C., Stern M.S., Robson P.N.: A new curvature loss formula of Huygense–type for rib waveguides, IEE Proc., Vol.135, pt.J (1), pp.11–16 (1988).

[39] Cullen T.J.: Transmission properties of single–mode Y–junction and bend structures for integrated optics, PhD. thesis, Glasgow University, 1985.

[40] Thurston R.N., Kapon E., Silberger Y.: Analysis of mode separation in multichannel branching waveguides, IEEE J.QE–23 (8), pp.1245–1255 (1987).

[41] Marcuse D.: Radiation losses of tapered dielectric slab waveguides, Bell Syst.Tech.J., 49, pp.273–290 (1970).

[42] Burns, Milton: Mode conversion in planar dielectric separating waveguides, IEEE trans.QE–11, pp.32–39 (1975).

[43] Anderson I.: Transmission performance of Y–junctions in planar dielectric waveguide, Microwaves, Optics and accoustics, Vol.2 (1), pp.7–12 (1978).

[44] Sasaki H., Anderson I.: Theoretical and experimental studies on active Y–junctions in optical waveguides, IEEE J.QE–14 (11), 883–892 (1978).

[45] Kuznetsov M.: Radiation loss in dielectric waveguide Y–branch structures, J.Lightwave Techn., Vol.LT–3 (3), pp.674–677 (1985).

[46] Kapon E., Katz J., Yariv A.: Supermode analysis of phase–locked arrays of semiconductor lasers, Opt.Lett., Vol.10, pp.125–127 (1984).

[47] Sasaki H., Shiki E–I., Mikoshiba N.: propagation characteristics of optical guided waves in asymmetric branching waveguides, IEEE J.QE–17 (6), pp.1051–1057 (1981).

[48] Frenette N.J.P., Cartledge J.C.: The effect of wavefront tilt on mode conversion in asymmetric Y–branch waveguides, IEEE J.QE–25 (4), pp.742–748, (1989).

[49] Forbes R.A., Marom E.: Symmetric directional coupler switches, IEEE J.QE–22 (6), pp.911–919 (1986).

[50] Hanaizumi O., Miyagi M., Kawakami S.: Wide Y–junctions with low losses in three–dimensional dielectric optical waveguides, IEEE J.QE–21 (2), pp.168–173 (1985).

[51] Wang S., Choi H.K., Fattach I.H.: Studies of semiconductor lasers of the interferometric and ring types, IEEE J.QE–18 (4), pp.610–617 (1982).

2. SEMICONDUCTOR MATERIALS CONSIDERED FOR RING LASERS AND THEIR EVALUATION.

2.0. INTRODUCTION.

Ring laser device operation is determined by its material properties. The analysis of laser materials with various designs of light and carrier confinement regions, and their threshold conditions, were undertaken. The structures were: a double heterostructure, a localised gain region separate confinement quantum well material and separate confinement material with an additional passive guide, directionally coupled to the lasing region. The materials with strong light and carrier confinements (due to high index steps and optimised width of the layers) produced minimised threshold current density devices. Reduced confinement, increased loss and reduced cavity lengths resulted in almost proportionally increased threshold current for the double heterostructure lasers, and almost exponentially, for the quantum well structures. Manufactured materials were evaluated and compared by measuring the performance of two-dimensional broad area devices. The threshold currents of typical length quantum well broad area lasers were lower than those of double heterostructure devices, while both operated multimode. The laser material with a passive guide directionally coupled to the lasing region restricted the oscillations and produced single mode operation.

2.1. RING LASER MATERIAL CONFIGURATION.

The new semiconductor ring laser (fig.2.1) uses, as other standard semiconductor lasers, a selected forward biased p-n junction to provide an inversion region, where most atoms are in an excited state [Thompson-1,Panish-2]. On relaxation to the stable ground state, they emit photons. Photons impinging on atoms which are in their excited state induce the stimulated emission of subsequent photons, in phase with the original ones, giving optical gain. Light and carriers are confined in directions transverse to the junction region by the structural and material design of the lasing region. In addition, optical feedback, created by a ring resonant structure, is introduced for a constructive photon-carrier interaction and subsequent lasing oscillation to take place. The biasing is provided by the external metal contacts.

The design of the laser material determines the properties of the final ring laser. All the thin layers are grown on the top of the {100} plane of the GaAs substrate, to allow cleavage of the final devices (section 3.6) (fig.2.2). Both the n-type substrate

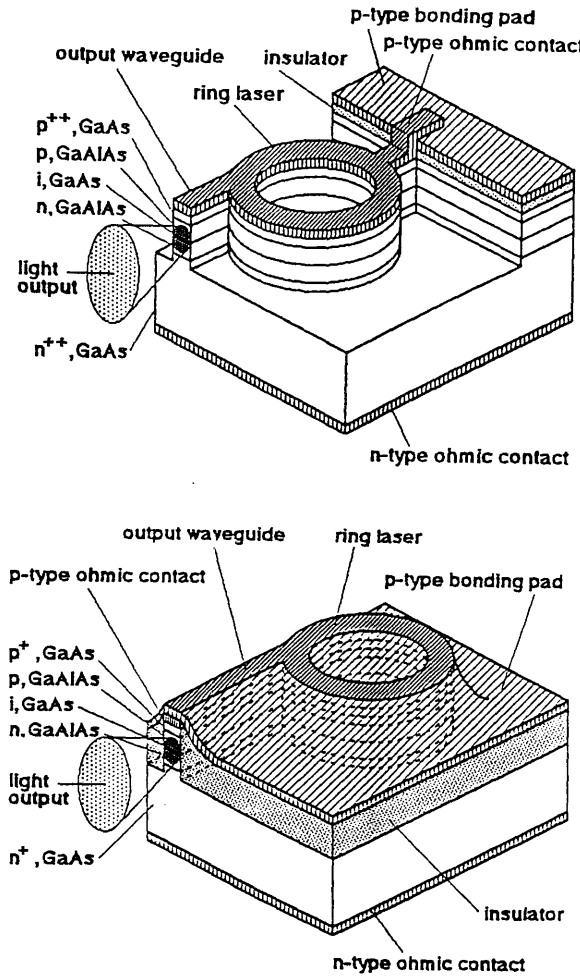

Fig.2.1. Integrated semiconductor ring rib lasers.

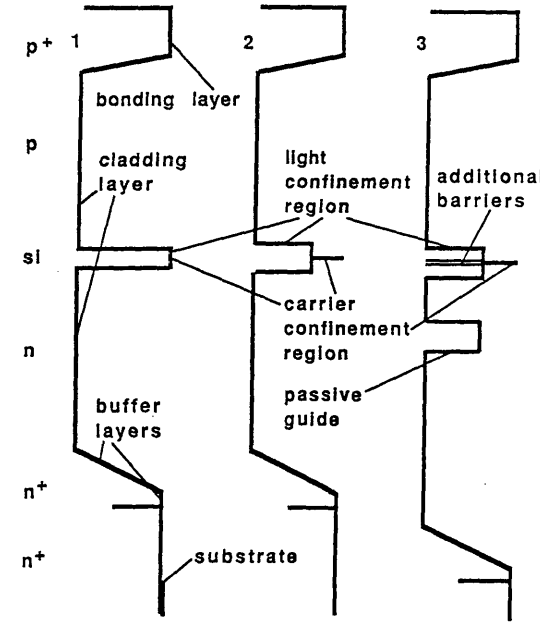

Fig.2.2. Heterostructure laser materials: 1. double heterostructure,
2. localized gain region separate confinement material,
3. localized gain region separate confinement structure with the improved carrier confinement and with coupled passive waveguide.

and the top p− type contact layer should be made of highly doped low band− gap materials to provide ohmic properties to contacts (section 3.3). Above the substrate there is an n− type buffer layer, reducing the influence of the substrate surface damage on the active layer. This buffer layer may be made of a 0.5μm thick layer with properties similar to those of the substrate [Sakaki− 3]; it may consist of a multiple quantum well system of total thickness of 0.2μm [Fujii− 4]; or it may be a structure with smooth transformation from GaAs to AlGaAs [Hersee− 5]. In between the buffer and the contact layers there is a waveguide structure (section 1.1) consisting of the active layer sandwiched between the cladding layers.

Three waveguide structures with different light and carrier confinement regions were designed to produce ring lasers (fig.2.2): a double heterostructure (DH), a localized gain region separate confinement quantum well structure (LGRSCQW) and a localized gain region separate confinement quantum well structure with improved carrier confinement and with a coupled passive waveguide (LGRSCQW− CPW). All the structures incorporate highly doped, n^+ − GaAs substrate and p^+ − contact layers, as well as the intermediate buffer layer, as previously described. The last two materials represent a development of the first structure, replacing a common region confining light and carriers by two separate confinement regions. The last structure provides a way of coupling the light out of the active layer to the passive guide. The laser device made in the configuration of a closed ring resonator cavity possesses more demanding oscillation conditions than the first two structures (section 2.1.3), providing superior spectral characteristics.

2.1.1. Double heterostructure material (DH).

In double heterostructure material [Thompson− 1] an active GaAs layer is sandwiched between n− and p− type cladding AlGaAs layers having a lower refractive index and a higher band− gap [Casey− 6] (fig.2.2). This limits the spread of light, forming an optical waveguide, and decreases diffusion of minority carriers, confining them to the centre layer [Casey− 7, Casey− 6, Thompson− 1]. The shorter wavelength of the absorption edge in the cladding layers provides a loss− free transparent region for the optical wave at the lasing wavelength of the active layer [Casey− 6].

The active layer is highly absorbing for an optical wave of the lasing wavelength [Casey− 8, Thompson− 1]. Injecting carriers into this layer is necessary to make it transparent, by shifting the absorption edge and decreasing the refractive index of the material [Thompson− 1]. Reducing the width of the carrier confinement layer

reduces losses by decreasing the necessary number of injected carriers. However, this also reduces the fraction of the light that travels inside the amplifying region. A compromise is therefore required to achieve a low threshold current material.

Cladding layers must be of sufficient thickness, suitable band–gap and doping in order to avoid considerable carrier loss by leakage over the barrier and to prevent penetration of the light into further layers [Thompson–1]. Any lack of planarity of the layers may additionally result in increased scattering losses. Excessive free carriers result in absorption losses in the ring laser waveguide [Thompson–1, Sell–9].

2.1.2. Localized gain region separate confinement quantum well material (LGRSCQW).

Localized gain region separate confinement heterostructure material (fig.2.2) is a development of a double heterostructure that employs independent regions of light and narrower, carrier confinement [Thompson–10]. A thin carrier confinement region can not confine the light but reduces the number of injected carriers required to support lasing action. The additional thin barrier layers (as in structure 3, Fig.2.2) may improve carrier confinement. The additional, wider light confinement region prevents the excessive spread of the light, which would lead to the reduction of optical confinement, Γ, with the decreased thickness of the active layer [Thompson–1] (section 2.1.1). A graded index configuration is possible and reduces potential barriers at the junction with the adjacent semiconductors [Tsang–11]. The triangular graded index structure may be crudely approximated by a step–like index waveguide with half the thickness of the light confinement region. If the carrier confinement well is narrower than the carrier de Broglie wavelength (20nm), the density of states and energy dependent radiative and non–radiative recombination rates are altered [Holonyak–12]. This dramatically changes the properties of the quantum well structure. A narrower well increases gain, decreases threshold current, reduces temperature sensitivity and considerably reduces the lasing wavelength [Zielinski–13]. In addition, this reduces the proportion of the optical wave interacting with the carriers in the well and increases the loss in the cladding layers due to the reduced lasing wavelength [Thompson–1], which increases threshold current of very narrow quantum well devices. To support lasing action the ring resonators must be of sufficient length, particularly for thin, single well materials (section 2.2.2).

2.1.3. Localized gain region separate confinement quantum well material with a coupled passive waveguide (LGRSCQW– CPW).

The heterostructure laser material may incorporate a passive waveguiding layer, separated from the lasing guiding layer to ensure weak directional coupling (fig.2.2). This enhances the potential for monolithic optical integration. The structure of fig.2.2 additionally incorporates thin barriers which improve carrier confinement and reduce the lasing wavelength.

Light created within the lasing region oscillates within the laser cavity and is coupled to the neighbouring waveguide region, where oscillation may also take place. The coupled– resonator structure possesses slightly different waveguide propagation constants and consequently unequal resonance spectra, depending on the materials and the guide dimensions used. This results in a mode selection of the final structure by favouring the oscillation at the one common resonance and leads towards single– mode operation (fig.2.3) (in a similar way to that in the C^3 laser [Tsang– 14]). Such single mode operation over a high range of the applied currents was confirmed experimentally (section 2.4.4).

Coupling of light between the guides results in a larger effective width of the total light confinement region and improved temperature properties and power handling capabilities of the final device.

The drawback of the coupling between the guides is that a smaller part of the created light is utilised in stimulated emission. Along with the restricted oscillation conditions of the double– resonator, this results in an increased threshold current in the final device (section 2.4.4). The guide coupling ratio varies sinusoidally with the length of the device (section 1.4) and therefore, the threshold current depends critically on the device length. The following description of laser threshold conditions should therefore be modified for the particular structure.

2.2. THRESHOLD CONDITIONS OF THE RING LASER DEVICE.

Current passing through the laser device supports both radiative and non– radiative carrier recombination within the structure [Chinn– 15]. The radiative component is a result of a spectrally dependent modal gain of the spontaneous emission rate (into all angles and polarisations), and possesses sharp features in the mode gain at the transitions from the heavy hole and the light hole. The

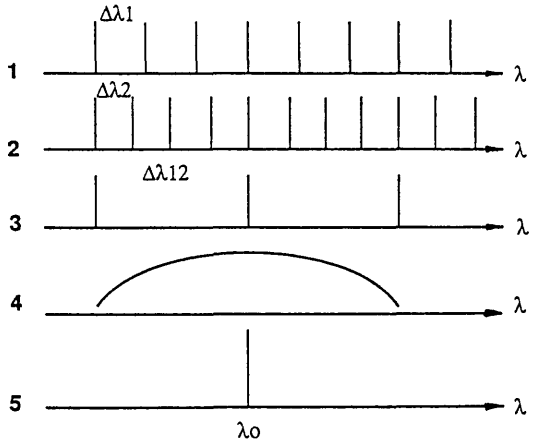

Fig.2.3. Mode selection in a LGRSCQW– CPW laser:
1. allowed optical modes for laser guide, 2. allowed optical modes for passive guide, 3. resultant modes in the coupled cavity guides, 4. gain profile of laser medium, 5. resultant laser spectrum. [similar to C^3 laser, Tsang–14].

non− radiative recombination includes leakage of the carriers over the confining barriers, Auger recombination of the electron− hole states via two− particle interactions and, to a smaller extent, the thermal population within X and L indirect minima band gap recombinations (at high gain and temperature) [Chinn− 15].

The threshold current density for lasing action depends on the gain, g, and the total loss, α, within the structure, and is determined by the optical confinement, Γ, representing a proportion of the optical power in the active region [Thompson− 1]. The necessary overall gain of the laser structure is determined by the distribution of optical intensity within the active and cladding layers, and by the loss for an individual mode. Above the threshold current, the mode gain per unit length, g_{th}, must be sufficient to cancel out all the losses of the optical wave per unit length, α_{total} [Panish− 2]. These are distributed losses due to free carrier absorption within the active layer, α_{fca} and cladding layers, α_{fcc}, scattering losses, α_s, due to imperfections of the guide, losses α_c, due to coupling of the optical wave to external layers through the cladding layers and radiation losses, α_r, due to bends of the stripe three− dimensional system and output coupling losses. Within a ring laser incorporating Y− junction coupling to other optical components, the coupling loss includes scattering and coupling at the Y− junction back to the resonating waveguide. This can be compared to the coupling loss mechanism of a Fabry− Perot structure, where light is lost to the outside media and part of it is reflected back to fulfill the resonating conditions [Thompson− 1; Panish− 2, Tsang− 16] so that:

$$g_{th} = \frac{1}{\Gamma} * \alpha_{total} \qquad (2.1)$$

$$\text{where } \alpha_{total} = \Gamma*\alpha_{fca}+(1-\Gamma)*\alpha_{fcc}+\alpha_s+\alpha_c+\alpha_r+\frac{1}{L}*\ln\left(\frac{1}{1-K}\right)$$

$$= \alpha_{int} + \frac{1}{L}*\ln\left(\frac{1}{1-K}\right) \qquad (2.2)$$

where: α_{total} represents all the losses per unit length due to absorption, scattering, mode coupling, bend radiation and output coupling,

α_{int} is the internal optical loss per unit length,

(1− K) is an output coupling coefficient describing that part of the light transferred back into the resonator,

L is the length of the closed ring optical path.

At the threshold current most of the power is transferred into a few central peaks of the gain curve, which grow rapidly with increased current [Thompson− 1].

The coupled resonator device (section 2.1.3), where light created in the active region

spreads into the additional passive guide, is characterised by decreased optical confinement in the active layer, Γ, increasing the gain, g_{th}, necessary to support lasing action, as confirmed by the experimental results of section 2.4.4. The coupling between the two regions is critically dependent on the uniformity of the structure and the length of the device and therefore the lasing conditions of the structure are difficult to describe.

$\alpha_{fca} \simeq 10$ to $30cm^{-1}$,
$\alpha_{fcc} \simeq 1$ to $20cm^{-1}$, depends on the doping within the cladding layers, other material properties of the cladding layer and the width of the guide,
Γ is the proportion of optical power in the active, carrier confinement region and is a function of d, n, Δn, sections 2.2.1, 2.2.2),
$\Gamma*\alpha_{fca} + (1-\Gamma)*\alpha_{fcc} \simeq 10$ to $30cm^{-1}$, (compared to $2cm^{-1}$, for thin active layer (small Γ) and low doped ($2*10^{17}cm^3$) cladding layers [Tsang-16]),
$\alpha_s \simeq 12cm^{-1}$, for 10nm roughness (dependent on the width of the guide),
α_c is negligible for the thicker cladding layers and a large refractive index step,
$1/L*\ln(1/(1-K)) \simeq 14cm^{-1}$, for L=800$\mu$m, 1-K=0.32,

2.2.1. Double heterostructure.

For DH lasers, the stimulated emission relationship between the maximum gain g_{maxDH} and the injection current density is linear [Thompson−1]:

$$g_{maxDH} = \beta * (J_{nom} - J_o) \qquad (2.3)$$

The equation (2.3) considers a normalised thickness of the active layer while the thickness dependence is introduced into a subsequent equation describing the threshold current density. The gain factor β with unity quantum efficiency, is proportional to 1/T, and

$\beta(293K)=0.045$ [$cm^{-1}/Acm^{-2}\mu m^{-1}$]

β may increase with the index step. J_{nom} is a nominal current density for a 1μm thick active layer; J_o, the value of J_{nom} for which $g_{max} \to 0$, is proportional to $T^{3/2}$ and

$J_o(293K)=4000$ [$Acm^{-2}\mu m^{-1}$]

J_o may be dependent on the index step.

From the above, the threshold current density of a DH laser J_{thDH} is:

$$J_{thrDH} = J_{nom} * \frac{d}{\eta}$$

$$= \frac{d}{\eta} * \{J_o + \frac{g_{th}}{\beta}\} = \frac{d}{\eta} * \{J_o + \frac{\alpha_{totall}}{\beta * \Gamma}\} \qquad (2.4)$$

where: η is the quantum efficiency of the radiative to nonradiative recombination,
d is thickness of the active layer in μm,
Γ is the proportion of the optical power in the active region. Γ depends on the refractive index of the active layer n, the index step between the active and the cladding layer Δn and the thickness of the active layer d (sections 1.1, 2.3).

For the DH laser, the value may be approximated [D. Botez, from Garrett -17] to:

$$\Gamma_{DH} \triangleq \frac{D^2}{2+D^2} = \frac{(\frac{2*\pi}{\lambda_o} * d * \sqrt{\delta\varepsilon})^2}{2+(\frac{2*\pi}{\lambda_o} * d * \sqrt{\delta\varepsilon})^2} \qquad (2.5)$$

where: D is the normalised thickness of the active layer,
λ_o is the freespace wavelength,
$\delta\varepsilon = n_a^2 - n_c^2$ is a dielectric constant. (2.6)

This can be approximated [Nagle—18] by:

$$\Gamma_{DH} \triangleq (\frac{2*\pi}{\lambda_o} * d)^2 * n * \Delta n, \text{ for } d<100\text{nm}. \qquad (2.7)$$

and for d=100nm, n=3.6 and Δn=0.2, $\Gamma_{DH} \simeq 0.38$,
while for d=10nm, n=3.6 and Δn=0.2, $\Gamma_{DH} \simeq 0.0038$.

The decreased confinement factor, Γ, requires an increased gain for lasing action. The threshold current density of the DH increases if the active layer is too thick, where the component $(d*J_o/\eta)$ dominates, or if the active layer is too thin (<<100nm), where the increasing loss component dominates (fig.2.4). Introducing (2.2), (2.5) and (2.6) to (2.4):

$$J_{thrDH} \simeq \frac{d}{\eta} * \left[J_o + \frac{[\alpha_{int} + \frac{1}{L} * \ln(\frac{1}{1-K})] * \{2 + [\frac{2*\pi}{\lambda_o} * d * \sqrt{(n_a^2 - n_c^2)}]^2\}}{\beta * [\frac{2*\pi}{\lambda_o} * d * \sqrt{(n_a^2 - n_c^2)}]^2} \right] \qquad (2.8)$$

Similarly very narrow lossy stripes should require increased gain and result in

increased threshold current density.

Example: for d=0.15μm, η=0.7, J_o=4000Acm$^{-2}\mu$m^{-1}, α_{int}=10cm^{-1}, L=0.08cm, 1-K=0.32, λ=0.87μm, n_a=3.6, n_c=3.25 and β=0.045cm^{-1}/Acm$^{-2}\mu$m^{-1} $\Rightarrow$ J_{thDH}=1054A/cm^2.

The optimum thickness of the active layer providing a minimum threshold current density can be calculated from:

$$\frac{\delta}{\delta d}(J_{thrDH}) = 0 \qquad (2.9)$$

A very low loss guide would result in a decreased value of the optimal thickness of the active layer d_{opt} to produce a minimal threshold current density $J_{thrDHmin}$ of the laser (fig.2.4). In section 2.3.4., the optimum width of the active layer, d_{optd}, is estimated from the normalised thickness of the active layer, providing the minimal normalised effective width of the optical field of the zero order mode within the particular waveguide [Thompson–1].

The optimum thickness of typical structures is then between 0.15 and 0.22μm. The value is overestimated, in particular for low loss devices, but prevents the excessive spread of light into the cladding layer and subsequent loss of light penetrating further layers. Very thin active layer would then require very thick cladding layers.

The dependence of the threshold current density on the ring path length of the device is presented in fig.2.5.

The threshold current I_{thDH} is then:

$$I_{thDH} = J_{thrDH} * L_d * s \qquad (2.10)$$

Note that J_{thrDH} depends on α_{total}, which in turn depends on the device length L_d and the width s. A sharp bend or very narrow guide results in increased α_{total} due to bend radiation, poor light confinement, increased scattering losses and absorption loss within the area outside the guide (section 1.6). This will result in increased J_{thrDH} and I_{thDH}, and has been confirmed experimentally in section 4.3.4.3. The dependence of threshold current on the ring path length of the device is presented in fig.2.6.

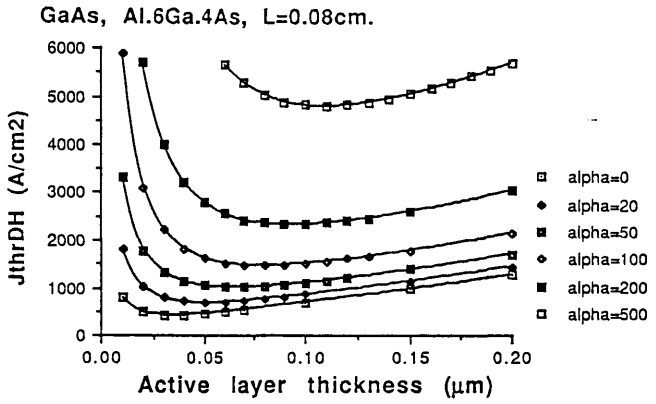

Fig.2.4. Dependence of the threshold current density of the DH on the thickness of the active layer, for various losses within the structure.

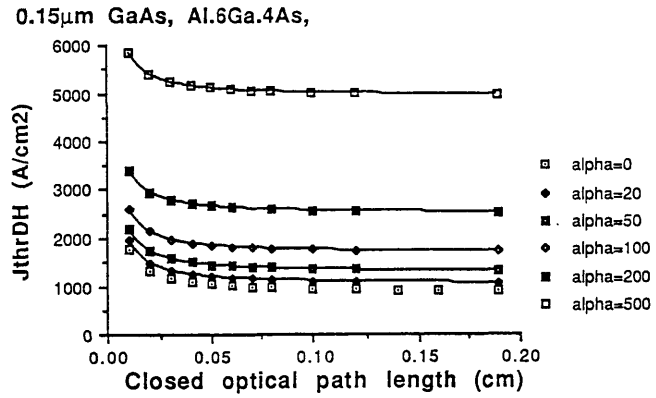

Fig.2.5. Dependence of the threshold current density of the DH on the ring path– length of the device, for various losses within the device.

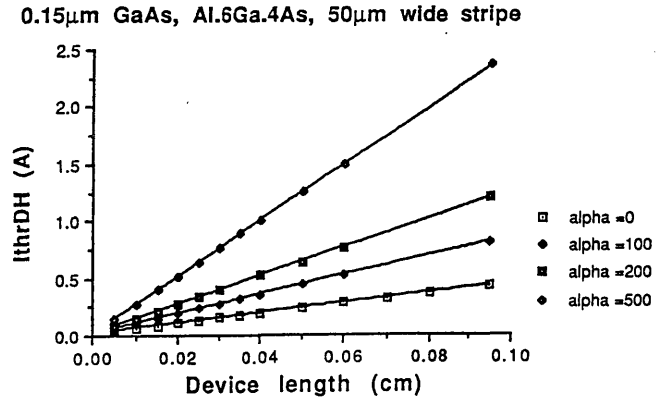

Fig.2.6. Dependence of the threshold current of the DH on the length of the device, for various losses within the structure.

2.2.2. Separate confinement quantum well structure.

Threshold conditions of quantum well lasers are not readily found in the textbooks. Unlike the case for double heterostructures, the stimulated emission relationship between the maximum gain g_{maxDH} and the injection current density in quantum well lasers (with thin wells) is nonlinear [Wilcox−19, Chinn−15, McIlroy−20]. The approximate logarithmic dependence of the gain−current density curve may be due to gain saturation in sub−bands with a constant density of states and an increased nonradiative Auger recombination rate at high carrier concentration; (leakage and L−valley recombination contributions to carrier loss were found to be small) [Wilcox−19]:

$$g_{maxscQW} \approx J_o*b * \ln(\frac{J_{nom}}{J_o}) = J_o*b * \ln[1+\frac{J_{nom}-J_o}{J_o}]$$

where: $g_{maxscQW} > 0$, (2.11)

J_{nom} is the nominal current density of the particular structure. Lack of normalisation, particularly on the thickness of the well as was the case in DH laser theory, means that the dependence of the subsequent threshold current density on the thickness of the well can not be easily seen. In the equation: J_o is a nominal current at transparency, and is temperature and structure dependent (including a thickness of the active layer), and b is the gain−current coefficient, increasing with the index step.

At small currents ($J_{nom}\rightarrow J_o$, $(J_{nom}-J_o)/J_o<1$, $\ln(1+x)_{x\rightarrow 0}\approx x$) the gain−current dependence (2.11) is approximately linear and similar to the DH laser:

$$g_{maxscQW(Jo)} \approx b * (J_{nom}-J_o) \quad (2.12)$$

Typical values of J_o and J_o*b, at 300K are presented in table 2.1.

Because a smaller proportion of light is confined to the thin active region of a QW laser, compared to the much wider DH laser, light travels mostly outside the highly absorbing region and the structure produces a higher level of optical power at a given gain. This results in a steeper light−current characteristic and a larger spontaneous emission, compared to a DH laser.

The total gain g_{maxN} for the N wells is approximately N times greater than the gain of an individual well g_{max1} [Arakawa−21, Arakawa−22], resulting in a threshold current density approximately N times larger:

$$g_{maxN} \approx N*g_{max1} \quad (2.13)$$

$$g_{max1} \approx \frac{1}{N*\Gamma_w}*\alpha_{total} = \frac{1}{N*\Gamma_w}*\{\alpha_{int}+\frac{1}{L}*\ln(\frac{1}{1-K})\} \quad (2.14)$$

$$J_N \approx N*J_1 \quad (2.15)$$

From the above, the threshold current of the QW laser J_{thrQW} is approximately given by:

$$J_{thrQW} \approx J_{nom} * \frac{N}{\eta}$$

$$\approx \frac{N}{\eta} * J_o * \exp[\frac{g_{thNQW}}{b*J_o}]$$

$$\approx \frac{N}{\eta} * J_o * \exp[\frac{\alpha_{totalQW}}{b*\Gamma*J_o}] \quad (2.16)$$

where J_o is both temperature and structure dependent.

Table 2.1. Examples of values of J_o and J_o*b.

GRIN	Well width	J_o*b	J_o	Reference
2x0.15μm thick from $Al_{.2}Ga_{.8}As$ to $Al_{.4}Ga_{.6}As$	7nm	$626.4cm^{-1}$	$40A/cm^2$	Wilcox-19
Typical	10nm	$690cm^{-1}$	$66A/cm^2$	Garrett-17
2x0.2μm thick from $Al_{.2}Ga_{.8}As$ to $Al_{.4}Ga_{.6}As$	5nm	$24.47cm^{-1}$	$123.6A/cm^2$	Chinn-15
2x0.15μm from $Al_{.33}Ga_{.67}As$ to $Al_{.71}Ga_{.29}$	7.5nm	$41.18cm^{-1}$	$102.4A/cm^2$	Chinn-15
2x0.1μm $Al_{.2}Ga_{.8}As$ between $Al_{.5}Ga_{.5}As$	7.5nm	$1195cm^{-1}$	$180A/cm^2$	McIlroy-20 Kurobe-27
$Al_{.2}Ga_{.8}As$ between $Al_{.7}Ga_{.3}As$	7.5nm	$1200cm^{-1}$	$400A/cm^2$	Saint-25

Thin carrier confinement wells do not disturb the light confinement region, and the confinement of the light to the wells is approximately proportional to their total thickness d for non-interacting QWs for both step-like (Γ_{Scstep}) and gradient (Γ_{scgrad}) confined structures [Arakawa-21, Arakawa-22, Nagle-18, Kasemset-23,

Blood– 24]. Thus for typical structures with optical waveguide thickness of L_o=1000A:

$$\Gamma_{Scstep} \approx \frac{0.3}{L_o} * d\ (A) \approx N * \Gamma_{scstepsqw} \qquad (2.17)$$

where: $d = N * L_w$, is the total thickness of the N well of the L_w thickness each, (2.18)

$\Gamma_{scstepsqw}$ is confinement to the single well,

e.g. for d=10nm, $\Gamma_{scstep} \simeq 0.03$.

The value of Γ_{scstep} depends on the refractive index step and varies with barrier thickness [Saint– Crico– 25].

$$\Gamma_{scgrad} \approx \frac{\sqrt{(\frac{2}{\pi})}}{W_o} * d = N * \Gamma_{scgradsqw} \qquad (2.19)$$

where: $W_o = \sqrt{(\frac{\lambda * x_\varepsilon}{\pi * n_o})}$ (2.20)

$$x_\varepsilon = \frac{x_c}{\sqrt{[1-(n_b/n_c)^2]}}$$

$n = n_o * \sqrt{[1-(\frac{x}{x_\varepsilon})^2]}$, is the index distribution of the parabolically graded waveguide,

n_b, n_c are the refractive indexes of the bottom of the barrier and confinement layers,

x_c is the distance from the bottom to the top of the barrier,

$\Gamma_{scgradsqw}$ is the confinement to the single well.

Consequently, introducing (2.2), (2.17) to (2.16), the threshold current density is:

$$J_{thrQW} \simeq \frac{N}{\eta} * J_o * \exp\left[\frac{[\alpha_{int} + \frac{1}{L} * \ln(\frac{1}{1-K})] * L_o}{b * J_o * 0.3 * N * L_w(A)}\right] \qquad (2.21)$$

The equation (2.21) is structure dependent and refers to typical 10nm thick well, and typical barrier and cladding layers. It does not allow estimation of the influence of well thickness on the threshold current density.

Bear in mind that the values of J_o and gain $J_o * b$ presented by various authors are based on experimental results refering to particular structures and assuming a known value of loss α_{int}. From the analysis of [Saint– Crico– 25, Kasemet– 23, Sagimura– 26], J_{nom} is proportional to the rate of spontaneous emission R_S,

elementary charge e and quantum well width L_w:

$$J_{nom} \simeq e*R_s*L_w \qquad (2.22)$$

Thus, more generally, the dependence of J_{thrQW} on the well thickness of a typical QW laser is suggested to be (fig.2.7):

$$J_{thrQW} \simeq \frac{N}{\eta}*J_o*\frac{L_w}{100}*\exp\left[\frac{[\alpha_{int} + \frac{1}{L}*\ln(\frac{1}{1-K})] * L_o}{b * J_o * 0.3 * N * L_w(A)}\right] \qquad (2.23)$$

Example: For N=1, η=0.8, J_o=66A/cm^2, α_{int}=10cm^{-1}, L=0.08cm, 1-K=0.32, b*J_o=690cm^{-1}, L_o=1000A and L_w=76A $\Rightarrow$ $J_{thrQW} \simeq$293A/cm^2.

The equation (2.23) agrees well with the data presented by various authors mentioned in the section. There is an optimum value of thickness and number of wells, about which the threshold current density increases for both increased or decreased values. For low loss structures, the threshold current density for a QW laser increases rapidly for layers thinner than about 5nm and slowly, for thicker wells [Sagimura– 26, Saint– Crico– 25] (fig.2.7). The optimal QW thickness value is lower for increased number of wells. Lossy waveguides shift the optimum towards a higher value. The optimal value of the active layer thickness of the low loss QW laser is much smaller than that of DH lasers. The additional confinement layers prevent excessive spread of the light away from the lasing region and allow cladding layers of reasonable thickness to be applied (see section 2.2.1) to prevent excessive losses.

From the equation (2.23) the threshold current density increases rapidly with decreasing ring path length of the laser or increased loss [Kurobe– 27, Reisinger– 28]. The minimum ring length providing low threshold current density decreases rapidly with increased number of wells, particularly for lossy guides, although structures with a larger well number may have a higher threshold current density for longer devices (fig.2.8).

The optimum number of wells to provide the minimum threshold current density may be calculated, taking into account the decrease in the current density with increased number of wells. It is dependent on length = f(α), loss and confinement parameters of the guide [Garrett– 17]:

$$N*(N+1)*\ln[\frac{1+N}{N}] \cong N_{opt} = \frac{\alpha_{total}}{\Gamma_{sqw}*b*J_o} \qquad (2.24)$$

For the ring path length of 600 to 800μm, the optimum number of wells of 7.6nm thick, ranges from 2 to 8 with increasing guide loss.

The threshold current I_{thQW} is then:

$$I_{thQW} = J_{thrQW}*L_d*s \qquad (2.25)$$

Note, that J_{thrQW} depends on α_{total} which in turn depends on both device length L_d and width of the device s. Similarly, as in the case of DH laser, within a QW laser a sharp bend or very narrow guides result in an increased α_{total} due to bend radiation, poor optical confinement, increased scattering loss and absorption within the area outside the guide. This would increase J_{thrQW} (fig.2.8) and I_{thrQW} (fig.2.9). The relation was confirmed experimentally (section 4.3.4.3).

The minimum threshold current L_d*s*J_{thr} is achieved for a ring path length L_{opt} [Garett– 17]:

$$L_{opt} \approx \frac{\ln[\frac{1}{1-K}]}{b*J_o*\Gamma_{sqw}*N} \qquad (2.26)$$

The optimal ring path length decreases with an increased number of wells [Sagimura– 26, Kurobe– 27]. Devices with a longer ring path made of material with more wells may result in increased current however (fig.2.9). The dependence of current on the number of wells, determining a total thickness of the active region, is presented in fig.2.10.

2.2.3. Summary of threshold conditions for DH and QW structures.

Let us consider the influence of losses due to the narrowness of the structure and the limited length of the device on the threshold current density of DH and QW devices, and compare it with experimental results.

Because the high output coupling loss is comparable to the mirror loss in a cleaved cavity laser, a similar approach to the threshold current may be used. The gain required from DH and MQW structures at threshold may be expressed as [Panish– 2, Kurobe– 27]:

$$\text{DH:} \qquad \Gamma_{DH}*G_{DH} = \alpha + \frac{\ln(1-K)^{-1}}{L} \qquad (2.27)$$

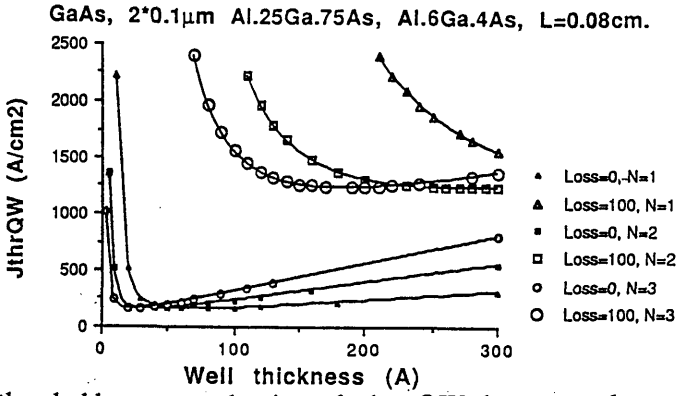

Fig.2.7. Dependence of the threshold current density of the QW laser on the total thickness of the wells (number of wells), for various losses within the structure.

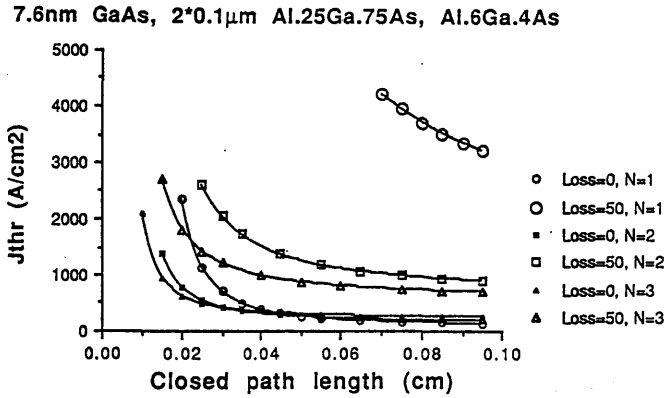

Fig.2.8. Dependence of the threshold current density of the QW laser on the ring path– length of the device, for various losses within the structure.

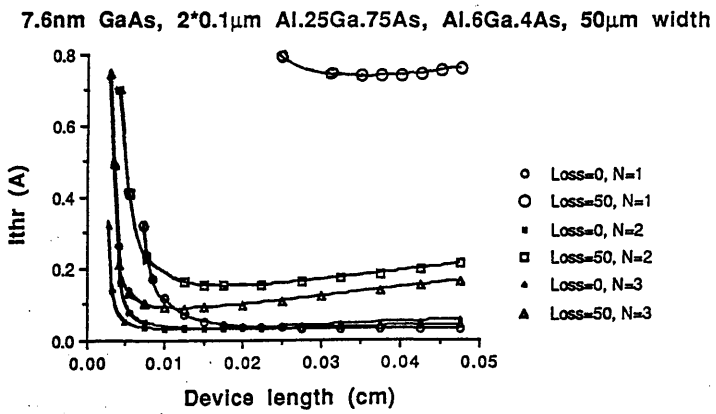

Fig.2.9. Dependence of the threshold current of the QW laser on the length of the device, for various losses within the structure.

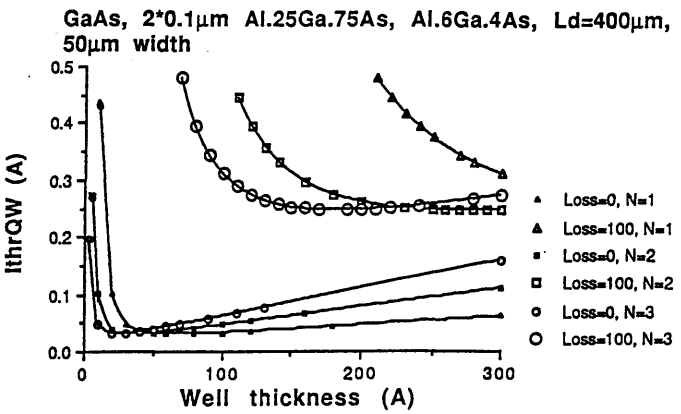

Fig.2.10. Dependence of the threshold current of QW laser on the total thickness of the wells (number of wells), for various losses within the structure.

$$\text{MQW:} \qquad N*\Gamma_w*G_w = \alpha + \frac{\ln(1-K)^{-1}}{L} \qquad (2.28)$$

where N, Γ_w and G_w are the number, optical confinement factor and optical gain per unit length of the quantum wells, α is the internal optical loss per unit length, L is the cavity length (ring circumference) and K is the output coupling loss.

The threshold current density of narrow DH and MQW structures can be presented as [Garrett−17, Wilcox−19, Arakawa−21] (sections 2.2.1, 2.2.2):

$$J_{thrDH} \simeq \frac{d}{\eta}*\left[J_o+\frac{[\alpha_{int}+\frac{\ln(1-K)^{-1}}{L}]*\{2+[\frac{2*\pi}{\lambda_o}*d*/(n_a^2-n_c^2)]^2\}}{\beta*[\frac{2*\pi}{\lambda_o}*d*/(n_a^2-n_c^2)]^2}\right] \qquad (2.29)$$

$$J_{thrQW} \simeq \frac{N}{\eta}*J_o*\frac{L_w}{100}*\exp\left[\frac{[\alpha_{int}+\frac{\ln(1-K)^{-1}}{L}]*L_o}{b*J_o*0.3*N*L_w(A)}\right] \qquad (2.30)$$

where: b and β are gain current coefficients,

η is the radiative to nonradiative quantum efficiency,

J_o is the value of J_{nom}, for which $g_{max}\to 0$,

L_w, d are well and active layer thicknesses,

L_o is the weighted light confinement region thickness (1000A)

From the expressions, the DH threshold current density increases with increased loss and decreased length of the device (fig.2.5). The threshold current density is increased for lossy devices. The MQW threshold current density increases at a much faster rate with decreased length or increased loss, since the relation is exponential (fig.2.8). Both lossy (e.g. due to narrowness of the bend structures) and very short devices increase the threshold current density above the reasonable measurable level. The advantage of the QW lasers of providing lower threshold current density than the DH lasers applies therefore to low loss devices only. The threshold current density decreases rapidly with increased number of applied wells or thicker well unless longer devices are considered (fig. 2.10). The increased total well thickness leads however to the DH laser regime with the additional light confinement region limiting the spread of light to the cladding regions and therefore their necessary thickness.

The threshold current of narrow DH and MQW structures can be presented then as (sections 2.2.1, 2.2.2):

$$I_{thrDH} \simeq \frac{d}{\eta} * \left[J_o + \frac{[\alpha_{int} + \frac{\ln(1-K)^{-1}}{L}] * \{2 + [\frac{2*\pi}{\lambda_o} * d * / (n_a^2 - n_c^2)]^2\}}{\beta * [\frac{2*\pi}{\lambda_o} * d * / (n_a^2 - n_c^2)]^2} \right] * L_d * s \qquad (2.31)$$

$$I_{thrQW} \simeq \frac{N}{\eta} * J_o * \frac{L_w}{100} * \exp\left[\frac{[\alpha_{int} + \frac{\ln(1-K)^{-1}}{L}] * L_o}{b * J_o * 0.3 * N * L_w(A)} \right] * L_d * s \qquad (2.32)$$

where: s and L_d are the width and the length of the guide.

Note particularly, that very narrow bend guides may result in excessively increased α_{int} due to poor optical confinement and loss of a large part of the field.

The threshold current of DH increases with loss and is almost proportional to length of the device. The threshold current of MQW possesses a minimum and increases rapidly for shorter device length; lossy devices rapidly shift the minimum towards a greater value of the length (fig.2.9). This can be compensated with an increased number of wells, or thicker wells within the structure, although the threshold current for longer devices may then be larger than for similarly long single well devices.

2.2.4. Second and higher quantised state operation of the quantum well laser.

The gain needed to overcome the very high losses within the quantum well structure and produce a lasing action, requires an excessively high threshold current density. This is observed within the shorter cavity laser material, with a small number of wells, short and narrow bend lasers, and other lossy structures.

The modal gain spectra at increased pumping level were calculated by Chinn, Zory and Reisinger [15]. Mittlestein and Yariv in [29] presented the approximate equations describing the modal gain of the one–dimensional carrier confinement within the quantum well laser. For the first two states, taking into account band broadening:

$$g(E) = A * \sum_{n=1}^{2} \frac{1}{\exp[(E_n - E) * S / \Delta E] + 1} * [2 * f_c(E) - 1] \qquad (2.33)$$

where: $f_c(E) = \dfrac{1}{\exp\left(\dfrac{(E-E_g)*S - E_{fc}}{kT}\right) + 1}$

A is the maximum available modal gain per state,

E_g is band–gap energy of bulk GaAs,

S is total band offset,

T is the device temperature,

The quantum well device introduces one dimensional carrier confinement, resulting in a staircase–like function of the density of states. With increased gain, its spectrum broadens around the electron–to–heavy hole transition energy. A lossy device requires a larger gain for lasing action. The spectrum broadens with a higher pumping level, reaching the electron–to–light hole transition, where a new peak develops, at a wavelength shorter by about 8 to 15nm [Yuasa–30]. A very lossy device requires a still larger pumping level and this causes further broadening of the gain spectrum, until the second electron–to–heavy hole transition energy is achieved. By adding gain from both first and second states at the second quantised state energy, a new gain peak rapidly develops and becomes dominant, at a wavelength shorter than that of the first state by about 60nm. A structure discussed throughout this thesis, incorporating the 7.6nm well and barriers made of $Al_{.25}Ga_{.75}As$, cannot support other transitions (fig.2.11). Experimental results are presented in section 4.3.4.4.2. A wider well or smaller barriers may result in further, higher order states. The shift of the gain peak occurs for devices with high losses or at high temperature which demand excessive gain and greatly increased threshold current, e.g. due to the shorter length. Thicker quantum wells and an increased number of wells result in structures which may be much shorter before they become very lossy and introduce a gain peak shift (section 2.2.2). Small spectral peak shifts due to increased temperature of the heavily pumped device are followed by a large shift due to the increasing pumping level.

Double heterostructures have a continous function of the density of states within the wide active region. With increased pumping level and therefore increased temperature there is a shift of the spectral peak wavelength (section 4.3.4.4). The shift is larger than in the case of the quantum well lasers. There is no large wavelength shift, as is observed due to the increased gain at the second quantised state within the quantum well devices, because the density of states within the larger devices is not a step–function.

Both low– and high–loss double heterostructure and quantum well devices were produced and experimental results confirmed the theoretical prediction of the higher state operation (section 4.3.4.4).

2.3. RING LASER MATERIAL DESIGN.

The properties of optical waveguide produced within the GaAs/AlGaAs system rely on the temperature dependent energy gaps of the materials used, their configuration, thicknesses and doping. The emission energy of such a ring laser structure is shifted from that of the active layer, due to a several angstroms thick gradient at the well– barrier interface, which becomes significant for a very thin active layer. The emission wavelength determines the refractive indices of the materials used. The structure incorporating quantum wells may require calculation of its weighted refractive index. A three– dimensional waveguide requires additional calculations of effective refractive index of the central layer. The knowledge of refractive indices allows calculation of optimum widths of the layers forming an optical waveguide.

Throughout this section there are relevant calculations of the double heterostructure and the quantum well laser materials presented in section 2.1 (fig.2.2).

2.3.1. Semiconductor energy band– gaps, emission energy and wavelength of the laser structures.

The direct bandgap $E_g{}^{d}{}_{GaAs}$ and indirect bandgaps $E_g{}^{x}{}_{GaAs}$ and $E_g{}^{l}{}_{GaAs}$ within the GaAs are temperature dependent (Casey and Panish, and Aspnes [Blakemore– 31]) (fig.2.12):

$$E_g{}^{d}{}_{GaAs}(T) = 1.519-5.405*0.0001*\frac{T^2}{T+204} \text{ [eV]} \qquad (2.34)$$

$$E_g{}^{x}{}_{GaAs}(T) = 1.981-4.6*0.0001*\frac{T^2}{T+204} \text{ [eV]} \qquad (2.35)$$

$$E_g{}^{l}{}_{GaAs}(T) = 1.815-6.05*0.0001*\frac{T^2}{T+204} \text{ [eV]} \qquad (2.36)$$

The lowest of the direct or indirect bandgaps determines the recombination within the material. The radiative recombination of light, necessary in the laser structures within the active layer, exists for materials with the direct bandgap smaller than the indirect bandgap. This is satisfied within the GaAs structure.

The energy bandgap for $Al_xGa_{1-x}As$ at a chosen temperature was suggested by [Casey and Panish– 32, Adachi– 33] (fig.2.13):

$$E_g^d{}_{Al(x)Ga(1-x)As}(T,x) = E_g^d{}_{GaAs}(T)+1.247*x \text{ [eV]}, \text{ for } 0 \leqslant x \leqslant 0.45$$

$$= E_g^d{}_{GaAs}(T)+1.247*x+1.147*(x-0.45) \text{ [eV]}, \text{ for } x \geqslant 0.45, \quad (2.37)$$

$$E_g^x{}_{Al(x)Ga(1-x)As}(T,x) = E_g^x{}_{GaAs}(T)+0.125*x+0.143*x^2 \text{ [eV]}, \quad (2.38)$$

$$E_g^l{}_{Al(x)Ga(1-x)As}(T,x) = E_g^l{}_{GaAs}(T)+0.642*x \text{ [eV]} \quad (2.39)$$

Examples are presented in table 2.2.

Table 2.2. The lowest band gap within various materials at 297K.

$E_g^d{}_{GaAs}$	1.423837 eV
$E_g^d{}_{Al(.25)Ga(.75)As}$	1.735586 eV
$E_g^l{}_{Al(.6)Ga(.4)As}$	2.02649 eV

At room temperature, the AlGaAs system exhibits a smaller direct than indirect energy gap for less than 42% aluminium concentration, and a larger gap for higher values (fig.2.13). The materials are of poor quality for concentrations of Al exceeding 60% [Thompson– 1]. The minimum practical energy step between active and cladding layers, providing confinement of the light and carriers to the active layer (for practical thicknesses of the central layers) is 0.3eV [Thompson– 1]. This corresponds to a concentration step of about 25 to 40% in Al (fig.2.13). Hence the maximum allowed Al concentration within the active layer is about 20%, limiting the minimum wavelength of the laser, unless quantum well structures, which introduce an additional wavelength shift, are used.

The emission energy of the very thin (<15nm) active well sandwiched between the barriers with a higher energy bandgap is strongly increased, probably due to a gradient several angstroms thick at the heterointerface of the well– barrier [Kawai– 34]. Calculations of the system require the solution of the equation [Kawai– 34]:

$$\tan^2\{[m_w*E*L_z^2/(2*\hbar^2)]^{1/2}\} - m_b*(V-E)/(m_w*E) = 0 \quad (2.40)$$

where: E is an eigenvalue in the one– dimensional finite square potential well,

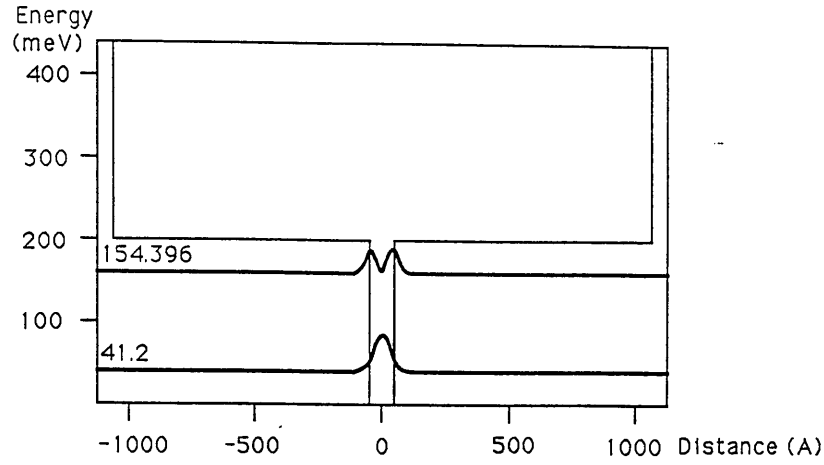

Fig.2.11. Available density of states within the 7.6nm GaAs well sandwiched between $Al_{.25}Ga_{.75}As$ cladding layers [After Pepin J., Glasgow University, 1989].

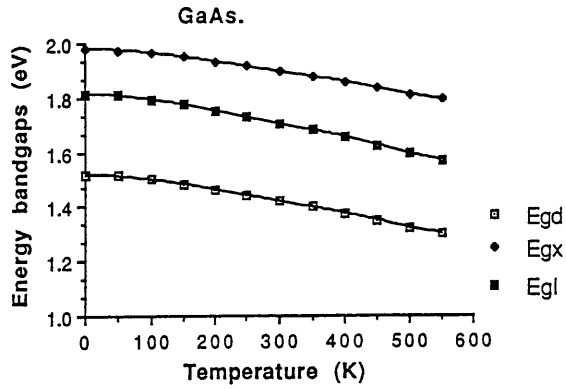

Fig.2.12. Temperature dependence of direct and indirect band– gaps of GaAs.

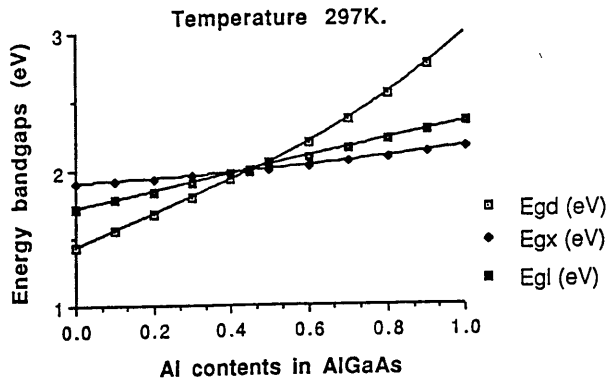

Fig.2.13. The energy band– gaps of $Al_xGa_{1-x}As$ materials at room temperature.

m_b, m_w are barrier and well particle masses,
L_z is a well width,
V is a barrier height.

The calculation (2.40) considers spectral broadening due to intraband relaxation and few-step recombination, which results in an effective band-gap shrinkage at high carrier densities [Chinn-15]. The solutions were computed using a program written by Bhumbra [35] and were compared with a simple, temperature dependent empirical equation, accurate for active regions thicker than 20nm (fig.2.14):

$$E_{peak}(T) = \frac{E_g{}^d{}_a*(L_z-5.66) + E_{b1}*5.66 + E_{b2}*5.66}{L_z+5.66} \qquad (2.41)$$

where: E_{peak} is an emission energy of the QW system,
$E_g{}^d{}_a$, E_{b1}, E_{b2} are energy gaps of the active and barrier layers,
$E_g{}^d{}_a < E_g{}^x{}_a$, $E_g{}^d{}_a < E_{b1}$, $E_g{}^d{}_a < E_{b2}$,
$L_z > 5.66$ is in Angstroms.

The examples of the simple calculations (2.41) are presented in table 2.3.

Table 2.3. Emission energy peak at 297K.

Active layer	Cladding layers	E_{peak}	λ
1520A GaAs	$Al_{.6}Ga_{.4}As$	1.428308 eV	0.8674597μm
76A GaAs	$Al_{.25}Ga_{.75}As$	1.467053 eV	0.8445505μm

For wells thinner than 10nm, the energy calculated using a simple empirical equation is smaller than that obtained from the exact solution, and corresponds to an emission wavelength longer by about 3nm than that of the exact solution (10°C difference in temperature). The practical devices often lase at a wavelength between these limits. Considering the fact that the operating temperature of the real junction of the laser is higher than the temperature of the environment, the exact solution seems to be more realistic. On the other hand, for simplicity, the empirical equation was found to be useful.

Note that Kawai's equations apply to very thin wells only. For a 22.7nm well, the solution exceeds the empirical equation solution (and the experimental value of the emitted wavelength) by 8nm, and for a 200nm thick junction, the calculated emitted

wavelength value is higher than 1200nm, which totally disagrees with experimental results. On the other hand, the experiments prove that the double heterostructure lases at a junction temperature of about 70°C to 95°C, which can be supported with theoretical calculation of the temperature drop across the semiconductor wafer (Appendix 2).

The emission wavelength $\lambda(T)$ of the laser device is then (fig.2.14) (Table 2.3):

$$\lambda(T)[\mu m] = \frac{1.239}{E_{peak}(T)[eV]} \qquad (2.42)$$

or approximatly for thicker layers: $\lambda(T) = \frac{1.239}{E_g{}^{d}{}_{a}(T)}$

At room temperature, the emission wavelength of the experimental devices shifted by about 0.28nm/°C for both DH and QW structures (Appendix 2).

2.3.2. Refractive index of laser materials and the influence of wavelength and doping.

For the lasing wavelength, the refractive index $n_{Al(x)Ga(1-x)As}$ of the active and cladding layers may be calculated to facilitate analysis of the experimental waveguide [V.Evtuhov, A.Yariv, Sellmeier equations– 36], fig.2.15:

$$n_{Al(x)Ga(1-x)As} = \sqrt{(A+B-C)} \qquad (2.43)$$

where: $A = 10.906 - 2.92*x$

$$B = \frac{0.97501}{\lambda^2-(0.52886-0.735*x)^2}$$

for $x \leqslant 0.36$,

$$= \frac{0.97501}{\lambda^2-(0.30386-0.105*x)^2}$$

for $x \geqslant 0.36$,

$C = 0.002467*(1.41*x+1)*\lambda^2$.

Examples are presented in table 2.4.

Table 2.4. Refractive indexes of AlGaAs systems at 297K.

λ	n_{GaAs}	$n_{Al(.25)Ga(.75)As}$	$n_{Al(.6)Ga(.4)As}$
0.8674597μm	3.600886		3.248774
0.8445505μm	3.62671	3.437237	3.261709

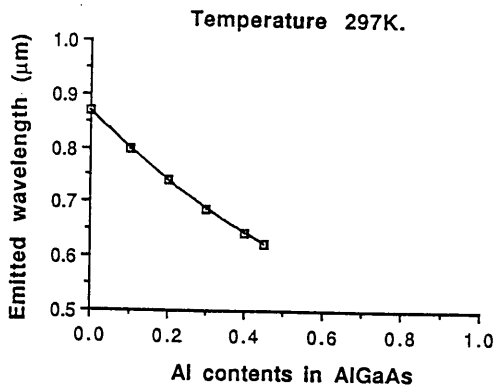

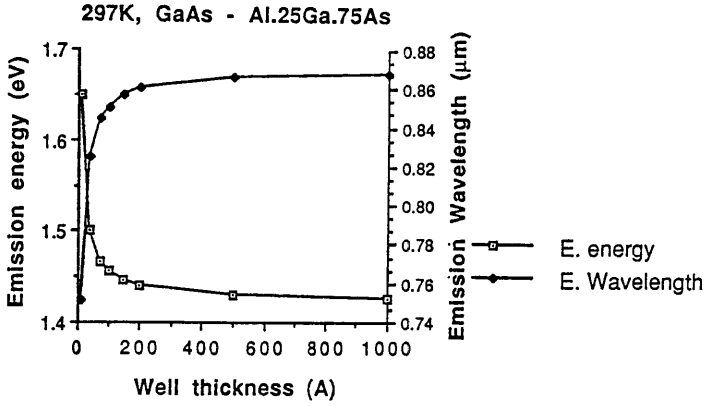

Fig.2.14. Emission energy and wavelength dependence on the thickness of GaAs well sandwiched between $Al_{.25}Ga_{.75}As$ at room temperature, calculated using a simple approximation.

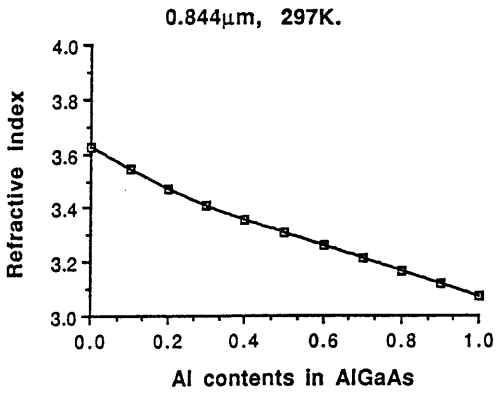

Fig.2.15. The refractive index of AlGaAs material at room temperature and a chosen wavelength.

The refractive index is affected by the presence of carriers. It becomes complex and decreases, due to the interaction of carriers with the optical wave (plasma effect) and a band to band interaction [Thompson−1]. For practical values of the carrier concentration present within the laser structures, this may be neglected [Sell−9, Thompson−1, Cross−37]. Free carriers in the waveguide introduce optical absorption proportional to the carrier concentration and this is significant for doping above about $10^{18}/cm^3$ [Tsang−16]:

$$\alpha_{GaAs}[cm^{-1}] = 3*10^{-18}*n_o+7*10^{-18}*p_o, \qquad (2.44)$$

The undoped or p−type−doped active layer results in high efficiency lasers and produces a concentration of injected carriers of $10^{18}/cm^3$ [Thompson−1]. This is considerably degraded for an n−type doped active layer.

Doping of the cladding layers being between $2*10^{17}$ and $10^{18}/cm^3$ provides low absorption loss and maintains low leakage and proper carrier confinement [Thompson−1]. At the same time, for typical structures, the thickness of the cladding layers should be larger than 1.5μm, to reduce leakage of carriers and spread of the optical field beyond the waveguide, since this would reduce the efficiency of the photon−carrier interaction (section 1.4).

2.3.3. Weighted refractive index of the materials incorporating quantum wells and effective refractive index of the stripe ring or straight waveguide structure.

The weighted refractive index of the light confinement region incorporating quantum wells can be calculated [McBeans−38, Blakemore−31]:

$$n_{aw} = \frac{n_a^2*d_a + n_{b1}^2*d_{b1} + n_{b2}^2*d_{b2}}{d_a+d_{b1}+d_{b2}} \qquad (2.45)$$

$$d = d_a + d_{b1} + d_{b2}$$

where: n_{aw} is a weighted refractive index of the central region,

n_a, n_{b1}, n_{b2} are refractive indexes of the active and barrier layers,

d is an averaged active layer thickness,

d_a, d_{b1}, d_{b2} are thicknesses of the active and barrier layers.

Examples are presented in table 2.5.

Table 2.5. Weighted and effective refractive indexes of AlGaAs systems at 297K.

λ	Active material	Stripe width	Side layer	n_{aw} or n_{eff1}
0.8445505μm	76A GaAs sandwiched between 2*1050A $Al_{.25}Ga_{.75}As$	slab	-	n_{aw}= 3.44385
0.8445505μm	GaAs-$Al_{.25}Ga_{.75}As$ system with n_a=3.44385	2μm	polyimide n_b=1.614	n_{eff1}= 3.437819
0.86743597μm	GaAs, n_a=3.600886	2μm	polyimide n_{b1}=1.614	n_{eff1}= 3.594468

A stripe structure, made out of the slab waveguide, may necessitate the replacement of the n_{aw} from the above equation with the effective refractive index n_{eff1} of the light confinement region with the refractive index n_{aw} and lateral cladding layers with the refractive index n_{c2}, if the structure possesses a higher refractive index step in the lateral direction (section 1.3). Examples are presented in table 2.5.

2.3.4. Optimum width of the optical waveguide layers and the quantum wells of the laser structure.

For the given values of wavelength, λ, guide thickness, d, guide index, n_{aw} and cladding layer index, n_c, the distribution of the optical intensity E^2 within the slab waveguide may be calculated (section 1.1). Comparing the normalised effective optical width S for different normalised thicknesses of the active layer D, the optimum width of the light confinement region d_{opt} may be found, to assure maximum confinement of the zero order mode. S_{min} corresponds to D= 1.7, where the optical distribution is about 40% wider than the thickness of the central layer [Thompson−1]. The designed materials are presented in figures 2.16 and 2.17. As mentioned in section 2.2.1, the value of d_{opt} is overestimated, particularly if the laser structure shows low loss. However, wider guides prevents excessive loss due to the spread of light to further layers. The normalized widths are defined as [Thompson−1]:

$$S = \frac{\int_{-\infty}^{\infty} E_x^2 dy}{E_{max}^2} * \sqrt{(\varepsilon_{aw}-\varepsilon_c)} * \beta_o \qquad (2.46)$$

$$D = d * \sqrt{(\varepsilon_{aw}-\varepsilon_c)} * \beta_o \qquad (2.47)$$

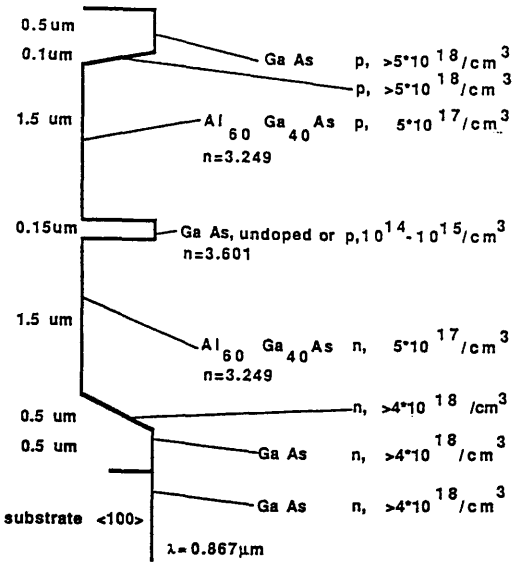

Fig.2.16. The optimised design of the double heterostructure material.

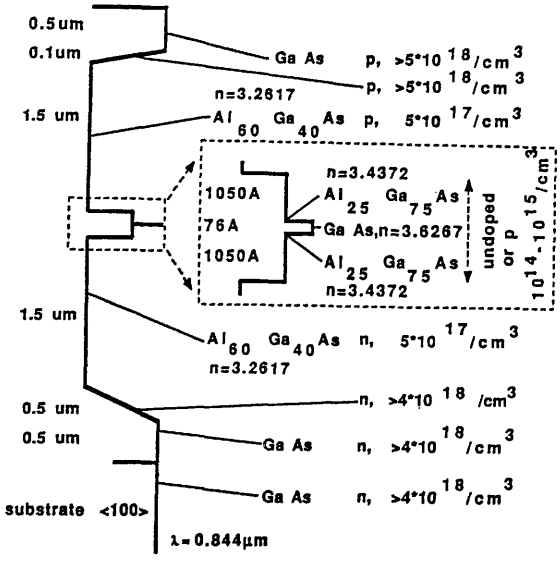

Fig.2.17. The optimised design of the localised gain region separate confinement quantum well laser material.

and the optimised thickness of the active layer is then:

$$d_{opt} = \frac{1.7*\lambda}{2*\pi*\sqrt{(n_{aw}^2-n_c^2)}} \qquad (2.48)$$

where: $\varepsilon = n^2$ is the dielectric constant of the layer and

$\beta_o = \frac{2*\pi}{\lambda_o}$ is the free space propagation constant.

Examples are presented in table 2.6.

Table 2.6. Optimised thickness of the active layer of AlGaAs systems at 297K.

Central layer	Cladding layers	λ	d_{opt}
0.152μm GaAs	$Al_{.6}Ga_{.4}As$	0.8674597μm	0.152μm
0.152μm GaAs, 2μm rib embedded in polyimide	$Al_{.6}Ga_{.4}As$	0.8674597μm	0.153μm
76A GaAs sandwiched between 2*996A $Al_{.25}Ga_{.75}As$	$Al_{.6}Ga_{.4}As$	0.8445505μm	2067A
76A GaAs sandwiched between 2*996A $Al_{.25}Ga_{.75}As$, 2μm rib embedded in polyimide	$Al_{.6}Ga_{.4}As$	0.8445505μm	2104A
0.2207μm $Al_{.25}Ga_{.75}As$ (passive guide)	$Al_{.6}Ga_{.4}As$	0.8445505μm	2207A

The maximised refractive index step within the waveguide and the optimal thickness of the active layer therefore reduces the threshold current of the laser device (section 2.2).

The dominance of different modes within the laser structure, as well as their threshold current, is determined not only by the internal loss, including the loss due to the curvature of the ring structures but, in addition, by the loss at the output coupler. The higher order optical modes dominate waveguiding for the thicker active layers [Thompson–1]. An increased active–cladding layer energy step results in a smaller thickness value, above which the higher order modes dominate. For practical thicknesses of the active layer a Fabry–Perot resonator favours the TE mode

[Thompson–1], while experimental ring resonator lasers, described here, supported both the TE and TM modes.

The quantum well width could be further optimised by finding the structure with maximum efficiency, providing the maximum ratio of light intensity within the well to the total light intensity per well thickness:

$$\frac{\delta}{\delta d}\left[\frac{\int_{-d/2}^{d/2} E_x^2 dy}{d * \int_{-\infty}^{\infty} E_x^2 dy}\right] = 0 \qquad (2.49)$$

This problem was not tackled but the well width dependence of the threshold current was presented in section 2.2.

2.3.5. Directionally coupling the light out of the active region.

Light created and confined to the lasing region may be coupled out to a closely situated passive waveguide with similar propagation constant. A waveguide of 0.22μm thick $Al_{.25}Ga_{.75}As$ (Table 2.6) separated from the lasing region (7.6nm thick GaAs sandwiched between two 0.105μm thick $Al_{.25}Ga_{.75}As$ cladding layers) by 0.4μm wide $Al_{.6}Ga_{.4}As$ (fig.2.18) was calculated to couple light out after a distance of 31μm (section 1.4). The structure of fig.2.18 provides also an improved carrier confinement.

The thickness of the cladding layers is also determined by the possibility of coupling the light out of the active layer (section 1.4) and should be larger than 1.5μm to prevent degradation of coupling within the long ring path structures.

2.3.6. Improved life–time laser.

The lifetime of the lasers may be improved by reducing stresses within the active layer. The influence of dislocations within the substrate on the active layer is reduced by growing a buffer layer. Crystalline defects can be limited by a good match of the lattice constant between various layers. The GaAs–$Al_{.6}Ga_{.4}As$ system is characterised by a 0.1% mismatch, which results in a degradation of the first few atomic layers of the subsequent material. This may be reduced using a $Al_{.6}Ga_{.4}As_{.97}P_{.03}$ system, but this is rarely done. The residual stresses induced by different thermal expansion of the subsequent layers may be eliminated with the proper choice of layer materials and thicknesses [Liu–39] for:

$$\frac{Y}{X} = 1 + \frac{d_s}{4*(d_{c1}+d_{c2})} \qquad (2.50)$$

For typical lasers $Y/X = 1+100/[4*(1.5+1.5)] = 9.3$,

where X,Y are content of Al in the active and cladding layers,

d_s, d_{c1}, d_{c2} are thicknesses of the substrate and cladding layers.

In practice, an active layer rarely incorporates Al, due to difficulties in the growth of thin layers with differing Al concentrations.

2.4. LASER MATERIAL EVALUATION.

The performance of the laser material can be evaluated by measuring the performance of Fabry–Perot two–dimensional broad area devices. Standard fabrication methods were used to produce ohmic contacts of width 50 to 100μm and length 100 to 500μm, and to cleave the devices (section 3). Much narrower stripe structures behave differently than the broad area devices. They may produce degraded light confinement in the third dimension (section 1.2) leading to excessive increase in loss, threshold current, operating temperature and the emitted wavelength (section 4).

The three heterostructures presented and designed in sections 2.1 and 2.3 were compared: a double heterostructure, a localized gain region separate confinement quantum well material, and a localized gain region separate confinement quantum well material with improved carrier confinement and with a coupled passive waveguide (figs.2.2, 2.16, 2.17, 2.18).

2.4.1. Experimental measurements.

The devices were mounted on a gold–foil electrode and probed to establish the top contact. Diode characteristics and luminescence at low currents up to 10mA were evaluated. The lasing threshold current was then estimated by testing the output optical power at increasing current, using a Photodyne 88XLC power meter. The devices required pulsed current operation to reduce the heat produced. The laser was driven with a pulse width 0.1 to 1μs at a repetition time 0.05 to 0.5ms. A faster repetition rate produced changes in the device characteristics (Appendix 2). The shape of the pulse was improved by matching the impedances of generator and termination of the coaxial cables (fig.2.19). The peak current was monitored on an oscilloscope. The spectra of the emitted light were measured through 40x and 20x

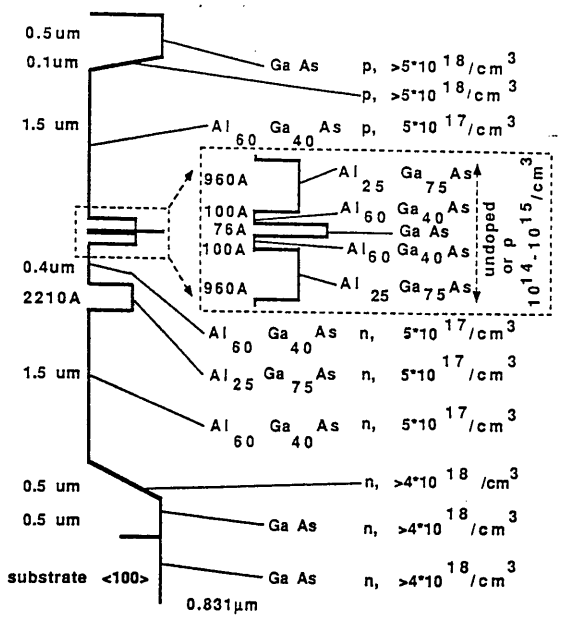

Fig.2.18. The optimised design of the localised gain region separate confinement quantum well laser material with improved carrier confinement and an additional coupled passive guide.

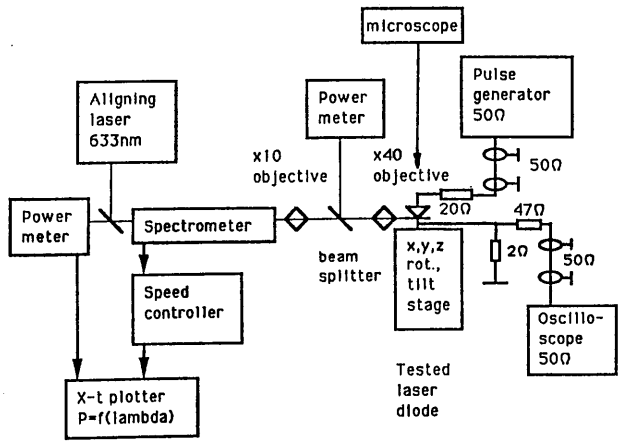

Fig.2.19. Spectral measurement system of the laser devices.

objectives for collimating and focusing the beam onto the input slit of a monochromator, respectively (fig.2.18). The output from the 5μm wide output slit of the monochromator was measured using a power meter. The monochromator was equipped with a stepper motor, while the power meter output was fed to the input of the X– t plotter, to plot the output spectra of the devices. Wavelength resolution was limited to 0.16nm, but by averaging the results of several measurements, better accuracy in estimates of spectral line spacing could be achieved. The spectra were measured both below and above the threshold current.

Although the devices lased within the invisible range of the spectrum (approximately 850nm), due to the exceptionally high intensities of the sources and their evanescent field, at higher currents they could be seen. A stripe structure pumped with a low current produces uniform luminescence along the device. Lasing action for higher currents was accompanied by a shift of the luminescence towards the mirrors of the device (usually, only one of them).

2.4.2. DH broad area laser performance.

Double heterostructures incorporated waveguides made of undoped GaAs layer, having different thickness between 0.1 and 0.2μm sandwiched between two, 1.5μm or thicker, p– and n– type AlGaAs cladding layers, doped up to $5*10^{17}/cm^2$, with differing Al content between 20 and 40%. For contact purposes, a n^+-GaAs substrate and the top p^+-GaAs layer were highly doped, to above $3*10^{18}/cm^3$.

The double heterostructure lasers fabricated from material with a higher Al concentration resulted in increased light confinement due to a larger index step within the guide and lased at a lower threshold current.

The DH lasers should lase at approximately 869nm at a room temperature of 20°C. The broad area devices of dimensions 270μm * 370μm, of the improved structure with a 40% Al content, lased at 1.7 amps under pulsed current operation, giving a threshold current density of $1.7kA/cm^3$ (fig.2.20). Above the threshold, the luminescence spectrum halfwidth was 20nm and multimode operation was observed with a peak at 882nm (fig.2.21). This corresponds to a junction operating temperature of 70°C, which confirmed the theoretical evaluation of the heat distribution within the laser devices (section 4.1).

At the threshold current, the DH lasers emit little luminescence between 0.04 to

0.2mW (fig.2.22), since the material lases within the thick region which is optically lossy at the emitted wavelength.

2.4.3. LGRSCQW broad area laser performance.

Three localized gain region lasers were compared. The first incorporated a 22.7nm single quantum well of GaAs sandwiched between two 0.1 μm thick, undoped $Al_{.25}Ga_{.75}As$ barriers, which were sandwiched in turn between two, p− and n− type $Al_{.6}Ga_{.4}As$ cladding layers, doped to $5*10^{17}/cm^3$. A second structure incorporated a thinner, 7.6nm single quantum well (fig.2.17), while the third structure was similar to the second, with additional 10nm barriers of $Al_{.6}Ga_{.4}As$, around the well, to improve carrier confinement. For contact purposes, the $n^+ - GaAs$ substrate and a top $p^+ - GaAs$ layer were highly doped to above $3*10^{18}/cm^3$.

The devices incorporating a 22.7nm QW material should lase at 860nm at a room temperature of 20°C. The broad area devices of 300*400 μm lased at 750mA under pulsed operation, giving a threshold current density of $700A/cm^3$ (fig.2.20). Multi− mode operation was observed with a peak at 858nm (fig.2.21), suggesting that the increase in temperature of the junction was small. At the threshold current, the device gives luminescence of 0.04 to 0.2mW, comparable to that of double heterostructure devices (fig.2.22).

The calculated wavelength of the broad area devices incorporating a 7.6nm single quantum well operating at room temperature is 840nm (section 2.3, Appendix 2), while that of the material incorporating additional barriers is 831nm. Both materials lased at 841nm (fig.2.21), with a second small peak at approximately 700nm. This indicates a negligible increase of junction temperature over the surrounding media. The thin barriers of the third structures did not seem to influence the lasing wavelength; on the other hand, the third structure may have been identical with the second one, since the structure described in the section 2.4.4, which also incorporated the additional barriers, lased at a reduced wavelength of 832nm.

A typical device of dimensions 50*400 μm lased at $420A/cm^2$ threshold current density (fig.2.20), which increased rapidly with reduced length of the device (Table 2.7), and devices shorter than 110 μm could not be made to lase (fig.2.23). A 100 μm wide laser had slightly lower value of threshold current density than the 50 μm wide lasers.

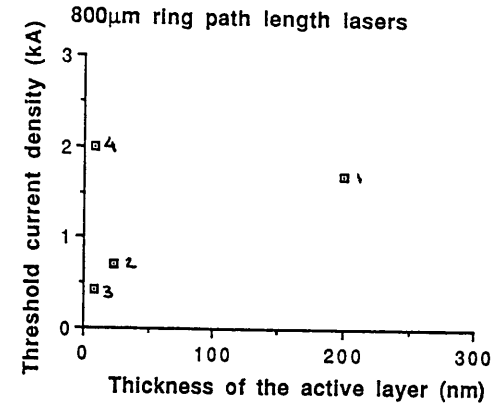

Fig.2.20. Threshold current densities of the 800μm closed ring path length lasers presented in sections: 2.4.2, 2.4.3, 2.4.4:
1. DH with a 0.2μm thick well,
2. LGRSCQW with a 22.7nm thick well,
3. LGRSCQW with a 7.6nm thick well,
4. LGRSCQW– CPW with a 7.6nm thick well and additional barrier layers.

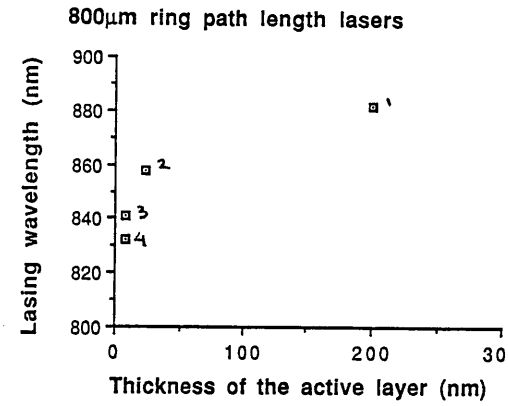

Fig.2.21. Lasing wavelengths of the 800μm closed ring path length lasers presented in sections: 2.4.2, 2.4.3, 2.4.4:
1. DH with a 0.2μm thick well,
2. LGRSCQW with a 22.7nm thick well,
3. LGRSCQW with a 7.6nm thick well,
4. LGRSCQW– CPW with a 7.6nm thick well and additional barrier layers.

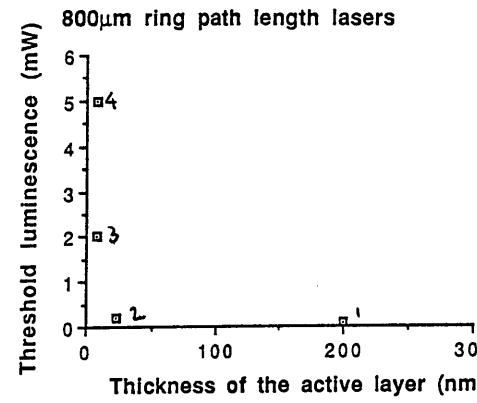

Fig.2.22. The luminescence power at the threshold of the 800μm closed ring path length lasers presented in sections: 2.4.2, 2.4.3, 2.4.4:
1. DH with a 0.2μm thick well,
2. LGRSCQW with a 22.7nm thick well,
3. LGRSCQW with a 7.6nm thick well,
4. LGRSCQW– CPW with a 7.6nm thick well and additional barrier layers.

Table.2.7. 7.6nm QW lasers (s – single mode, m– multimode operation, B– structure incorporating barrier)

guide width	length	output guide	I_{th}	J_{th}	λ	Comments
(μm)	(μm)	(μm*μm)	(mA)	(kA/cm^2)	(nm)	
100	800	-	220	0.27	844	s,
100	400	-	140	0.35	840	m, B,
50	420	-	90	0.4	840	m, B,
50	300	-	70	0.46	840	m, B, 1.6mW thr
50	250	50*50pas	60	0.48	840	m, B,
50	300	-	80	0.53	841	m, 0.7mW thr,
100	240	-	150	0.62	841	m, NP
50	200	-	80	0.66	841	m, NP
50	250	-	90	0.72	840	m, B, 1mW thr,
50	250	-	90	0.72	840	m, 2.6 mW thr,
50	200	-	150	1.5	840	m, B, 4mW thr,
50	110	-	370	6.7	840	m, B, 8mW thr,
50	100	250*50pas,	did not lase, (B),			
50	100	-	did not lase,			

At the threshold current, the devices give strong luminescence between 1.6 and 8mW, increasing with reduced device lengths (fig.2.22). The high luminescence is due to a very narrow, absorbing carrier confinement region and consequent guiding of the light produced within the low loss guide.

Single longitudinal mode operation was observed just above the threshold current and this converted into multimode operation at higher currents. The lasing wavelength of broad area devices corresponds to the first state electron– to– heavy hole transition, unless they were very short, and as a result, lossy [Mittlestein– 29] (section 2.2.4). Mode and transition behaviour of the broad area devices were different from that of the narrower structures (section 4.3.4.4).

Lasers with contact partially removed from above the waveguide can be made to lase unless the contact is very short (Table 2.7). A short pumping region results in a spread of the light away from the gain region and characteristics which are similar to those of the device with the length of the contact itself.

2.4.4. LGRSCQW– CPW broad area laser performance.

The structure of the localized gain region separate confinement quantum well material with a coupled passive waveguide, was similar to the LGRSCQW. It consisted of a 7.6nm quantum well, with the additional 10nm barriers of $Al_{.6}Ga_{.4}As$, placed within the light confinement region (section 2.4.3.) and an additional waveguide of 0.21μm thick GaAs incorporated beneath the lasing guide and separated by a 0.4μm thick, undoped $Al_{.25}Ga_{.75}As$ layer (figs.2.2, 2.18).

A localized gain region laser with a coupled passive guide should lase at the wavelength of 831nm. The broad area devices operated at 832nm (fig.2.21) in single longitudinal mode operation within a large range of currents (fig.2.24). The threshold current was 3 to 5 times larger than that of similar length devices made in a structure without the passive guide.

The threshold current density of similar length devices varies considerably. The threshold current of devices 50*300μm falls between 230 and 370 mA, corresponding to current densities of 1500 and 2500 A/cm^2 (fig.2.20). A 100μm wide guide produces slightly lower values of threshold current density than a 50μm wide guide , and a 100*300μm device lased at 440mA, corresponding to 1466A/cm^2. The threshold current was comparable to that of the normal structure, without the passive guide, with a much shorter length of 200μm. The spread of the light from the active lossy region resulted in a very high spontaneous emission level below the threshold current, approximately 5mW for a device of 50*300μm (fig.2.22). This value was again similar to that of the normal structure, without the passive guide, and with a much shorter, 200μm length.

Single longitudinal mode operation and increased threshold current of the practical devices confirmed our assumptions that the additional passive waveguide coupled to the lasing area makes lasing conditions more critical. It requires overlapping oscillations within both cavities of the laser and the waveguide. The spread of the light away from the active layer decreases the efficiency of the stimulating emission and results in an increased threshold current density. The coupling length between

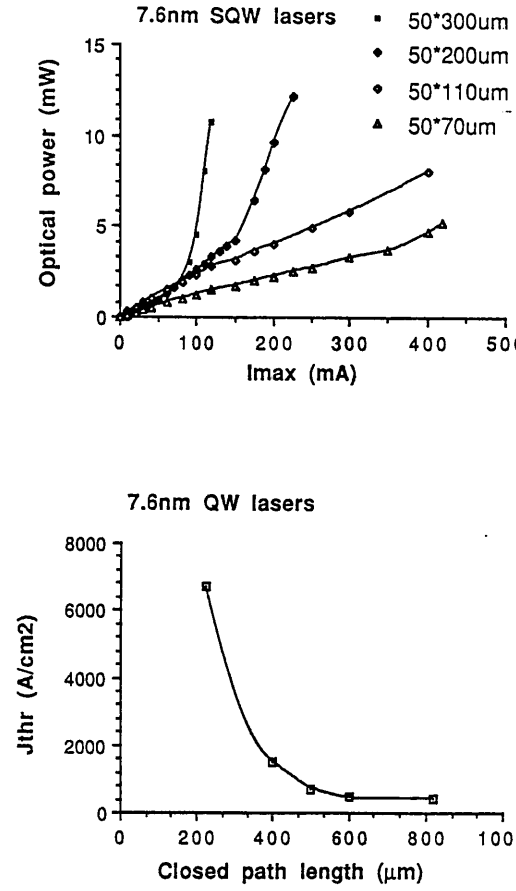

Fig.2.23. Dependence of the threshold current density on the closed path length of the 50μm wide broad area laser made of material with a narrow, 7.6nm well.

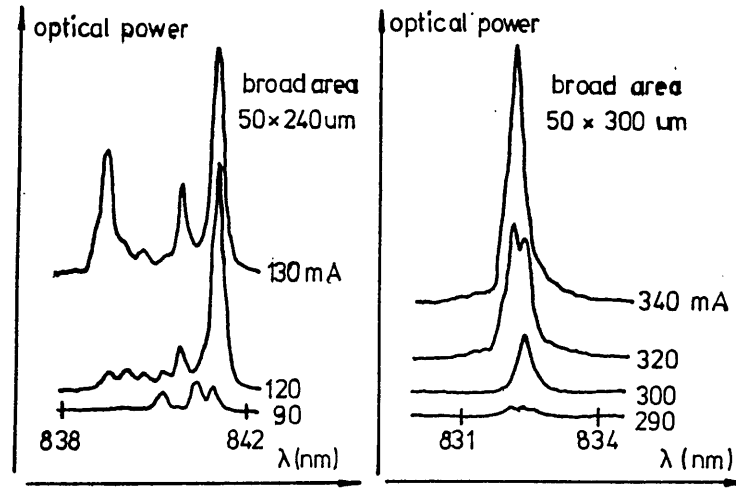

Fig.2.24. Spectra of the localised gain region quantum well laser 1.) without and 2.) with coupled passive waveguide.

the lasing region and the passive waveguide was calculated to be 31 μm (section 1.4). This would change subject to quality and uniformity of the material. Consequently, similar sizes of the device result in a large variation in that amount of the optical power "lost" from the lasing region and the threshold current density.

2.5. SUMMARY.

The evaluation of ring lasers required analysis of the materials used in their production. Three structures were developed: a double heterostructure, a localised gain region separate confinement quantum well structure and a quantum well structure with additional coupled passive waveguide. The DH laser possesses a linear dependence of the threshold current density on the loss, while the QW lasers exhibit a stronger, exponential dependence. The increased threshold current for lossy devices due to their reduced length was presented experimentally. The influence of loss due to other factors is presented in section 4.3.4.

Detailed calculation of the waveguiding laser structures included the energy band–gaps of the materials used, emission wavelength, refractive indicies, weighted indicies or effective indicies of the materials used and the optimum waveguide parameters.

All the structures were produced and evaluated as broad area devices. All the structures lased at relatively low threshold currents, for the typical closed path device length of 800 μm. The LGRSCQW lasers incorporating a 7.6nm thick QW operated at a lower threshold current density (420A/cm^3), than the ones incorporating a wider, 22.7nm thick well (700A/cm^3), and lower still than DH lasers (1.7kA/cm^3) (fig.2.20), confirming the theoretical predictions [Thompson–1]. The narrow QW laser threshold current density increased rapidly for shorter devices (6730A/cm^3 for the closed ring path length of 220 μm) and could not be made to lase for closed path lengths shorter than 220 μm. The spread of the light to an additional waveguiding region within the LGRSCQW–CPW structure resulted in a relatively high threshold current density of approximately 1.3 to 2.2kA/cm^3 (fig.2.20). This may have been influenced by too strong a carrier confinement due to the incorporated additional barriers. The restricted oscillation conditions and material quality dependence of the coupling between both guides resulted in different threshold current densities for similar device sizes.

QW material with a thicker, 22.7nm well, posesses a small luminescence power

below the threshold current, comparable with that observed in DH, of between 0.04 to 0.2mW (fig.2.22). Narrow, 7.6nm well material is less absorbing for the lasing wavelength and increases this value up to 2mW for typical length devices, and up to 8mW for very short lasers. The structure incorporating an additional passive guide distributes the light between two guides, increasing the luminescence up to 5mW for reasonable length devices.

The emitted wavelength of the DH is much greater than the calculated value, due to the increased temperature of the laser junction. The calculated room temperature wavelength is 869nm, while the broad area device generally lases at 882nm, corresponding to 70°C (fig.2.21). The quantum well broad area devices lase at similar wavelengths to those calculated for room temperature conditions. The values are 860nm for the 22.7nm QW material with $Al_{.25}Ga_{.75}As$ barriers, and 840nm for 7.6nm QW material (fig.2.21). (Lossy stripe devices, made of narrow QW lase at a different wavelength due to second quantised state operation, as described in sections 2.2.4, 4.3.4.3.). A 7.6nm QW laser with the additional passive guide lases at a wavelength of 832nm due to the additional 10nm thick barriers of $Al_{.6}Ga_{.4}As$ around the well.

Broad area devices made of DH material lase in multiple longitudinal mode operation. The devices made of QW structures lase in single mode operation just above the threshold current, and in multiple mode at higher currents. A stripe configuration is necessary for both DH and QW structures to produce single mode operation within a larger range of currents. The broad area devices made out of material incorporating an additional passive guide, restrict oscillation conditions to those oscillations occuring at a common resonance of the possible oscillations within both lasing and passive guides and produces single mode operation within a large range of currents.

2.6. REFERENCES.

[1] Thompson G.H.B.: Physics of semiconductor laser devices, J.Wiley & Sons (1980).

[2] Panish M.B.: Heterostructure injection lasers, Proc.IEEE, Vol.64, 10, pp.1512–1540 (1976).

[3] Sakaki H., Yoshino J., Sekiguchi Y., Sakai K.: Superlattice optical cavity multiple quantum well (SOC–MQW) lasers grown by molecular beam epitaxy, Electr.Lett, Vol.20, 8, pp.320–322 (1984).

[4] Fujii T., Hiyamizu S., Yamakoshi S., Ishikawa T.: MBE growth of extremely

high quality GaAs–AlGaAs GRIN–SCH lasers wioth a superlattice buffer layer, J.Vac.Sci.Techn., B3(2), pp.776–778 (1985).

[5] Hersee S.D., Baldy M., Assenat P., De Cremoux B., Duchemin J.P.: Very low threshold GRIN–SCH GaAs/GaAlAs laser structure grown by OM–VPE, Electr.Lett., Vol.18, 20 pp.870–871 (1982).

[6] Casey H.C., Sell D.D., Panish M.B.: Refractive index of AlGaAs between 1.2 and 1.8eV, Appl.Phys.Lett., Vol.24, 2, pp.63–65 (1974).

[7] Casey H.C., Panish J.M.B.: Composition dependence of the GaAlAs direct and indirect energy gaps, J.Appl.Phys., 40 pp.4910 (1969).

[8] Casey H.C, Stern F.: Concentration dependent absorption and spontaneous emission in heavily doped GaAs, J.Appl.Phys., 47, pp.631–643 (1976).

[9] Sell D.D., Casey H.C., Wecht K.: Concentration dependence of the refractive index for n– and p–type GaAs between 1.2 and 1.8eV, j.Appl.Phys., 45, pp.2650 (1974).

[10] Thompson G.H.B, Kirkby P.A.: Low threshold current density in 5–layer–heterostructure (GaAl)As/GaAs localised gain region injection lasers, Electr.Lett., 24 pp.481 (1974).

[11] Tsang W.T.: A graded index waveguide separate confinement laser with very low threshold current and narrow Gaussian beam, Appl.Phys.Lett. 39(2), pp.134–137 (1981).

[12] Holonyak N.J.R., Kolbas R.M., Dupuis R.D., Dapkus P.D.: Quantum well heterostructure lasers, IEEE J.QE–16, 2, pp.170–185 (1980).

[13] Zielinski E., Schweizer H., Hausser S., Stuber R., Pilkuhn H., Weimann G: Systematics of laser operation in GaAs/AlGaAs MQW heterostructures, IEEE JQE–23, 6, pp.969–976 (1987).

[14] Tsang W.T.: The cleaved–couple–cavity (c^3) laser, Semiconductor and semimetals, Vol.22, pt.B, 5, pp.257–373 (1985).

[15] Chinn S.R., Zory P.S., Reisinger A.R.: A model for GRIN–SCH–SQW diode lasers, IEEE JQE–24, 11, pp.2191–2214 (1988).

[16] Tsang W.T.: Extremely low threshold (AlGa)As graded index waveguide separate confinement heterostructure lasers grown by molecular beam epitaxy, Appl.Phys.lett., 40 (3), pp.217–219 (1982).

[17] Garrett B.: Design of quantum well lasers, STC Technol. ltd., Paington, Lecture at Glasgow University (1988).

[18] Nagle J., Weisbuch C.: The physics of the quantum well laser, Thompson CSF, Orsay, France, pp.251–268 (1987).

[19] Wilcox J.Z., Peterson G.L., Yang O.J.J., Jansen M., Schechter D.: Gain and threshold current dependence for multiple quantum well lasers, J.Appl.Phys., 64 (11), pp.6564–6567 (1988).

[20] Mc Ilroy P.W.A., Kurobe A., Uematsu Y.: Analysis and application of

theoretical gain curve to the design of multi−quantum well lasers, IEEE J.QE−21, 12, pp.1958−1963 (1985).

[21] Arakawa Y., Yariv A.: Theory of gain, modulation response and spectral linewidth in AlGaAs quantum well laser, IEEE JQE−21, 10, pp.1666−1674 (1985).

[22] Arakawa Y., Yariv A.: Quantum well lasers − gain, spectra, dynamics, IEEE JQE−22, 9, pp.1887−1899 (1986).

[23] Kasemset D., Hong C.S., Patel N.B., Dapkus P.D.: Graded barrier single quantum well lasers − theory and experiments, IEEE JQE−19, 6, pp.1025−1029 (1983).

[24] Blood P., Fletcher E.D., Woodbridge K.: Dependence of threshold current on the number of wells in AlGaAs−GaAs quantum well lasers, Appl.Phys.Lett., 47(3), pp.193−195 (1985).

[25] Saint−Crico B., Lozes−Dupuy F., Vassilieff G.: Well width dependence of gain and threshold current in GaAlAs single quantum well lasers, IEEE JQE−22, 5, pp.625−630 (1986).

[26] Sagimura A.: Threshold currents for AlGaAs quantum well lasers, IEEE JQE−20, 4, pp.336−343 (1984).

[27] Kurobe A., Furuyama H., Naritsuka S., Sugiyama N., Kokubun Y., Nakamura M.: Effects of well number, cavity length, and facet reflectivity on the reduction of threshold current of GaAs/ AlGaAs multiquantum well lasers, IEEE JQE−24, 4, pp.635−640 (1988).

[28] Reisinger A.R., Zory P.S., Waters R.G.: Cavity length dependence of the threshold behaviour in thin quantum well semiconductor lasers, IEEE J.QE−23, 6, 993−999 (1987).

[29] Mittelstein M., Arakawa Y., Larrson A., Yariv A.: Second quantised state lasing of a current pumped single quantum well laser, Appl.Phys.lett., 49(25), 22, pp.1689−1691 (1986).

[30] Yuasa T., Yamada T., Asakara K., Ishii M.: Performance of dry−etched short cavity GaAs/ AlGaAs multiquantum well lasers, J.Appl.Phys., 63(5), pp.1321−1327 (1988).

[31] Blakemore J.S.: Semiconducting and other major properties of gallium arsenide, J.Appl.Phys., 53(10), pp.R123−R181 (1982).

[32] Casey H.C., Panish M.B.: Heterostructure lasers, Academic, NY, Parts A and B (1978).

[33] Adachi S.: GaAs, AlGaAs and $Al_xGa_{1-x}As$: Material parameters for use in research and device applications, J.Appl.Phys., 58(3), pp.R1−R29 (1985).

[34] Kawai H., Kaneko K., Watanabe N.: Photoluminescence of AlGaAs/ GAAs quantum wells grown by metalorganic chemical vapour deposition, J.Appl.Phys., 56(2), pp.463−467 (1984).

[35] Bhumbra B.: private communication, Glasgow University, (1987).

[36] Evtuhov, Jariv A.: GaAs and GaAlAs devices for integrated optics, IEEE Trans. Microwave Theory and Techniques, MTT-23, 1, pp.44-57 (1975).

[37] Cross M., Adams M.J.: Effects of doping and free carriers on the refractive index of direct-gap semiconductors, Optoelectronics, 6, pp.199-216 (1974).

[38] MacBeans M.D.A.: Multiple quantum well structures as optical waveguides, PhD. Thesis, Glasgow University (1986).

[39] Liu H.D., Feng Z.C.: the stresses and photoelastic effects in stripe geometry GaAs-GaAlAs DH lasers with masked and selective thermal oxidation (MSTO) structure, IEEE JQE-19, 6, pp.1016-1020 (1983).

3. FABRICATION PROCESSES FOR RING LASER DEVICES.

3.0. INTRODUCTION.

Various GaAs– AlGaAs ring laser devices were designed and investigated. For each device, a fabrication procedure from a wafer to a packaged device was proposed. The processes necessary to achieve each production step were developed. The pretreatment of the sample strongly affects all the subsequent steps of processing and studies cross–examining a combination of various processes were performed.

Fabrication of a small semiconductor device requires a temperature and humidity controlled environment, with a limited number of dust particles since these could critically mask the processed areas. The general illumination of the environment should not affect the materials used (e.g. resists).

All the semiconductor processes must be preceeded by surface preparation revealing its unspoiled surface and removing its damage and stress (section 3.1).

The required pattern is created in a light– or electron–beam sensitive resist spun over the wafer (section 3.2), which is then transferred onto the pattern of semiconductor, metal or insulator to form the final device. This transfer is achieved by either selective etching or deposition of thin layers followed by a "lift off" method. The optimised lithography developed resulted in smooth high quality ring laser patterns with widths between 0.4 and 10μm.

Various methods of contact and insulator layer deposition and their annealing were investigated (section 3.3). Spinning of liquids provided layers that covered a high aspect ratio pattern smoothing its inlay, and became thinner on the top of the pattern. Evaporation along with a "lift off" method, formed layers with sharp discontinuities. Contact between semiconductor and certain metal compositions incorporating dopants produced ohmic properties on annealing. The investigations resulted in development of ohmic contacts, capable of high temperature operation at 350^{o}C, as well as a composition providing ohmic properties to both n– and p–type GaAs. The investigations were supported with a controlled annealer, developed to anneal the contacts in the optimal way.

Selective etching, either wet, chemical (section 3.4) or dry (section 3.5), ranging

from chemical to physical processes, were investigated. The chemical processing causes less damage to the processed surface and is highly selective to various materials, while physical sputtering may produce highly anisotropic laser structures with vertical walls. Reactive ion etching may combine the advantages of both methods. $SiCl_4$ gas was used to etch high aspect ratio ring laser structures, of width $0.5\mu m$ and height $7\mu m$. Low damage oxygen plasma etching was used to controllably etch the insulating polyimide around the ring laser pattern.

Cleavage of the wafer was used to separate high definition, high aspect ratio ring laser chips (section 3.6).

Small and fragile laser device packaging assured electrical connections, improving their mechanical strength and heat dissipation (section 3.7).

3.1. PREPARATION OF THE SEMICONDUCTOR SURFACE.

The nature of chemical pretreatment has a strong influence on surface properties and semiconductor–metal contact characteristics [1,2]. Any nonuniformity of the oxide or any contamination of the surface form a micromask preventing the uniformity of the subsequent processes and degrading the properties of final small pattern devices.

3.1.1. Oxide formation and removal.

A gallium arsenide substrate exposed to air or reagants is covered with a nonabsorbing film of oxides and other compounds [2,3,4] with a refractive index between 1.8 [5] and 3.5 [6]. The thickness of the film is influenced by the treatment of the semiconductor with various reagants.

The oxidation process on GaAs depends on diffusion of an oxidiser through an already existing oxide to the surface of the GaAs. Subsequent breaking of the Ga–As bonds and reactions produce new oxide molecules [7]. The diffusion and reaction are strongly increased with temperature and enhanced by impurities within the semiconductor (fig.3.1) or oxidiser.

The thickness of an oxide covering a freshly grown GaAs wafer is of the order of 1nm [2,5]), and increases up to 3nm after five days. Above a critical value of about

400°C [7,8] the growth rate rapidly increases. At 500°C, a 20hr. treatment in air produces a 1.16μm thick uniform isotropic oxide layer (figs.3.1,3.2) swelling outwards from the semiconductor with a calculated percentage volume increase of 34%. The oxidation through the pattern can be used to define some laser structures (section 3.3.1). Oxidation in dry oxygen (fig.3.3) and at temperatures above 530°C, results in a poor quality oxide [7,8].

The duration of GaAs oxidation with chemicals is critical due to their selectivity. Short treatment (5min [5,6]) preferentially dissolves certain oxides while longer, results in preferential reactions with Ga and As atoms increasing the oxide thickness [8,9,6,10]. A combination of reagants is necessary to achieve proper gallium arsenide oxide growth or reduction. The growth process is based on a water solution of hydrogen peroxide (H_2O_2:H_2O − 1:100 (+ wetting agent)). Reduction relies on water solutions of hydrochloric acid (HCl:H_2O − 1:1 or weaker) [2,5,9] or ammonia water (NH_4OH:H_2O − 1:2 or weaker) [2,11]. The processes are ended with water, solvent and water soaking, to remove traces of chemicals and dissolve the arsenic oxides [5,6,10].

3.1.2. Surface cleaning procedure.

Cleaning procedures provide surface uniformity to all the processes and should not destroy a ready made pattern.

Organic contamination is removed with ultrasonic agitation in solvents: methanol (removes water vapours), trichloroethylene (removes organic contamination; if boiled, removes wax), methanol (removes trichloroethylene remains) and acetone (removes traces of organic contamination). Traces of the solvents are washed away with deionised water. [It should be noted that solvents damage resists]. Subsequent oxide reduction reveals an unspoiled GaAs interface (fig.3.4) (section 3.1.1). [It should be noted that most acids damage metals and AlGaAs].

Subsequent polish− etching of the GaAs reduces all the stresses and damage to surface. The NH_4OH:H_2O_2:H_2O − 3:1:150 etch is advised for wafer cleaning and the ($KClO_3$:H_2O− 1g:100ml):HCl − 1:50 etch for pattern undercut cleaning (section 3.4.1) and their traces are removed with deionised water. Patterns smaller than 0.2μm require a wetting agent e.g. FC− 93 or New Decon (100ppm) to assure process uniformity. [It should be noted that wetting agents are soluble in IPA and

a.)

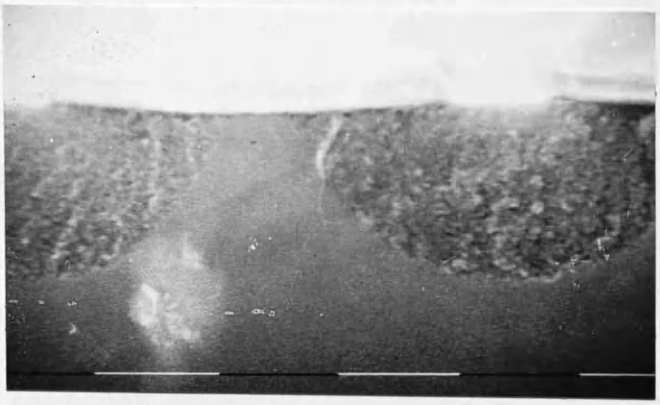

b.)

Fig.3.1. Thermal oxidation in air through the Cr+ Au mask of a.) GaAs and b.) GaAs substrate ($3*10^{18}/cm^3$) covered with a $0.5\mu m$ thick highly doped layer ($>10^{20}/cm^3$).

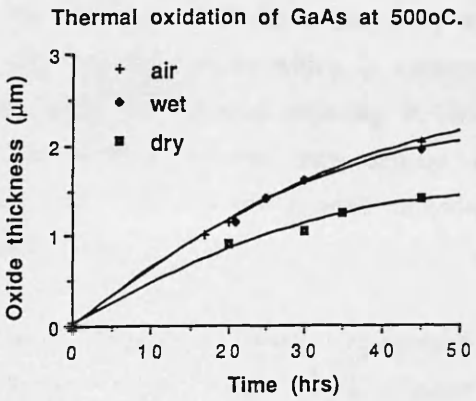

Fig.3.2. Thermal oxidation speed of GaAs, Zn doped to $3*10^{18}/cm^3$: in air, wet and dry oxygen at a temperature of 500^oC.

Fig.3.3. Thermal oxidation in dry oxygen of the GaAs wafer.

not in water].

The oxide left after the etching process is subsequently removed (section 3.1.1) leaving a uniform, unspoiled GaAs surface, and the sample is blow–dried with nitrogen.

The additional process of argon RF plasma sputtering improves the adhesion and properties of the evaporated layers (section 3.5.3).

3.2. LITHOGRAPHIC PROCESSES.

Throughout laser device manufacture, it is necessary to define the fine areas to be processed by means of lithographic methods [7]. The transfer of the pattern on to the semiconductor surface is usually accomplished in two stages. Firstly, a substrate is covered with a radiation–sensitive resist and pattern windows are opened in the resist. This is followed by a range of processes of the semiconductor surface through the opened windows. Lithography must proceed in a dust–free humidity controlled environment whose general illumination does not affect the resist.

There are two principal methods of pattern creation [7]. The "etching" method uses a resist pattern deposited on the top of the material, which is subsequently etched through the mask. The "lift off" method uses patterned resist which is subsequently covered with a thin film. The resist, along with the material covering it, is then removed, leaving the negative pattern. The etching process may damage some materials and requires tougher resist masks. The "lift off" in acetone provides an easy way to produce patterns and is discussed further.

Two main positive lithographic methods were investigated: photo–lithography and electron–beam lithography, both of which use resists which, when exposed are modified, so that they can be easily removed from the sample, using a developer [7,6]. The methods require a number of tests to achieve the required shape of the pattern, the resist profile, and consequently, a properly defined final ring laser device.

3.2.1. Optical lithography.

Photolithography uses an ultraviolet sensitive resist exposed through an opaque patterned glass mask. The layout of the mask was computer–generated, plotted in a large scale of 400 times the final size on a stable transparent film (fig.3.5) and photo–reduced to the required size. The reduction step smoothes the plotter increments down to 0.1 μm, losing definition at the Y–junctions of the pattern (fig.3.6) and limits minimum pattern widths to about 2μm .

Four different photo–resists produced by Shipley: AZ1350J, AZ1350, AZ4330 and AZ4110 [12], were tested. They were spun all over the samples at 4000rpm for 40sec and baked for 30min at 90°C or 30 sec at 115°C, producing respectively: 1.8μm, 0.8μm, 3.3μm and 1.1μm thick layers. Thinner resists improve resolution of the image, while thicker resists form a better cover of existing patterns. The resists were exposed to a U.V. light through an aligned mask. The influence of a 30min chlorobenzene soaking was investigated and these samples had to be baked for a shorter time of 15min at a temperature of 90 or 65°C [13,14]. The resists were developed in a water solution of AZ100 (or AZ400) developer, 1:1 for the two thicker and 4:1 for the two thinner resists [12].

The profile of the AZ4000 type resist was steeper than that of the AZ1000 type (figs.3.7,3.8) and this was further improved with a higher temperature, short–time baking (fig.8). The chlorobenzene treatment modified the top layer, reducing its solubility [13,14] and consequently resulted in an undercut profile for the AZ1000 resist series (fig.3.9), while it had little effect on the AZ4000 series (fig.3.10). A 20nm undercut beneath the resist may be produced using a room temperature ($KClO_3$:H_2O–1g:100ml):HCl–1:50 etch for 5sec. Subsequent evaporation of thin layers and "lift off" resulted in the desired pattern on the sample. The "lift off" was improved with a steeper resist pattern and an undercut. A larger undercut however, allowed for coverage of the space beneath the resist undercut, degrading the quality of the pattern edges (fig.3.9).

3.2.2. Electron–beam lithography.

Electron–beam lithography uses a direct exposure of the resist by a computer controlled focused electron–beam to produce fine patterns (down to 16nm wide on a thin substrate [15]). Back–scattering from the substrate results in the exposure

Fig.3.4. Influence of the deoxidation procedure on the subsequent $SiCl_4$ RIE.

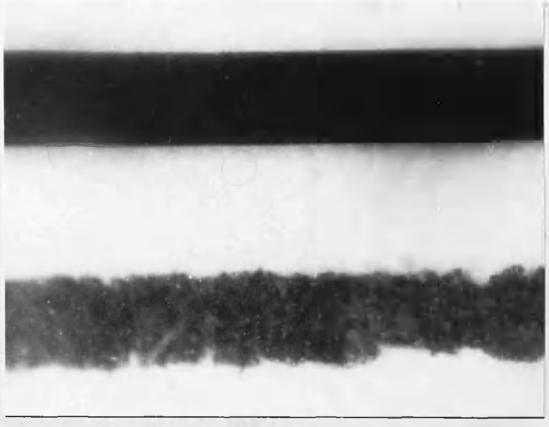

Fig.3.5. Pattern drawn on the transparent film and paper.

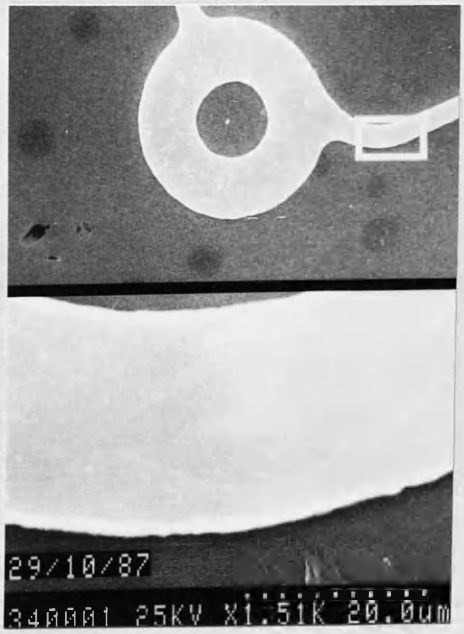

Fig.3.6. Optically defined mask incorporating Y-junction pattern of the ring laser device.

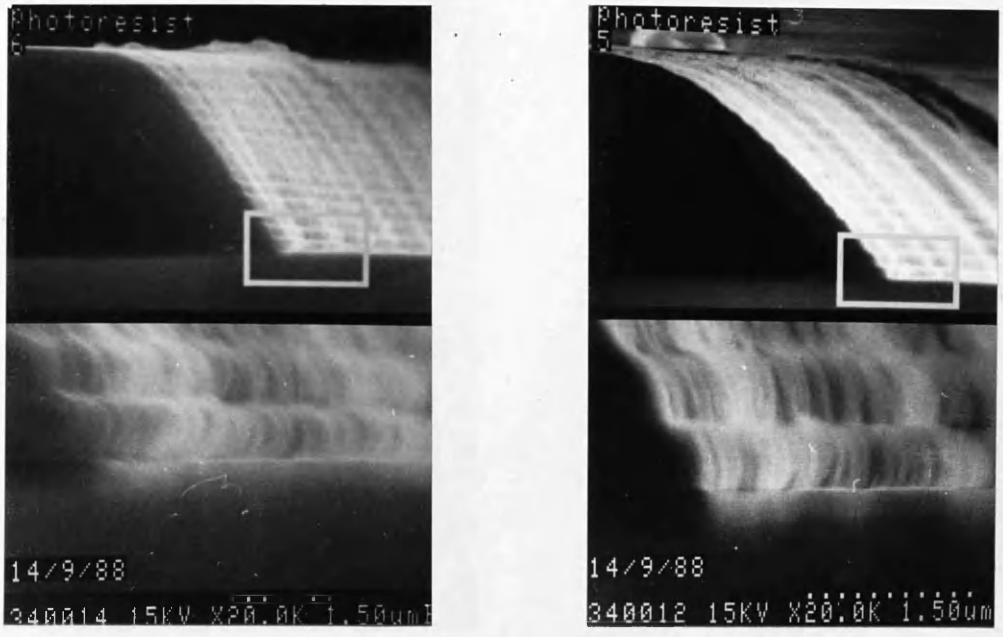

Fig.3.7. Profile of AZ1350J resist baked at 90°C for 15min, exposed to U.V. light for 11sec. and developed in AZ100:H_2O−1:1 for 1min. , or overdeveloped for 1min.30sec. (marker corresponds to the top part of each photograph).

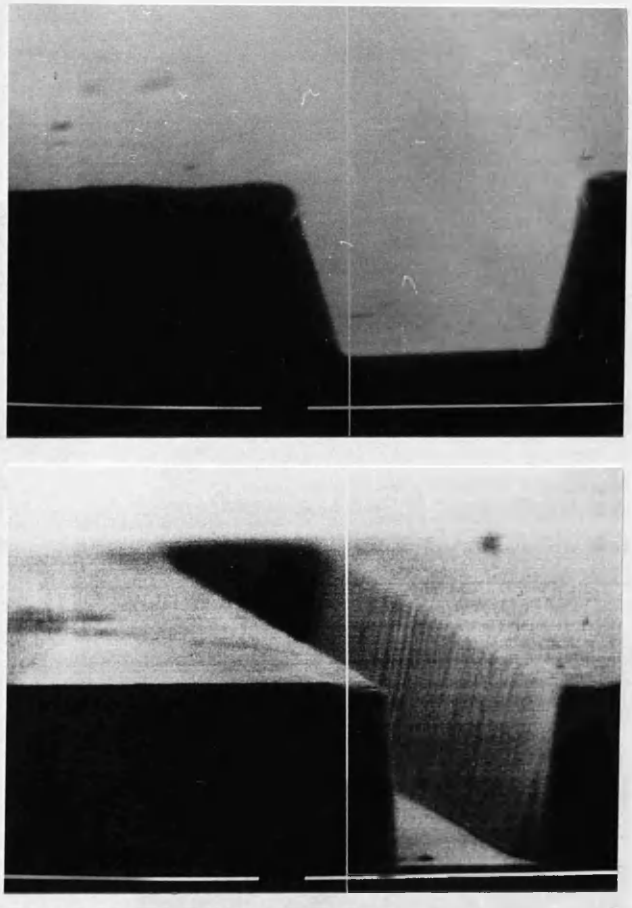

Fig.3.8. Profile of AZ4330 resist baked at 90°C for 15min, exposed to U.V. light for 11sec. and developed in AZ400:H_2O−1:4 for 2min. (top), or baked at 115°C for 30sec, exposed to U.V. light for 11sec. and developed for 1min.30sec. (bottom) (0.5μm marker)

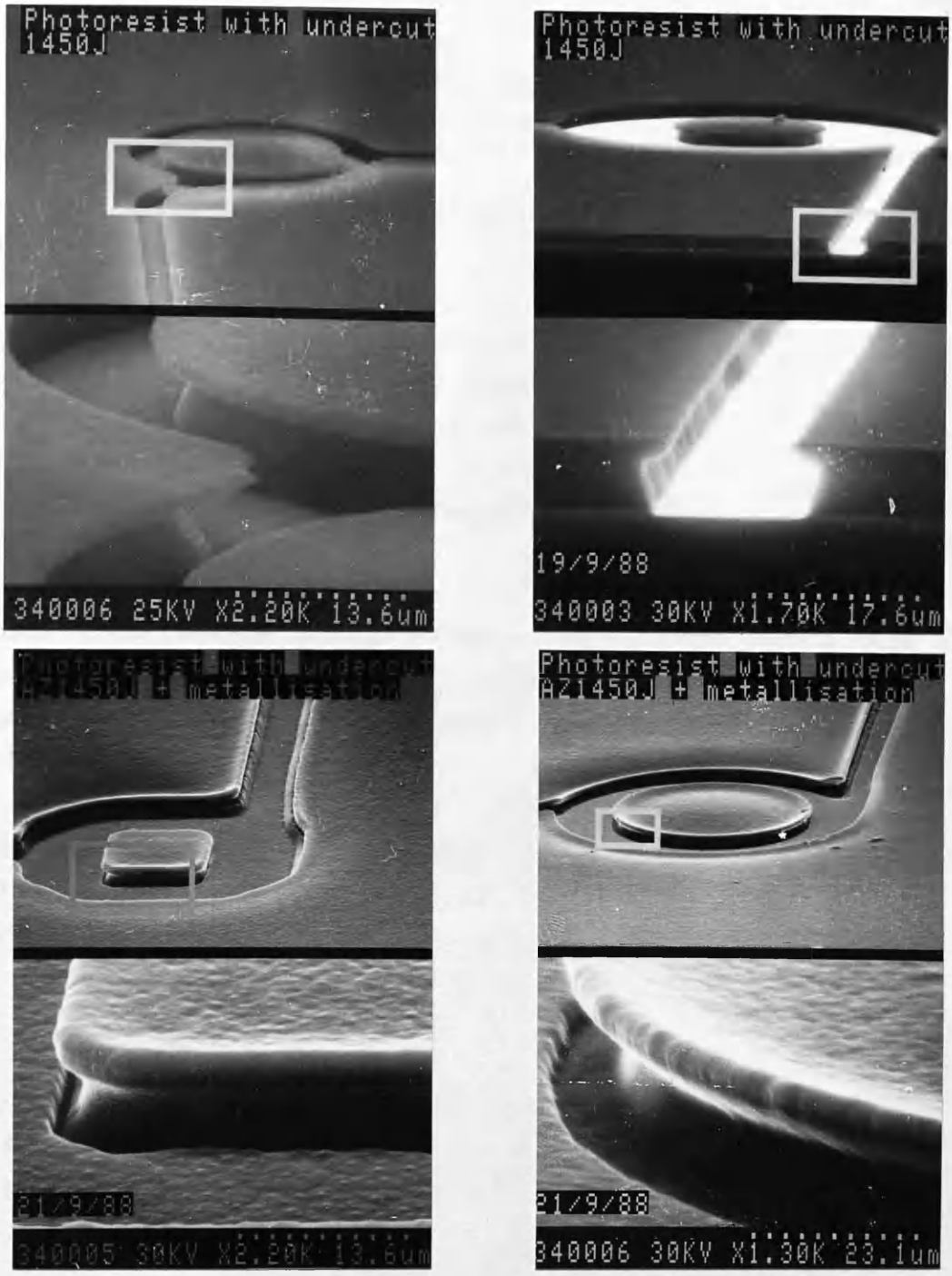

Fig.3.9. Profile of AZ1450J resist baked at 65°C for 15min, exposed to U.V. light for 11sec., soaked in chlorobenzene for 30min and developed in AZ100:H_2O−1:1 for 1min.10sec. Lower, resist covered with metal layer (marker corresponds to the top part of each photograph).

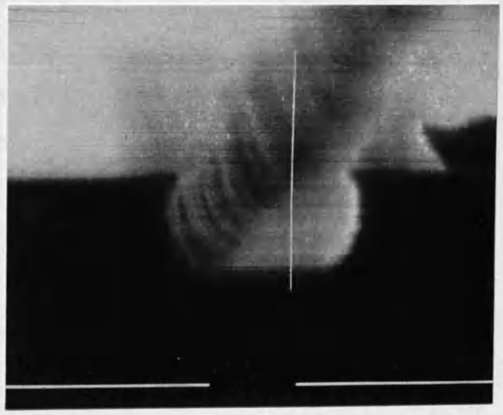

Fig.3.10. Profile of AZ4110 resist baked at 90°C for 15min, exposed to U.V. light for 11sec., soaked in chlorobenzene for 30min. and developed in AZ400:H_2O−1:4 for 1min.30sec. (0.5μm marker) (similar profile for high temperature baking)

proximity effect on the surrounding area [7,16] smoothing the fine pattern steps (fig.3.11).

The two-layer PMMA (poly (methyl methacrylate)) resist [17] consisted of a low molecular weight 8%BDH resist solution in xylene, followed by a high molecular weight 4% Elvacide resist solution. They were each spun at 5000rpm, and baked at 180°C for 1hr and 2.5hrs respectively, forming a 0.2 + 0.1 μm thick sandwich of layers. Subsequently, the patterns formed possessed a small undercut, useful for "lift off" purposes.

A modified Philips scanning electron-microscope type PSEM500 with a 50kV accelerating voltage and magnification of 320x was used to produce the pattern using a Design program [18]. The screen area consists of a grid of 4096 x 4096 pixels of size 95.3 x 72.4nm. The electron beam moves to the beginning of the pattern, and exposes it, pixel by pixel, from the top left corner, line by line, to the bottom right corner. A low exposure sacrificial rectangle below the proper pattern was used to avoid the blanking - exposure error (fig.3.12). The ring pattern consisted of 200 overlapping rectangles, to produce a smooth curved edge (fig.3.11). The exposure time of the rectangles forming the ring had to be shorter than that of the straight sections due to multiple exposure.

The exposed pattern was developed in: MIBK:IPA-1:2.5 at 23°C for 30sec., rinsed in IPA for 30sec., and blown dry with N_2. Subsequent metallisation and a "lift off" process produced the final ring laser pattern (figs.3.11).

3.3. DEPOSITION.

The fabrication of a ring laser device requires deposition of selectively patterned and stable thin films to create conductive paths between various parts of the device or their insulation [7,6]. They should create Schottky or ohmic contacts to the semiconductor and be free from pinholes and cracks, which would cause them to degrade with time and temperature. The properties of the deposited layers are affected by the prior surface preparation, deposition techniques and further processing [1]. The optimal combination of metals would form stable ohmic properties to semiconductor improving the life-time of the final ring laser devices.

The GaAs laser contact and interconnection technology is based on non-corroding,

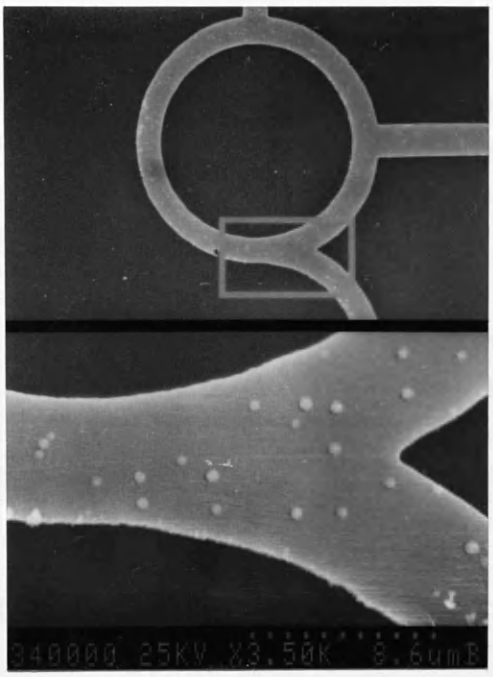

Fig.3.11. Ring laser metal pattern produced using e– beam lithography.

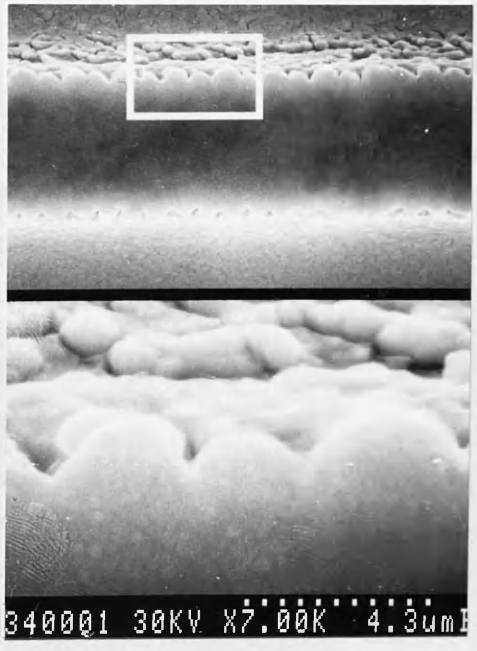

Fig.3.12. Blanking– exposure error using e– beam lithography, resulting in bad definition of vertical lines.

low resistivity gold, transition metals (e.g. Ti, Cr) improving its adhesion to insulators (e.g. SiO_2, Si_3N_4, polyimide), and barrier metals (e.g. Mo, W) preventing the interdiffusion of metal and semiconductor constituents. The thermally incompatible system of insulators and metals introduces stress resulting in degraded properties, unless the system is properly chosen and deposited [9].

This work presents the evaporation and the spinning deposition techniques used in producing laser devices. In evaporation, the thermal evaporator heats the required materials with a resistive heater driven with a high current, or with a beam of electrons collimated onto the material. Spinning is a much simpler technique, but is restricted to liquid substances.

3.3.1. Stresses due to deposition.

The interface of two materials with different thermal expansion coefficients (deposited at a different temperature from the one at which the system will operate) will exhibit stress [19]. This degrades the properties of the structure, in the form of dislocations, nucleation points or cracks, thereby reducing its lifetime. The variation in the thickness of the layers (in the extreme discontinuity of the films) also results in stress [19,20,21,22]. This is increased with the thickness of the layer [22,23]. The stress is distributed within the materials of total thickness d and results in a bending of the structure (fig.3.1).

The strains may be eliminated by depositing films at the working temperature (e.g. using a Peltier temperature controller) [19]. Increased or decreased deposition temperatures, compared to the operating temperature, result in opposing behaviour of the system and the tensile thermal stresses produced by one process correspond to compression stresses for the other.

High temperature deposition increases the possibility of diffusion, which would limit the introduced stress. The stress achieves a maximum value at the point of its creation and decreases very rapidly with depth from the source interface. Stress provides a local change in the dielectric constant of the material due to the photoelastic effect, which can be utilised to produce optical waveguides [19,20]. The laser structure of the two metal stripe contacts surrounded with a thermally grown insulating oxide on the top of GaAs/AlGaAs wafer, was computed to maximise the change of the refractive index within the semiconductor (fig.3.13), and manufactured

(fig.3.1), resulting in stress induced laser devices [24]. The structure will not be considered further in this work.

3.3.2. Insulator spinning technique.

A simple low–stress liquid spinning method, e.g. resist (section 3.2) [14] or polyimide insulator, followed by curing allows deposition of a uniform thin layer over the semiconductor, covering and smoothing the steps of the pattern. The layer thickness decreases with increased spin speed and increased liquid viscosity. The process should be performed in a dust–free enviroment at the adhesion promoting humidity of 40%.

XU–180 polyimide powder was dissolved in a mixture of Xylene:Acetophenone – 35:65 using ultrasonic agitation and a 24–hour treatment of heat and stirring, to form solutions between 7 and 18% by weight. A solution was spun on to a GaAs sample (covered with a 1μm wide and 7μm high pattern) at 4000rpm for 1min and cured for 20min at 75^{o}C, 10min at 135^{o}C, 10min at 200^{o}C, 30min at 230^{o}C and 1hr at 350^{o}C. The layer had good insulating properties, was resistant to all the chemicals tested and was etched using an oxygen plasma (section 3.4.2). A 14% solution gave a film approximately 1.4μm thick (fig.3.14), and while covering the ring laser pattern 6μm high and 2μm wide, smoothed the layout with the thickness on the top being 0.2μm. Within the 0.1μm thick polyimide layer (on the sides of the ribs), existing pinholes occasionally formed paths for further deposited metals to create narrow fuses and a short circuit to the underlaying semiconductor. These were blown up by passing a high current through the device.

3.3.3. Metal – semiconductor contact.

The semiconductor ring laser needs electrical connections for device operation. The quality of the contacts between metal and semiconductor strongly affects the performance of the device. Thermal or high electric field instabilities and subsequent surface dissociation occur because of out– or in–diffusion of various elements, and result in degradation of the contacts, change in the composition of the contacts and the device, and finally modification of their characteristics. Reliable and reproducible contacts should possess stable characteristics and an homogenous interface, and provide uniform adhesion between metal and semiconductor without the introduction of strain into the chip. They should also provide low thermal impedance, removing

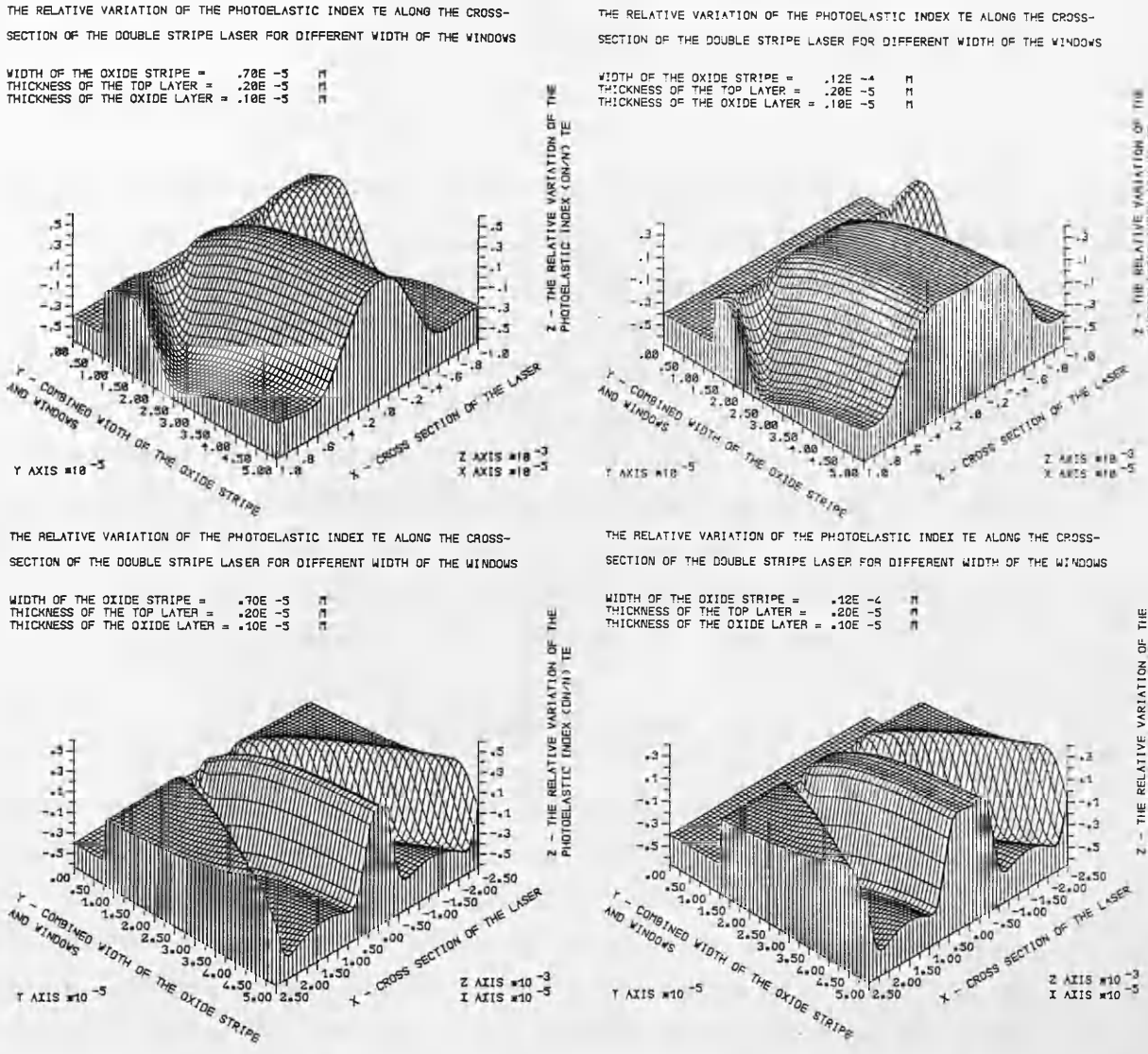

Fig.3.13. Variation of the photoelastic index across the double stripe laser device for a different width of the middle oxide stripe.

Fig.3.14. Profile of polyimide covering the ring laser rib.

heat from the device.

The type of contact is determined by the dominant mechanism of carrier transport through the barrier in the metal – semiconductor junction [25,1] and consequently by its I–V characteristic. A Schottky contact uses thermionic emission of carriers over the top of a barrier and possesses a rectifying I–V characteristic. An ohmic contact has a linear I–V characteristic with resistance much smaller than that of the device and exists for field emission (tunnelling of carriers through the whole barrier), or recombination in the depletion region of the interface. The latter mechanism requires a damaged, rough semiconductor surface, which can degrade the contact during operation. Contacts with properties between ohmic and Schottky use thermionic field emission, where, due to the narrower depletion layer and higher doping concentration, hot carriers tunnel through the top of the barrier.

3.3.3.1 Ideal and real contacts.

Classical Schottky theory [7] assumes the metal–semiconductor barrier height being equal to the difference between the metal work function and the electron affinity of the semiconductor. This applies to the defect free contact. A real semiconductor–metal interface is affected by defects, oxide layer and contaminants, creating additional surface states and producing non–uniform inter–diffusion of the constituents (section 1.1). This results in a depletion region and a 'pinning' of the Fermi level (fig.3.15) [6,8,26]. The barrier is then almost independent of the metal used and depends mainly on surface preparation and deposition techniques [26]. Non–uniform constituent interdiffusion results in localised stress initiating protruding contacting regions, with uncontrollable sizes and spacings, which increase the substrate carrier concentration.

3.3.3.2. Ohmic contacts.

Resistivity of the contact between a metal and a semiconductor ρ_c primarily depends [25,1] on barrier height Φ_b, effective mass of the carrier m_c, dielectric constant of the semiconductor ε and the carrier concentration of acceptor or donors $N_{d,a}$:

$$\rho_c \sim \frac{1}{m_c} * \exp\left(\frac{4*\pi}{h}*\Phi_b*\sqrt{m_c}*\sqrt{\varepsilon}*\frac{1}{\sqrt{N_{d,a}}}\right) \qquad (3.1)$$

Note that a decrease in barrier height or an increase in carrier concentration gives rise to a decrease in resistivity.

To achieve a low resistivity ohmic contact, the semiconductor layer adjacent to the metal should be of low band gap (e.g. GaAs on the top of GaAlAs layers) and should be very highly doped, to thin the depletion region in the semiconductor, so that field emission transport dominates, even with a high barrier.

Ohmic contacts require the conditions [1]:

$$N_{d,a} >> (\frac{k*T}{q}*\frac{4*\pi}{h})^2 * m_c * \varepsilon \qquad (3.2)$$

$N_d >> 1.7*10^{18}/cm^3$, for n− GaAs,

$N_a >> 1.25*10^{19}/cm^3$, for p− GaAs,

where: k is the Boltzmann constant, h is Planck's constant, T is the absolute temperature, q is the electronic charge, $N_{d,a}$ is the carrier concentration of donors or acceptors, m_c is the effective mass of a carrier, and ε is the dielectric constant of the semiconductor.

Surface doping can be introduced either before metal deposition, through diffusion, epitaxy or ion implantation, or, after deposition, by annealing and consequent indiffusion of dopants [1]. A combination of methods, decreasing the barrier and increasing the doping level, is the most popular way of producing ohmic contacts. A highly doped low band gap semiconductor layer is annealed with a metal structure to increase further the carrier concentration.

3.3.3.3. Conventional and improved contacts.

The conventional metal composition for an ohmic contact consists of a doping layer, a transfer layer and a bonding layer (fig.3.16). A typical example is: n− GaAs/Au− Ge/Ni/Au. During the annealing (contact formation) Au enhances the outdiffusion of Ga (of group III) from GaAs, and Ni, a fast diffuser, greatly enhances the indiffusion of Ge into GaAs [1,27]. (Ge is amphoteric and normally has a slow diffusion rate). Consequently, Ga vacancies are filled by Ge atoms (of group IV) creating a highly doped n− type layer on the GaAs surface, necessary for the ohmic contact. Similarly, a p− type ohmic contact would require the Ga vacancies to be filled by a dopant of group II (e.g. Zn, Mg, Be). The indiffusion of group IV elements into the As sides was also investigated and was found to create unstable resistive contacts. After annealing, a stable point of contact formation should be obtained. The excess unreacted material (e.g. Au from the bonding layer) may cause further contact reactions during device operation. This causes increased resistivity by outdiffusion and oxidation of Ga, and indiffusion of acceptors such as

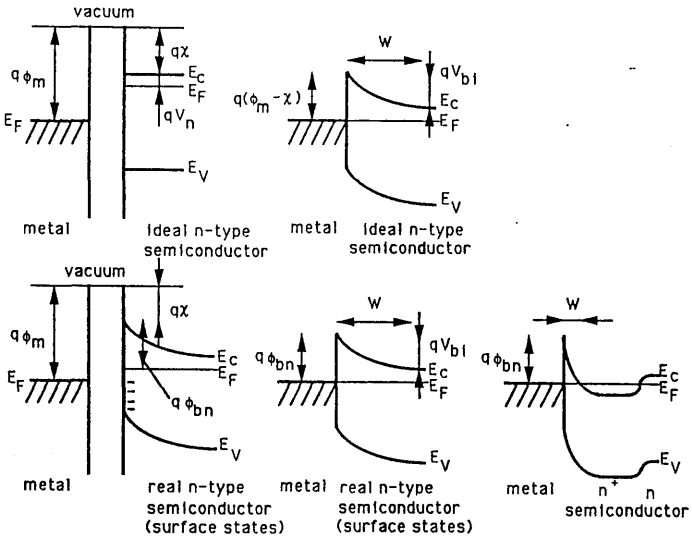

Fig.3.15. Energy diagram of the contact metal – semiconductor.

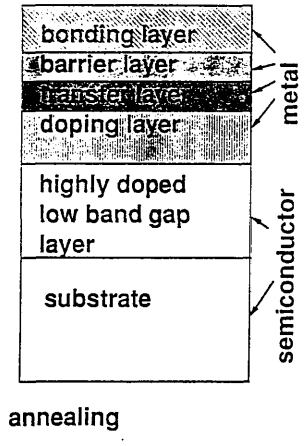

Fig.3.16. Ohmic contact composition.

Au and Ni, leading to the degeneration of the contact [1]. This implies that all layers should be thin, but thick enough to provide enough carriers. The relative thickness and the sequence of subsequent layers is critical for reliable and stable contact formation.

To avoid excessive degradation of contacts with time at the working temperature of the device (particularly for high temperature applications) and to limit the diffusion between the metallization layers (e.g. indiffusion of the top Au bonding layer and outdiffusion of the reacted contact material) an additional layer working as a diffusion barrier must be interposed between the contact layer and bonding layer (fig.3.16) [1,28,29,30,31,32,33]. This barrier should form very stable, well defined compounds with neighbouring layers, with little interdiffusion at the annealing temperature, introducing a stress, which holds the film on the surface during annealing and decreases the roughness and non-uniformity of the contact. The most common approach involves the use of high melting point metals.

Diffusive transport in polycrystalline films is dominated by diffusion along grain boundaries and dislocations at all realistic temperatures [34]. Therefore an effective diffusion barrier should not be polycrystalline within the applied temperatures. "Stuffed" barriers with plugged paths, including stable nitrides, borides, carbides or oxides, and barriers made of amorphous metal films (e.g.Ni-Mo), seem to be the most promising materials for obtaining high temperature stable metal contacts to semiconductors [29].

3.3.3.4. Contact fabrication.

Improved contacts may be produced by the correct choice of the following: materials and their surface doping levels, preparation techniques, metallic layers and their thicknesses, deposition techniques and controlled annealing conditions.

3.3.3.4.1. Surface preparation and deposition techniques.

Semiconductor surfaces were cleaned with organic solvents. Oxide reduction was carried out to reveal unspoiled GaAs using either a mixture of 30%NH_4OH : H_2O - 1:2 or HCl : H_2O - 1:1. Surface damage was removed with a polish-etch of 30%NH_4OH : H_2O_2 : H_2O - 3:1:150. The semiconductor was coated with photoresist, which was subsequently patterned. Surface de-oxidation was again

carried out through the resist pattern. Additional RF argon plasma cleaning was performed in a vacuum system, prior to metal deposition. The metallic doping and transfer layers were thermally evaporated at below 10^{-6}Torr. Slow deposition rates of 0.2nm/s were used to ensure uniform deposition. This also prevented overheating of the GaAs substrate, reducing the stress introduced into the evaporated layers, which might have caused microbreakage on cooling. A barrier layer was deposited in a separate evaporator using a focused e− beam. Two alternatives were employed: deposition in a N_2 atmosphere at 10^{-5}Torr in order to "stuff" the barrier grain boundaries [28], or evaporation without the N_2 at 10^{-6}Torr, with no consequent "stuffing". Finally, the sample was treated with nitrogen RF plasma sputtering and the top Au bonding layer was deposited in a thermal evaporator at a rate of 0.2nm/s and at a pressure of 10^{-6}Torr.

3.3.3.4.2. Controlled annealing.

Ohmic contact creation is achieved by annealing a semiconductor with metal layers containing dopant, at temperatures between 300 and 450C within the reducing atmosphere [1]. The chemical reaction products are determined by the temperature and time of annealing. Slow sintering at low temperature forms a contact by a solid phase reaction, while fast alloying at high temperature uses recrystallisation of melted alloy. The final structure of sintered and alloyed contacts are identical [1]. The necessary period of heat treatment should be optimised. Under− annealing does not produce ohmic contact behaviour while excessive annealing results in a larger interdiffusion of the volatile components and contact degradation. A new method of real time ohmic contact formation display was developed during the research into the contacts. By monitoring the I− V characteristics of the contact during heat treatment, (which can also be done with laser or ion− beam), the point at which the ohmic contact is developed can be easily found, and the temperature and duration of annealing (or power and duration of the beam) can be optimized. The system allows for analysis and stability examination of the metal − semiconductor contact. A suitable controlled heat annealing system was produced (fig.3.17). This consists of an air− tight furnace equipped with a graphite heating element (of low temperature expansion coefficient), thermocouple and two probes, stereo− zoom microscope, and a semiconductor curve tracer. The probes were placed on the metal dots on the semiconductor sample and annealing took place in an atmosphere of forming gas ($95\%N_2 + 5\%H_2$).

Development of the controlled annealing system confirmed that the annealing temperature and time should be minimal, proving that (fig.3.18):

1) Before the ohmic contact composition is annealed, the I– V characteristic has a rectifying nature (the carrier concentration is low enough to prevent a tunnelling effect for a low applied field; for higher field, however, carriers move over the top of the barrier) [1].

2) During heat treatment, the I– V characteristic changes from rectifying to ohmic and carriers tunnel through the top of the thinner barrier [1]. With too low a temperature, or too short a time (not enough dopants diffused), the characteristic changes back to almost rectifying, when the contact is cooled.

(A contact consisting of the barrier and bonding layers only, without the doping layer, will always revert back to Shottky behaviour.)

3) The ohmic contact is annealed when enough dopants have indiffused in to the surface of the semiconductor to reduce the barrier [25] and provide tunnelling of carriers through the barrier. Ohmic behaviour then improves further with decreased temperature, due to the increased low temperature hole mobility.

4) The contact will improve with time, until all the vacancies in the semiconductor surface are filled.

5) It will remain unchanged as long as dopants are still available to indiffuse to the semiconductor surface.

6) It will degrade, when there are no more dopants available and they indiffuse deeper into the semiconductor, decreasing the semiconductor surface carrier concentration. Metal constituents indiffuse into the sample and semiconductor constituents outdiffuse through the contact along grain boundaries of metals, causing very inhomogenous intermixture within the contact and on its surface. As mentioned before, these problems may be suppressed by the application of an diffusion barrier.

An understanding of the above mentioned processes made the controlled optimum annealing of an ohmic contact reasonably straightforward, and featureless, low resistivity contacts (figs.3.19,3.20) were obtained routinely, providing they were made on the bulk semiconductor material. For a semiconductor with thin layers of different doping and material composition, the situation is more complex. It is difficult to estimate the influence of thermal excitation of atoms in deeper layers on the averaged I– V sample characteristics during heat treatment. This may be overcome by testing the contacts of a bulk sample having the properties of the top semiconductor layer.

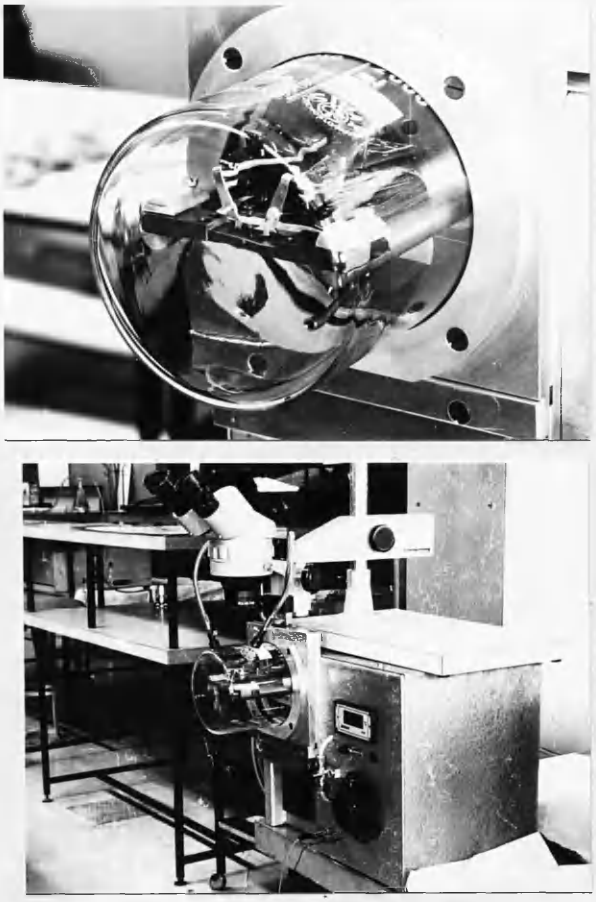

Fig.3.17. Real time ohmic contact development display system.

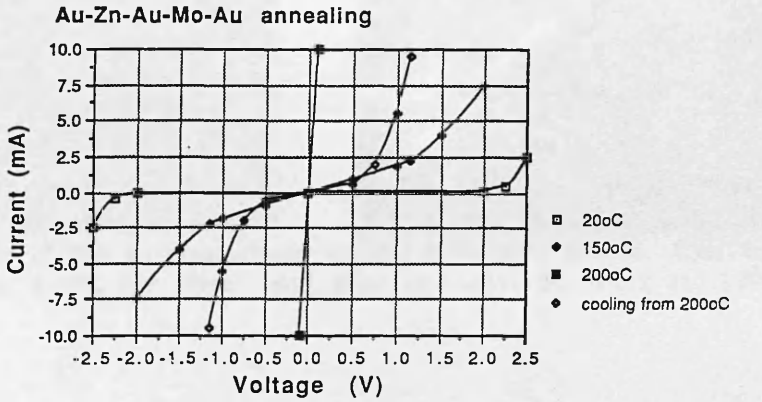

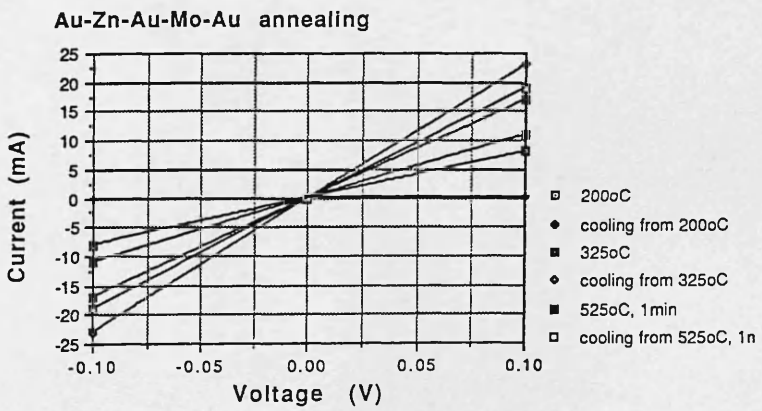

Fig.3.18. I– V characteristics of the ohmic contact composition during annealing.

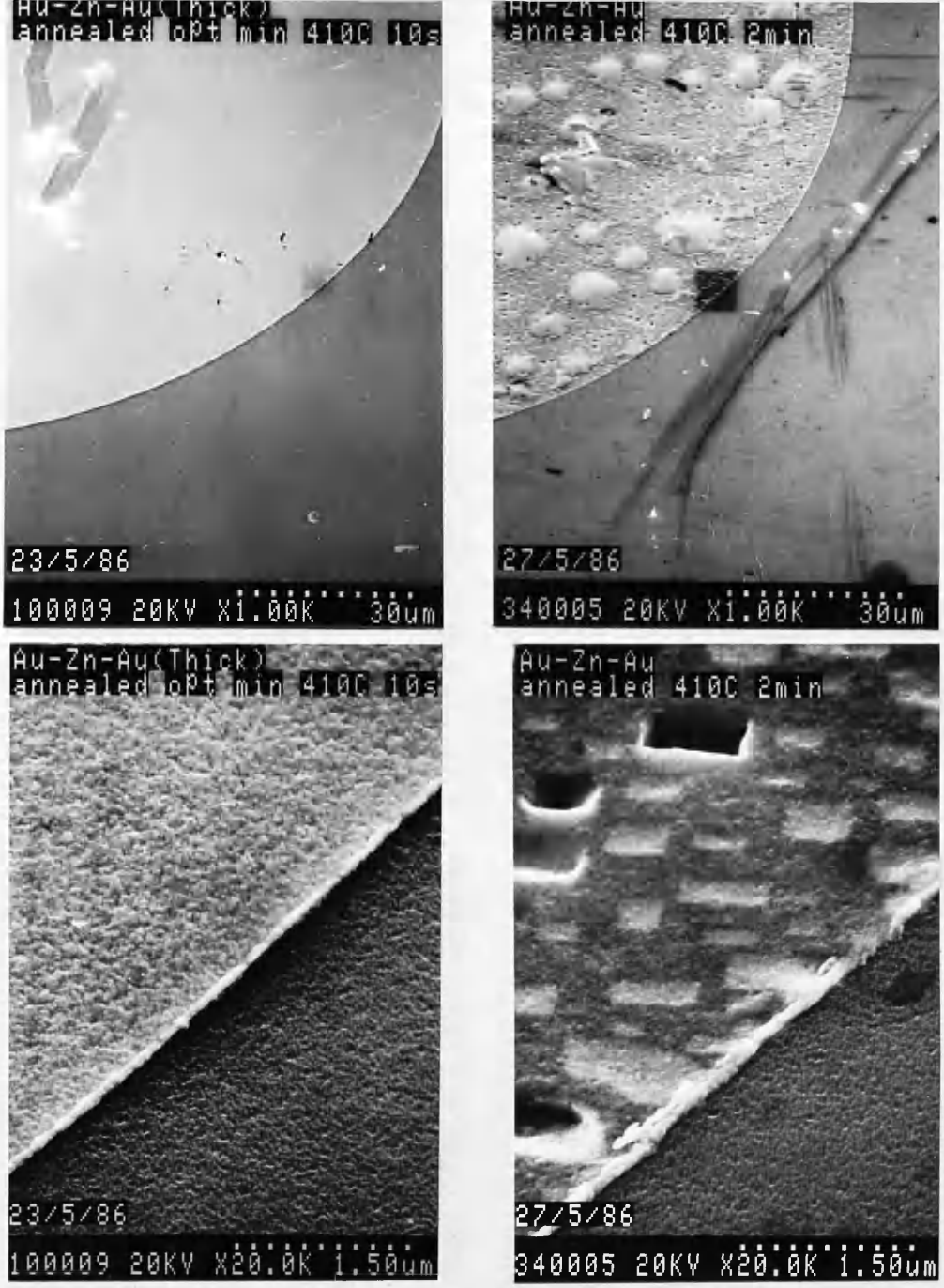

Fig.3.19. Surface view of the p— type ohmic contact without a barrier, after optimal (minimal) annealing at 410°C for 10sec., and after prolonged annealing at 410°C for 2min.

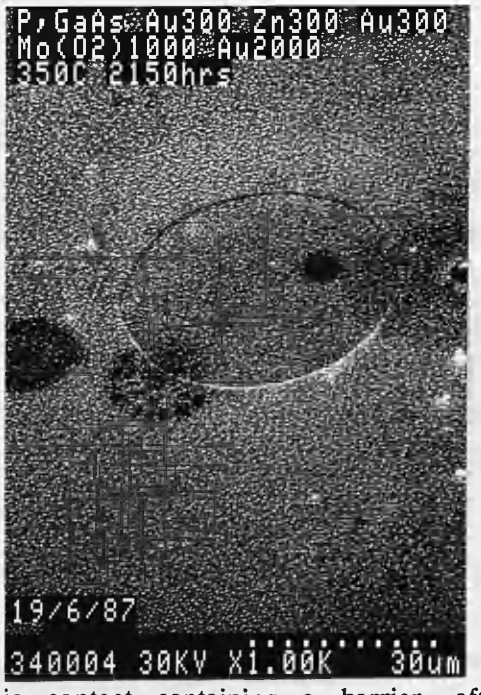

Fig.3.20. Surface view of the p– type ohmic contact containing a barrier, after optimal (minimal) annealing at 410°C for 10sec., after prolonged annealing at 525°C for 5min and after prolonged ageing at 350°C for 2000hrs.

3.3.3.5. Contact evaluation.

Contact evaluation was carried out before and after annealing, and after prolonged ageing at high temperature. The uniformity of the contact surface was examined with optical and scanning electron microscopes. The linearity of the I– V characteristic between the contacts was checked with an I– V curve tracer, confirming their ohmic behaviour [35,36]. The specific contact resistivity was measured using a modified four– point method (fig.3.21) [37,38]. This method uses 4 equidistant spacing s circular contacts of diameter d ($d<<s$), arranged on a straight line, on an infinite plane of relatively small thickness w ($w<<s$). A current source was applied between contacts 1 and 4 (I_{14}) and the voltage drop was measured between contacts 1 and 2 (U_{12}), or 2 and 3 (U_{23}). The specific contact resistivity ρ_c may be calculated for [37]:

$$\rho_c = A * R_c > \frac{\rho * d^2}{4 * w} \qquad (3.3)$$

where: ρ is a resistivity of the semiconductor and A is the contact area, and is then equal to [37]:

$$\rho_c = \frac{A}{I_{14}} * [U_{12} - \frac{U_{23} * \ln(\frac{3*s}{d-0.5})}{2*\ln 2}] \qquad (3.4)$$

The chosen pattern of d= 50um, s= 1000um, w= 500um enables us to measure a contact resistivity of $\rho_c = 2.5*10^{-6} \Omega cm^2$ for highly doped p– type GaAs (ρ= 20mΩcm) and of $2.5*10^{-7} \Omega cm^2$ for highly doped n– GaAs (ρ= 2mΩcm).

3.3.3.6. P– and n– type GaAs Schottky contacts.

Excessively doped (above $10^{20}/cm^3$) GaAs forms ohmic contacts with metals [24]. Moderately doped GaAs forms Schottky contacts to most of the materials, if not annealed. Annealing of the system incorporating dopants results in their diffusion and changes contact properties to ohmic. The materials preventing the dopant diffusion with stable rectifying characteristics to GaAs, are used as barriers or insulators. Their characteristics are non– Schottky above 150°C and ohmic above 300°C and revert back to rectifying on cooling. The investigated layers of 200nm thick SiO_2 and 100nm thick high melting point metals, like Cr, Ti, NiCr, Mo, TZN Mo alloy or Hastelloy C, formed good morphology dopant barriers to both p– and n– GaAs. The were all stable after 5s to 5min treatment at 500°C. The barriers were degraded by reducing their thickness and improved with incorporation of the opposite dopant.

3.3.3.7. P– and n–type GaAs ohmic contacts.

Materials doped in excess of $10^{20}/cm^3$ readily formed an ohmic contact to any metallisation, e.g. to a stable Cr–Au composition. Ohmic contacts to moderately doped GaAs consist of the optimised doping, transfer, barrier and Au bonding layers. The contact should be reliable, stable and have good morphology. Alloys are not advisable due to inhomogeniety, different vapour pressures and consequent lack of repeatability. Practical contacts were surrounded with an insulating layer of 200nm SiO_2 while the top Au layer created larger, overlapping pads.

3.3.3.7.1. Ohmic contacts to p–GaAs.
High temperature ohmic contacts to p–GaAs.

Reliable p–type ohmic contacts to GaAs increase the doping level by substituting group III Ga with the elements of group II [10,39], e.g. Zn. Some of these systems were investigated, starting with a composition of transfer/doping/bonding layers of Au(30nm)/Zn(30nm)/Au(200nm). The contact became ohmic on annealing at 350°C (with resistivity $1*10^{-3}\Omega cm^2$) and showed reduced resistivity on optimal annealing at 410°C for 10s ($1.5*10^{-5}\Omega cm^2$), providing excellent morphology (fig.3.19). Further annealing at 410°C for 2min resulted in excessive contact indiffusion degrading the morphology (fig.3.19) and in increased resistivity up to $4*10^{-5}\Omega cm^2$. The additional NiCr layer covering the contact had little influence on contact resistivity although it degraded the morphology on prolonged annealing.

The thermal stability and morphology of the starting contact, both before and after annealing, were improved within the system with an additional barrier layer incorporated between the doping and the bonding layers. The doping layer was still covered with 30nm of Au for antioxidation purposes and its small thickness reduced contact resistivity to $8*10^{-6}\Omega cm^2$. Various barrier materials of thickness 100nm were tested and Mo, TZN Mo alloy and Hasteloy C were found to maintain the original contact resistivity and caused little degradation to the morphology, even at prolonged ageing for 2000hrs at 350°C or 5min at 525°C (figs.3.20, 3.22). A Ti barrier was also effective although it allowed for some diffusion. The carbide and silicide barriers (B_4C, WSi_2, $NbSi_2$) produced stable, good morphology contacts with highly increased resistivity ($5*10^{-3}\Omega cm^2$), and prevented the adhesion of the Au bonding layer. The SiO_2 layer maintained its insulating properties after the 5min treatment at 500°C for

layers thicker than 200nm.

The contacts produced were exposed to air (oxidised) before the evaporation of a Au bonding layer. The barriers could be further improved with nitrogen "stuffed" grain boundaries, using evaporation within an N_2 atmosphere, followed by treatment with N_2 RF plasma sputtering (fig.3.22).

Ohmic contacts to GaAs, using the substitution of group V arsenic, with the elements of group IV, e.g. Ge, Si and Ti, was also investigated. Compositions incorporating Si required a high content of Ni catalyst (e.g. Ni(30nm)/Si(30nm)/Ni(50nm) and annealing at 400°C produced relatively stable ohmic contacts, with a high resistivity of $2*10^{-3}\Omega cm^2$ and a non-linear I-V characteristic. A composition incorporating Ti annealed at 400°C produced ohmic properties (resistivity $2*10^{-4}\Omega cm^2$), which rapidly degraded on further annealing (rectifying, $10^{-2}\Omega cm^2$). A composition incorporating Ge formed unstable contacts which, with increasing annealing temperature alternated between ohmic and Schottky behaviour.

In conclusion, ohmic contacts using a substitution of As with the elements of group IV produce considerably worse results than contacts using a substitution of Ga with the elements of group II, and should therefore be avoided.

3.3.3.7.2. Ohmic contacts to n-GaAs.

Reliable n-type ohmic contacts to GaAs increase the doping level by substituting group III Ga with the elements of group IV, e.g. Ge. Amphoteric Ge is a slow diffuser [27] and both Au and Ni catalysts are necessary to produce ohmic properties. The annealing temperature can be reduced to an acceptable 400°C with a proper combination of both ingredients. The resultant micro-nodular Ni-As-Ge and Au-Ga grains [6] provide a low resistivity contact. Uniformity of the outdiffusion of Ga may be improved with an additional layer of Ga [40], while an additional barrier layer suppresses the total intermixture of the contact with bonding layers, improving the stability of contacts.

Single elements rather than eutectic alloys should be deposited to ensure the repeatibility of contact characteristics. To form an alloy of $Au_{.88}Ge_{.12}$, the relative thickness of Au to Ge layers should be about 2:1 and a 40nm thick Ge layer

provides a sufficient number of donors. The optimal thickness of Ni [41,42] is then 20nm. Both Ni and Ge form alloys with Au, while Ni forms a compound with Ge. Ge and Ni must have been separated by Au to decrease the annealing temperature to a reasonable 400°C. The chosen system of Ge(40nm)/Au(60nm)/Ni(20nm)/Au(20nm)/Mo(100nm)/Au(200nm) was optimally annealed at a temperature of 405°C for 10sec producing good morphology, low resistivity contacts ($2.5*10^{-6}\Omega cm^2$), reasonably stable at increased temperature ($7.5*10^{-5}\Omega cm^2$ after 1100hrs aging at 350°C).

Systems which were not optimised, required increased annealing temperatures and resulted in degraded stability, due to the inefficiency of the system or an excess of unreacted material. This was also affected by the layer sequence. Compositions incorporating Ge as a first layer allowed for a large tolerance of ±50% of the content of Au and Ni without increasing the annealing temperature. Careful control of both Ni and Au layer thicknesses was required for those systems in which either of them was incorporated as the first deposited layer.

In a separate investigation and a different annealing system, the diffusion depth of Ge to GaAs was investigated. Diffusion depends on temperature, dopant concentration gradient and the number of available states within the semiconductor lattice. Amphoteric Ge may additionally compensate for doping by indiffusion on to both Ga and As vacancies [6].

Diffusion of the Ge from the contacts of 40Ge/60Au/20Ni/200Au through the determined thickness of insulating GaAs layer to the highly doped n− GaAs substrate can be detected by measuring the resistance between two contacts. For the non− diffused contact, this is dominated by the resistance of the insulator, while for the diffused contact, this is dominated by the much smaller resistance of the contact and the substrate for a diffused contact (fig.3.23). Assuming the point of ohmic contact creation to be ≃ 10Ω, the Ge dopant diffuses through a 0.02μm insulating layer (depletion depth) during the annealing cycle, reaching an indicated temperature of 195°C, through 0.1μm at 212°C, 0.3μm at 242°C and 0.5μm at 300°C.

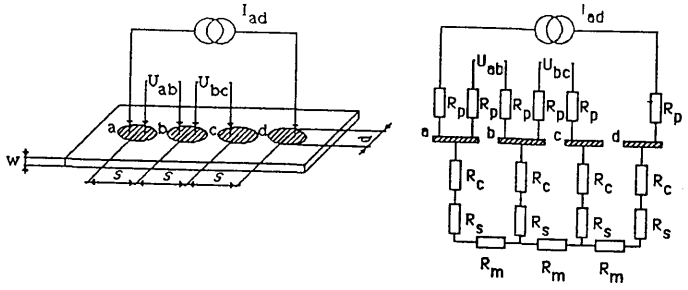

Fig.3.21. Specific contact resistivity measurement using modified four– point method.

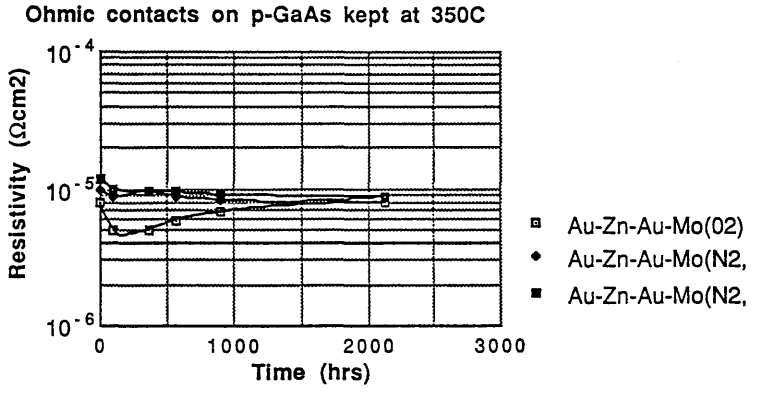

Fig.3.22. Resistivity of the p– type ohmic contacts containing molybdenum barriers kept at 350°C for 2000hrs.

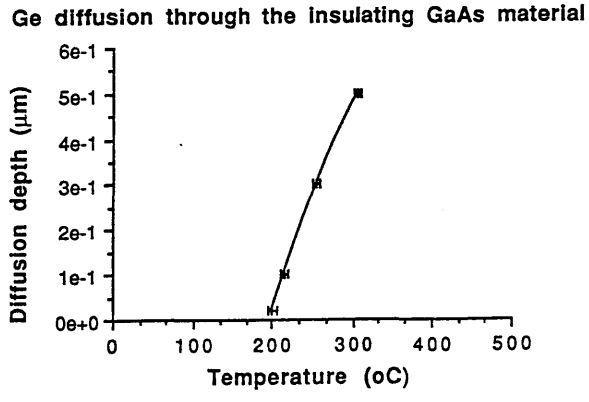

Fig.3.23. Diffusion of Ge from the ohmic contact to GaAs substrate at different temperatures.

3.3.3.7.3. Ohmic contact composition to both n– and p– type GaAs.

The number of device fabrication process steps may be limited if both n– and p– type ohmic contacts to the GaAs are produced at the same time using a single metallisation step. P– and n– type GaAs require Au/Zn/Au and Ge/Au/Ni/Au systems, respectively (sections 3.3.3.7.1, 3.3.3.7.2). The systems of: p– type– metallisation to n– GaAs, and n– type– metallisation to p– GaAs, are of rectifying characteristics. The deposition sequence of various metals and their thicknesses are critical in producing ohmic contacts to both n– and p– type GaAs.

The systems of Ge/Zn followed by Au or Ni/Au produced, at a low annealing temperature of 410°C, good ohmic contacts to p– GaAs, while rectifying properties to n– GaAs, probably due to formation of a barrier for indiffusion of the Au and Ni.

The Ge/Au/Zn system followed by Au formed good ohmic properties to both n– and p– GaAs when annealed at 450°C. The additional Ni/Au layers degraded the contact resistivity, particularly for the p– GaAs, probably due to an excess of the catalysts.

The Zn/Ge/Au/Ni/Au system produced, at a low annealing temperature of 410°C, excellent morphology ohmic contacts to both p– and n– GaAs, with a resistivity of $2*10^{-5}\Omega cm^2$ for p– GaAs and $2*10^{-6}\Omega cm^2$ for n– GaAs. Again, both Ni and Au layers of defined thicknesses were required and the stability of the contacts was assured with the additional Mo barrier layer. The chosen stable composition was therefore: Zn(30nm)/Ge(40nm)/Au(30nm)/Ni(20nm)/Au(30nm)/Mo(100nm)/Au(200nm). The performances of the contact to both n– and p– GaAs were similar to the best separate n– and p– type contact compositions to GaAs.

3.4. WET CHEMICAL ETCHING.

Throughout the laser device fabrication process, wet etching was used to perform several functions: to thin the sample (deep, flat etching), to remove contaminated and damaged layers providing a flat, stress– free surface (shallow, 20 to 100nm flat etching), to produce surface and sidewalls of a chosen shape (e.g. mesa isolating a device, recess etch prior to metallisation, or accessing the underlaying layers) and to selectively remove or highlight different layers.

Wet etches convert the etched elements into compounds that are soluble in the etchant which may be then carried away. The etching process relies on: a diffusion of fresh reagants through the processed etching solution, adsorption, diffusion through the oxide to the GaAs interface, oxidation, formation of soluble complexes, their dissolution, and diffusion of the dissolved products through the etch solution away from the oxide–etch interface [6]. The etches are both diffusion and reaction–limited depending on the relative quantity of solvent and complexing and oxidising agents. The diffusion process results in an undercut beneath the mask material, which limits the smallest dimensions of the pattern and reduces resolution. The etches leave behind a layer of 7 to 30nm of reaction products [6,8] (for etch traces and oxide removal see section 3.1).

The rate of reactions between reagents and different materials vary considerably, providing the possibility of selective etching. The etching of polycrystalline and amorphous materials (e.g. metals and dielectrics) proceeds isotropically [6,8,9,43]. Diffusion limited etching of crystalline materials (e.g. GaAs) tends to polish the surface by providing more agents to protrusions. Reaction limited etching of crystalline materials maintains the surface topography for shallow etching and, due to different rates and selective reactions with Ga and As atoms, becomes anisotropic along the preferential crystal planes with walls of a predetermined profile, for deeper etching [6,8,9] (fig.3.24). The mixture of various reagants and controlled etching conditions is necessary to obtain the desired etch profile.

Selective etching through a pattern requires the mask to be well defined, removable, well adhering [6,7] and etch resistant. Masks may be made of organic polymers, or of tougher metals and dielectrics.

The number of etching methods and solutions is extensive. The etch rate depends on the properties of the materials, pretreatment, surface contamination, the preliminary oxide layer (sections 3.1, 3.2), temperature [6,44], doping, defect density, agitation and pattern size, and must be tested and corrected for particular samples. Various etches are presented in [6,8,9,43,7,44,45,46,47] and other reviews.

3.4.1. GaAs etches.

The following chemical etchants were found to be useful throughout the laser device fabrication:

1. $NH_4OH:H_2O_2:H_2O$ – 3:1:150; 90 to 180nm/min (20°C; no agitation); 50nm/min (5°C, no agitation); leaves 7nm oxide; polishing; shallow etch (up to 300nm); flat bottom; no trenching; (anisotropic for deeper etch [9]); 30sec produces 0.05μm deep and 1.5μm wide undercut beneath the masks; does not remove resist nor most metals (e.g. Ni – Cr); polishing etch.
2. ($KClO_3:H_2O$ – 1g:100ml):HCl – 1:50; 240nm/min (20°C, no agitation); in a different experiment: 43nm/30sec, 80nm/min, 100nm/2min (20°C, weak agitation); recess etch (20nm) prior thin film deposition (fig.3.25); improves adhesion; does not remove resist; no trenching.
3. $HNO_3:H_3PO_4:H_2O_2:H_2O$ – 1:1:1:x; x= 0 3μm/min (deep etch); x= 3 1.5μm/min; x= 9 0.3μm/min; x= 27 0.06μm/min; (20°C, weak agitation);
4. $H_3PO_4:H_2O_2$:ethylene glycol – 1:1:3; clouding of the surface; (anisotropic); relatively independent of doping concentration [9]; few sec. process at 0°C results in improvement of laser mirror facets; no trenching; does not remove resist.
5. ($AgNO_3:H_2O$:HF – 0.3g:40cm^3:40cm^3):($CrO_3:H_2O$ – 40g:40cm^3) – 1:1; staining etch; a few sec. treatment reveals dislocations and delineates interfaces of materials of different composition or doping (difference of 3 to 5*10^{18}/cm^3 can be detected); for fine structures; e.g. 200nm; dilution with H_2O – 1:5 is advised; [48].
6. AZ developer; causes partial etching of GaAs.

Each of the above etches was used for different purposes. For example: to polish the sample, to provide pattern undercut, to improve adhesion of deposited layers, to produce deep etched pattern, to improve laser mirror facets or to reveal material dislocations.

3.4.2. GaAs "oxide" layer etches.

GaAs oxides were removed using:

1. HCl:H_2O – 1:1; 5min; followed by H_2O and solvent rinse; does not remove resist; may remove metals.
2. $NH_4OH:H_2O$ – 1:2; 5min; followed by H_2O and solvent rinse; does not remove resist nor most metals (e.g. Ni – Cr).

Both deoxidising agents were equally effective.

3.4.3. Insulator etches.

Insulators were etched using the following etchants:

SiO_2

1. $HF:H_2O$ – 1:5; etches AlGaAs and GaAs.
2. $HF:NH_4F$ – 1:6; 100nm/min; (buffered HF) [3]; does not remove resist; etches AlGaAs and GaAs.

Polyimide

1. N– methylpyrrolid– 2– one.
2. Acethophenone:Xylene– 65:35.
3. γ– butarylactone.

All three etches were equally effective.

3.4.4. Metal and alloy etches.

Metal layers were etched using the following etches:

Au, also Au– Zn– Au– Ti– Mo– Ti– Au system

1. ($KI:H_2O$ – 55.6g:50ml); adjust pH to 5.5 with HCl or NaOH, add 32g of I_2; if the etch is too quick dilute with H_2O – 1:5; the etch is selective to GaAs; does not remove resist.
2. $HCl:HNO_3$ – 3:1; 25– 50μm/min; removes thick layers; destroys most resists, metals, and semiconductors.

In, also indium oxide

1. HCl; for the longer treatment of thick layer removal; the unetched wafer side should be covered with wax.
2. HNO_3:HCl– 2:1.
3. Mercuric chloride:Dimethylformamide (DMF)– 100g:500ml; u/s; rinse with DMF and change when murky; carcinongenic; very effective.

Ni, also NiCr– 9:1

1. HCl; does not etch GaAs; resist nor Au; removes GaAs oxides; etches AlGaAs.
2. $HCl:H_2O$ – 1:1; Does not etch GaAs nor resist; removes GaAs oxides; etches AlGaAs.
3. $HNO_3:H_2SO_4:H_3PO_4$:glacial acetic– 3:1:1:5; [3].
4. $Ce(HSO_4)_4:H_2O:HNO_3$ – 2g:20ml:10ml.

Mo

1. HNO_3:HCl:H_2O– 1:1:3.
2. HNO_3:H_2SO_4:H_2O– 1:1:3.
3. HNO_3:H_3PO_4:acetic acid:H_2O– 2:5:4:150; 0.5μm/min; does not remove resist.

The choice of specific etch was determined by the combination of materials present in the sample and the etch selectivity.

3.5. DRY ETCHING.

Dry etching uses a combination of chemical reactions with a directional physical ion–bombardment of the processed surface, using a plasma of noble or reactive gases, to produce highly anisotropic structures with vertical walls, applicable to rib ring laser devices. The process aims for high selectivity of materials, smooth etched surfaces and low damage to the sample. The plasma is initiated by either electrons moving between the electrodes (plasma process) or by an external ion beam (ion beam process) [49].

Dry etching ranges from purely chemical plasma etching (PE), through the mostly chemical, reactive ion etching (RIE), to the mostly physical, reactive ion beam etching (RIBE) or assisted ion beam etching (AIBE), and to purely physical with a different level of ion acceleration: ion beam etching (IBE), sputter etching (SE) and plasma sputter cleaning (PSC) [49,50]. The more chemical reactions improve material selectivity.

All the plasma assisted processes, in particular those using higher energy non–reactive ions, introduce damage to both the bottom and sidewalls of the material due to dislocation, diffusion and redeposition, limiting the minimum dimensions of the final device [51] (fig.3.26). Crystal damage can not be annealed out [52] although it could probably be avoided at temperatures above 150°C [6]. The deposition and diffusion of the reaction products and the plasma constituents may be annealed out at temperatures above 900°C using an arsenic overpressure or an encapsulant [53]. Trapping of the charges generated within the surface [6] degrade Schottky contacts and may be annealed out at 400°C. The damaged layer can be removed with a wet etch or partly removed by deoxidation.

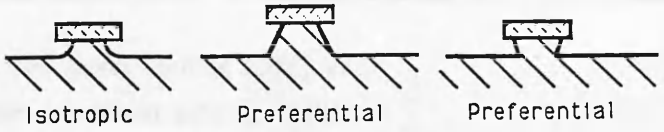

Fig.3.24. Isotropic and preferential wet etching of GaAs.

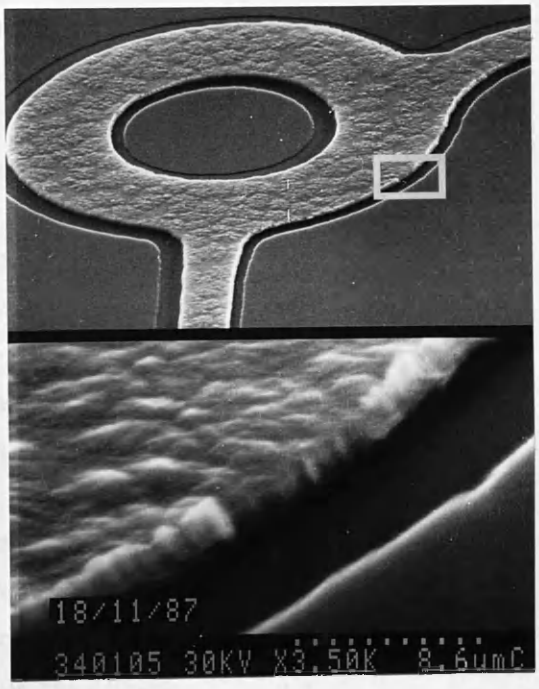

Fig.3.25. Recess etch followed by metallisation.

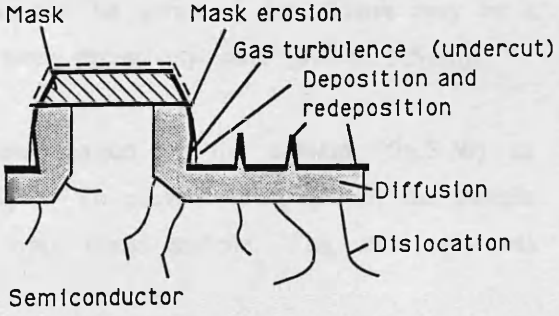

Fig.3.26. Damage to the surface during dry etching.

3.5.1. Ion beam etching (IBE) and Reactive ion beam etching (RIBE).

Ion, or reactive ion beam etching uses physical collisions to sputter the target atoms, using an inert or reactive–gas external ion beam source [49,54] with energy exceeding the target binding energy. Reactive etching requires lower energy. Low etch selectivity reduces the influence of contaminants [9], and limits the use of thinner masks.

The Oxford Applied Research 2255 system using argon produced vertical etch walls of GaAs material, for beams incident onto a rotating sample at an angle of 22° to the normal [49] (fig.3.27). It requires high beam energy and resulted in a crosslinked polymer mask and in semiconductor damage which extended to depths between 100 and 300nm [49,51]. The process was not developed further.

3.5.2. Ion sputter etching (ISE) and Reactive ion etching (RIE).

The system uses inert or reactive gas positively charged ions produced by a discharge between parallel plates, to bombard the target electrode and the sample, negatively biassed with respect to the plasma [55,56], using a D.C. supply or a matched rf generator through a capacitor, which encourages high mobility electrons to leave the plasma towards the electrodes. Since the average electron current densities at each electrode are of the same order, the non–symmetric system results in a higher voltage drop to a smaller electrode with the target sample.

A Electrotech RIE80 system at the optimum power of 100W [51] was used to etch GaAs–AlGaAs laser material using reactive $SiCl_4$. A Ni/Cr mask was used with an etch selectivity to GaAs of 1:80. Damage was assessed by a 4 probe measurement of the conductivity of etched wires made of a highly doped 0.5μm thick GaAs layer [Rahman, Glasgow Univ. (fig.3.28)] indicating damage depth of 40 to 60nm (fig.3.29) [49] for a prolonged 40min. etch, which can not be annealed out. There may be a large estimation error, since the wires used were excessively wide (0.7 to 3.5μm).

The quality of RIE is influenced by contamination of the system (fig.3.30) or semiconductor sample (fig.3.4), and redeposition. To prevent redeposition, the sample was placed on top of a larger, constant area GaAs sample. The etch rate was

1.)

2.)

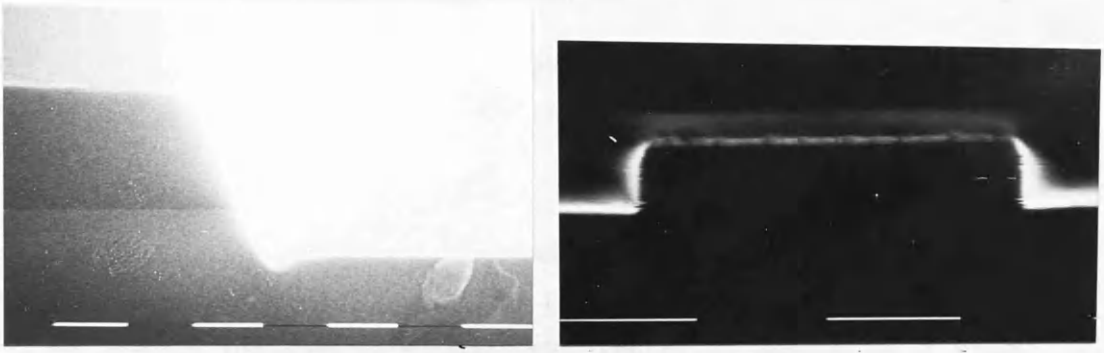

Fig.3.27. Ion beam etched GaAs surface at 1.) 0° and 2.) 22° angles of the incident beam.

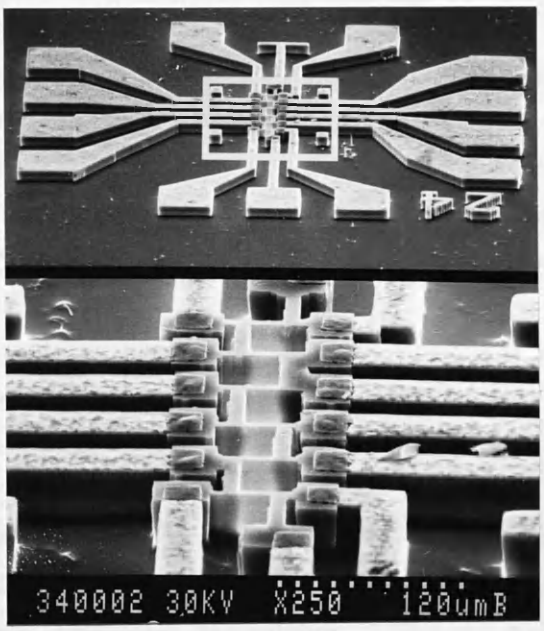

Fig.3.28. $SiCl_4$ etched pattern of thin conductive wires used to evaluate the damage to the surface [Rahman M., Glasgow University (1989)].

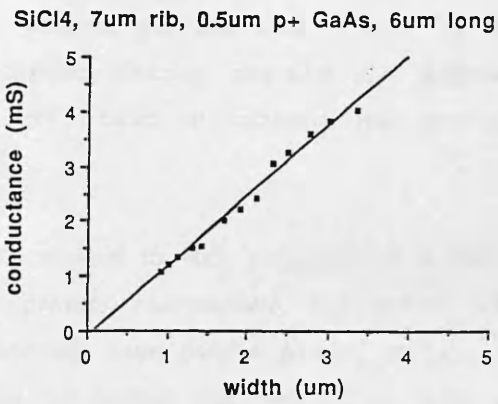

Fig.3.29. Conductance of different width $SiCl_4$ etched wires [After Rahman M., Glasgow University (1989)].

reduced due to both a reduced distance to the plasma, resulting in a reduced voltage (fig.3.31), and an increased area of GaAs, resulting in a loading effect [57] (fig.3.32).

The etched wall profile is controlled by the input power [51] and gas pressure [58]. Increased pressure enhances the reflection and turbulence from the bottom surface producing an undercut (figs.3.33, 3.34, 3.35) and resulting in the loss of a small pattern. At low pressures of 5mtorr for $SiCl_4$, the etched walls were almost vertical and enabled production of a high aspect ratio pattern of 7μm in height and 0.4μm wide (figs.3.36, 3.37).

The Electrotech RIE80 system at 100W power was also used to etch polyimide using oxygen [54,59]. To prevent redeposition the samples were placed on top of a large Si or GaAs wafer. Etching produced electrical damage to the semiconductor, indicated by an increased resistance between ohmic contacts with etch time. The damage was reversed by annealing at 420°C for 10sec, but due to the possibility of non-annealable optical damage, the process was not developed further.

3.5.3. Plasma sputter cleaning (PSC) and Plasma etching (PE).

Plasma sputtering and etching use low potential electrodes (< 50V), which result in low surface damage [49]. The etcher may be a coil, parallel plates or a barrel configuration with electrodes of similar sizes. Optimised gas mixture, pressure, flow rate and RF power contribute to production of vertical wall profiles.

A 100W coil system with argon was used to clean the semiconductor and to improve both adhesion and ohmic contact properties. Nitrogen gas was used to improve the barrier contact layer [54,59] (section 3.3). Sputter cleaning degrades the Schottky contacts [51], unless they are subsequently heat treated to consume the damaged layer (e.g. Pt/Pd [60]).

The Plasmafab 505 barrel etcher was used with oxygen to etch polyimide at a speed of 0.9μm/hour, with little damage [49]. To prevent redeposition, the sample was placed within a glass petri-dish (fig.3.38). Polyimide spun over a pattern of 1μm in width and 7μm in height, was 1.4μm thick on the bottom and only 0.2μm thick at the top of the pattern. The etch revealed the top and still left the insulator on the

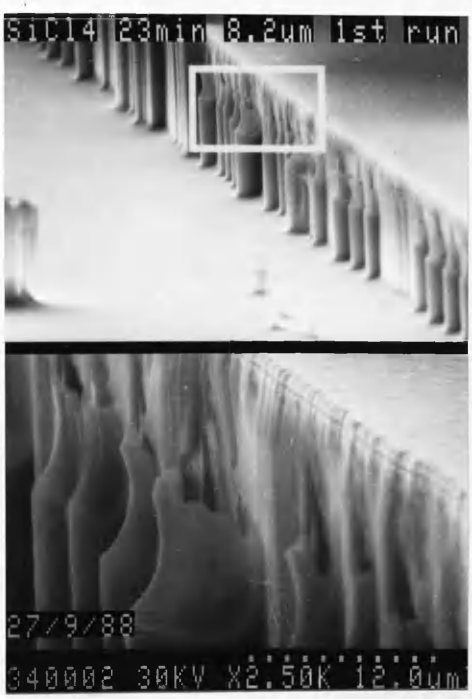

Fig.3.30. Redeposition from the contaminated system, degrading the $SiCl_4$ etch.

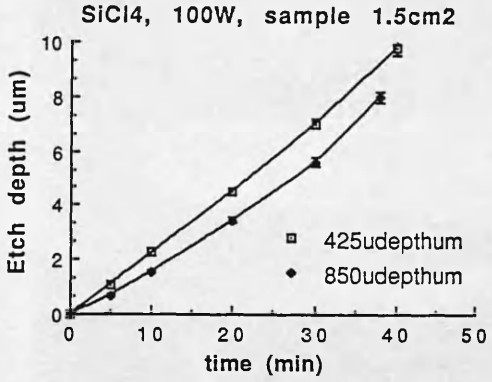

Fig.3.31. $SiCl_4$ RIE etch rate dependence on the height of the sample.

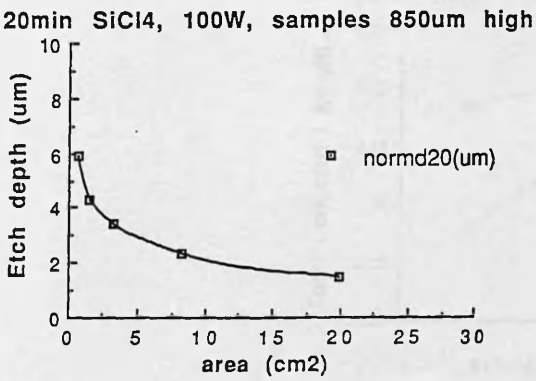

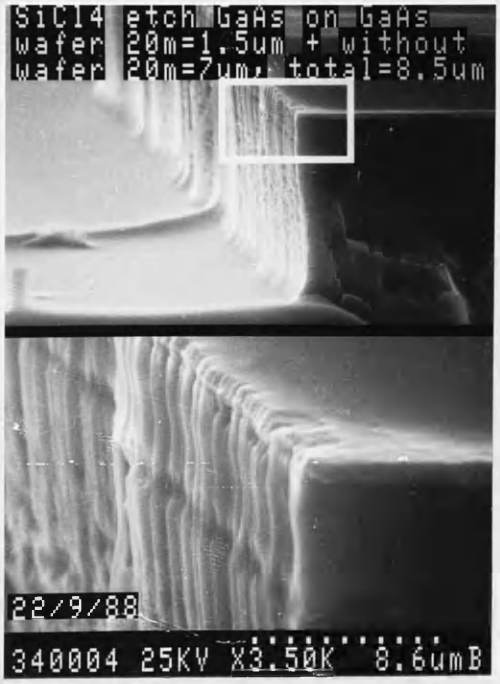

Fig.3.32. $SiCl_4$ RIE etch rate dependence on the area of the etched sample.

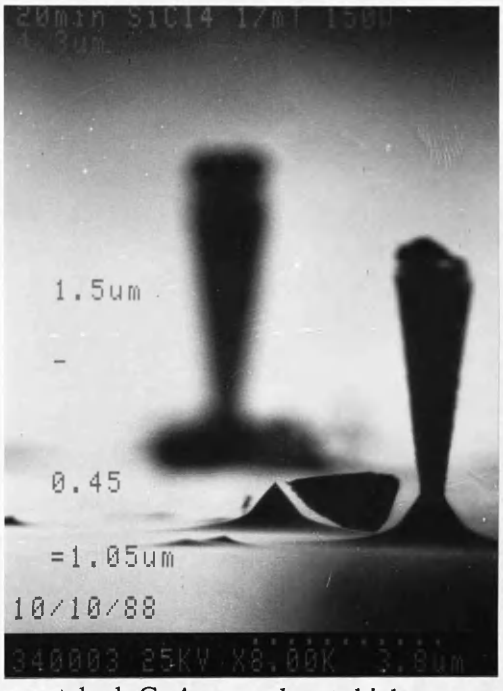

Fig.3.33. Profile of $SiCl_4$ reactive ion etched GaAs sample at high pressure.

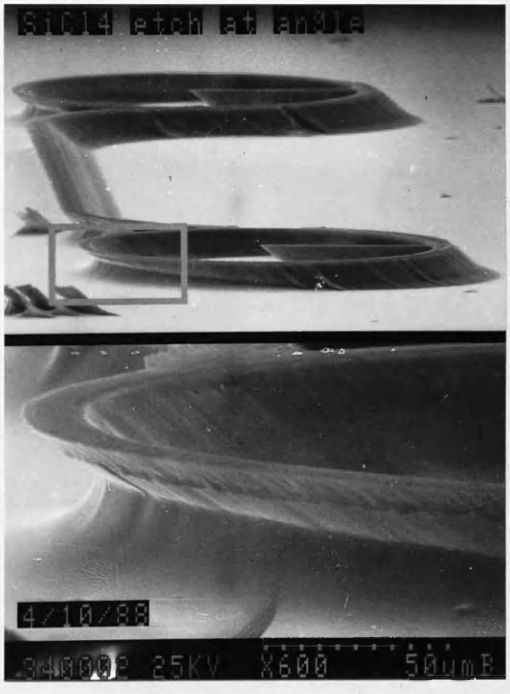

Fig.3.34. Profile of $SiCl_4$ RIE at angle of the GaAs sample.

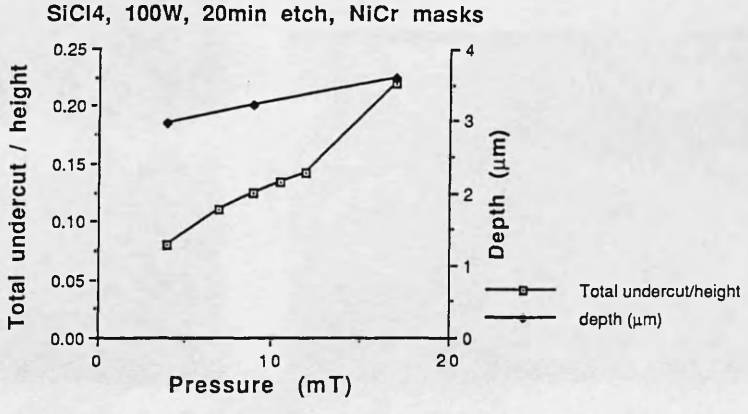

Fig.3.35. Influence of pressure on the undercut of the pattern during the $SiCl_4$ RIE.

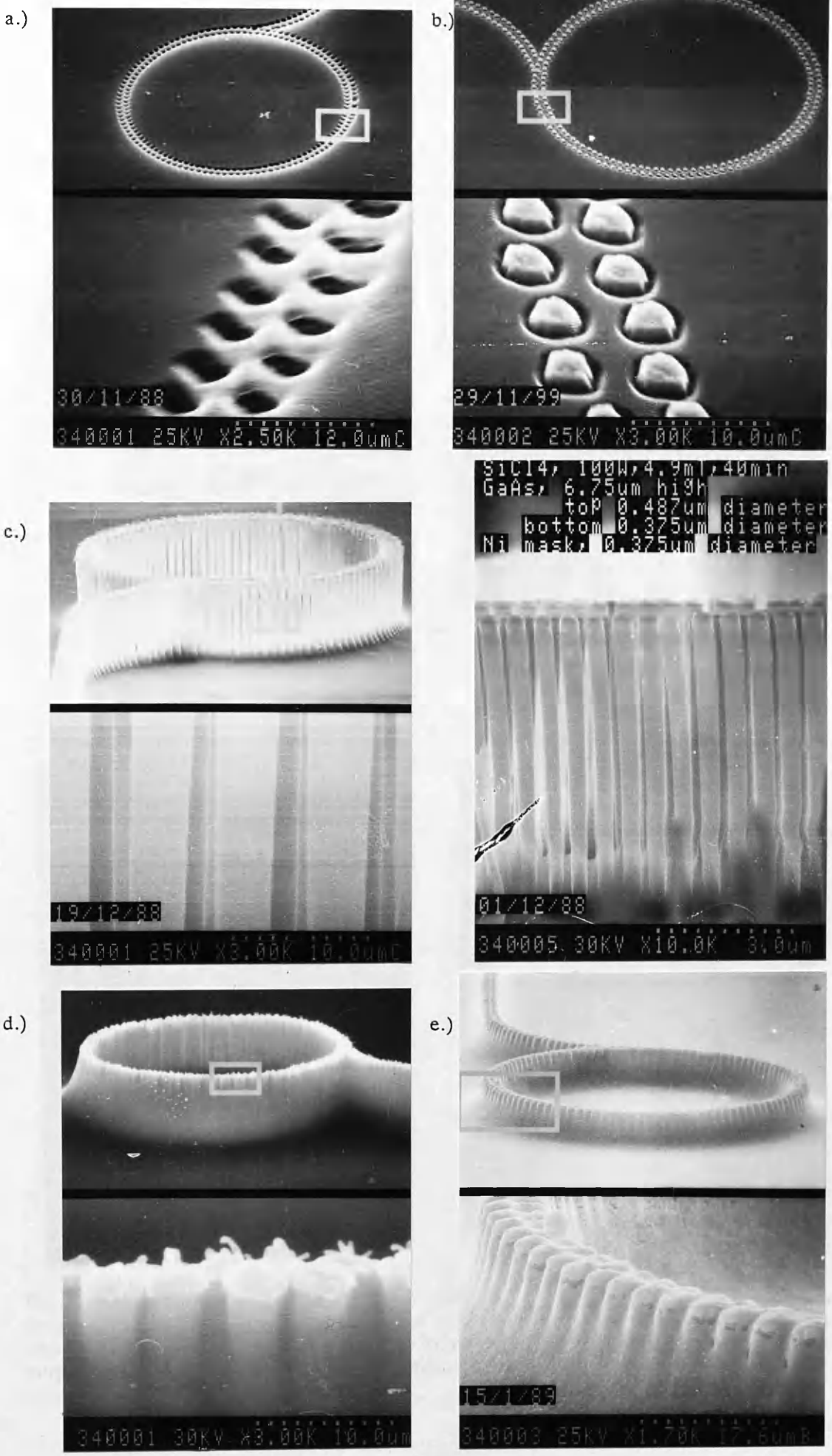

Fig.3.36. A dot pattern allowing evaluation of the processes: a.) pattern in resist, b.) metal pattern, c.) pattern etched through the metal mask using $SiCl_4$ RIE, d.) pattern as c.), covered with polyimide and etched using O_2 plasma, e.) pattern as d.) followed with metallisation.

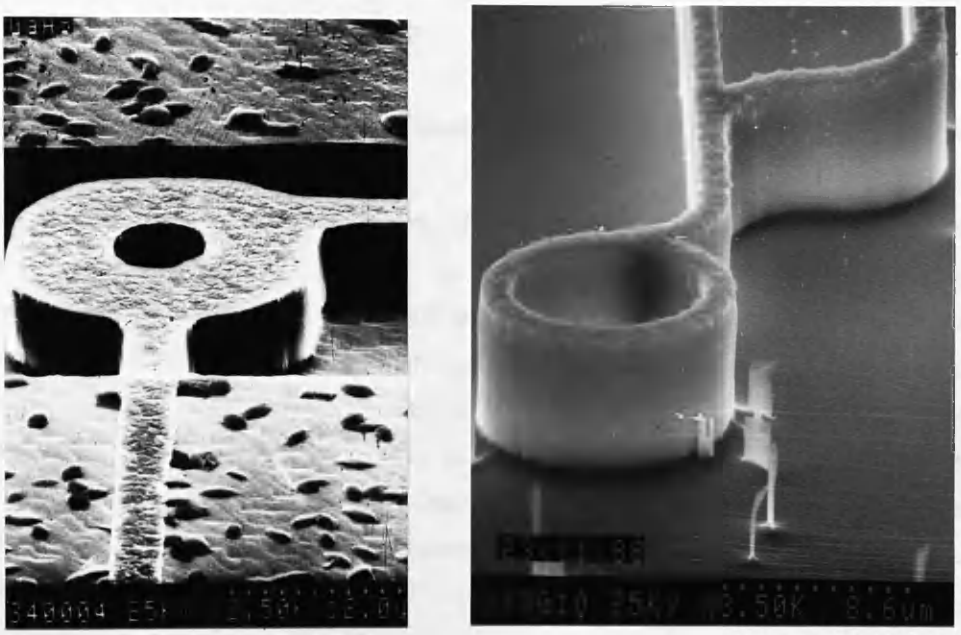

Fig.3.37. Ring laser $SiCl_4$ etched pattern.

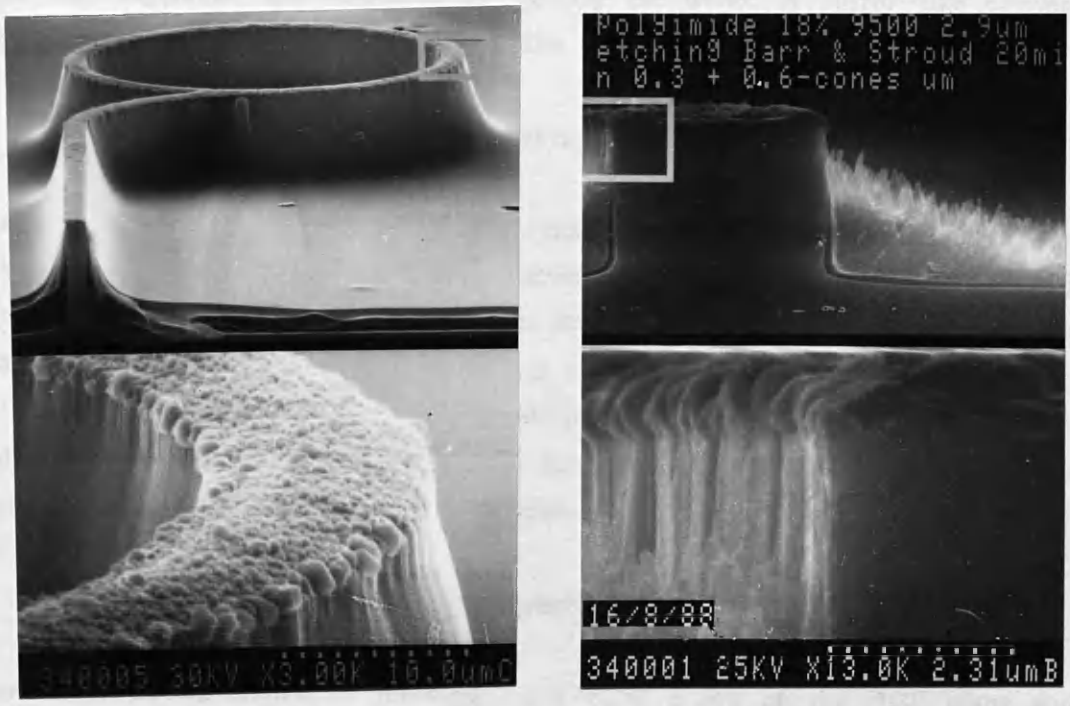

Fig.3.38. GaAs ring laser device pattern etched with $SiCl_4$ RIE through the ohmic contact mask down to 7μm, and covered with polyimide spun all over the sample, which, in turn, was etched using O_2 PE to reveal the top of the pattern for contact purposes. Also, redeposition of a badly etched polyimide.

sides and bottom of the pattern (fig. 3.38).

3.5.4. Conclusion.

Dry etched patterns require a combination of physical ion bombardment to provide high anisotropy, with chemical reactions to assure a high etch selectivity. Both processes have disadvantages: the increased energy produces non–annealable crystal damage, while low power chemical processes introduces a high influence of contamination on the etch quality. The RF power and the gas pressure may control both the slope of the walls and the quality of etching. Etch uniformity was found to be better at low pressures. The etch rate increases with temperature and a decreased area of the target material. Various low damage processes were investigated and used to produce ring laser devices.

3.6. DEVICE CLEAVAGE.

A processed semiconductor wafer usually contained a number of ring laser devices and their separation was completed by cleaving the wafer. A mirror–like cleavage plane provided a scatter–free output to other optical components.

3.6.1. Crystal cleavage properties.

Gallium arsenide posesses a zinc–blend crystalline structure [61,6]. There are three crystal lattice plane groups considered in device applications: {100}, {110}, and {111}. A single bond, between the atoms of the subsequent layers of the chosen specific plane can easily be broken and assures good cleavage properties between those layers [61]. This happens for (110), (111) and planes laying between these two [6]. Subsequent (111) planes incorporate single populations of Ga or As and the dipole face created [61] makes cleaving more difficult.

3.6.2. Laser device grinding and cleavage.

GaAs laser devices should be produced on a water grown on the {100} plane and cleaved along the two or four (110) planes, perpendicular to the waveguiding and lasing directions. The practical wafer grown with a 2 degree misalignment away from the required (100) plane provides necessary stress and bonding forces initialising epitaxial growth [62]. This may degrade the cleavage properties.

A substrate thickness of 100μm with a stress free, mirror finish to the back of the wafer, provided good strength and allowed reproducible cleavage into small, 400*400μm chips. The wafer was waxed on to the jig along with thicker Si samples and lapped using solutions of 9μm, followed by 3μm alumina polishing powders on glass bases, followed by 3μm powder diluted with a mixture of 1:3 of bleach : water on a microcloth. The Si samples prevented excessive pressure being put onto the softer GaAs sample, enabling thinning of a wafer with a fragile pattern (e.g. 7μm high and 0.3μm wide, fig.3.38). The wax was subsequently removed with boiling trichloroethylene.

Cleavage planes were initialised with etched grooves or scribes. The sample was then sandwiched between plastic transparent films, placed upside-down on to a rubber base, of chosen hardness, and pressed gently with a scalpel blade along the scribed lines to complete the cleave (fig.3.38).

Cleavage of the GaAs wafer resulted in electrostatic charges increasing the handling difficulties of very small devices. The charges could be dissipated using vapours of solvents and the devices were handled as other static devices according to BS5783:1984 regulations.

3.7. PACKAGES.

A package should protect the laser chip, introduce heat dissipation and provide a stress-less mechanical and electrical interface between the chip and the header to simplify its manipulation [63,8].

3.7.1. Bonding.

Packaging of small laser chips using a conductive glue or indium solder was established, using a specially designed bonder (fig.3.39). The hand rests and the XYZ-manipulators equipped with a sharpened Q-tip or a probe, were used to deposit a controlled amount of conductive epoxy or to place an indium sphere in a flux, and position a laser chip on the edge of the package (fig.3.40), which was held by vacuum to a hot plate. The top contact was made using gold wire, soldered to one of the header pins (fig.3.41). The header was covered with a cap for further protection.

Conductive adhesives should be viscous for 1min for handling purposes, produce a flat, well defined small spot [64] and avoid outgassing during the curing process. Three adhesives: A120, A310 and A53O [64] with a methyl cellosolve thinner, were used to mount the small laser chip onto the header. The chip was positioned on to the top of a glue spot and the glue was cured at the recommended temperature of 150°C for 1hr.

Indium based solders possess better heat and electrical conductance than adhesives. Their softness ensures that low tensile strains are introduced into the sample [65]. A 100% indium solder requires a rubbing motion [66], a flux [67] or a high temperature annealing to reduce its surface tension and provide bonding. A solder sphere covered with flux was squashed with a Q− tip at a temperature of 100°C. Above the melting point of 156°C, the laser chip was pushed into the solder and the sample was then cooled rapidly.

The ultrasonic and thermo− compression bonding of gold wires to the top contacts was tested. The available bonder was not recommended for smaller chips, where the optical path could be damaged via micro− breakage.

3.7.2. Thermoelectrically cooled package.

An increased operating temperature affects the lifetime of semiconductor ring laser, increasing threshold current, decreasing optical power output and introducing a shift and a broadening of the spectral peak.

Controlled heat removal from the device may be performed using a thermoelectric (peltier) cooled package (fig.3.42). Small Au− Al thermoucouples made of 25μm thick wires or evaporated materials, with a temperature sensitivity of: $\Delta V = 3.5*10^{-6}*\Delta T$ [V/°C] [68], were used to sense the temperature of various points of the semiconductor laser chip (section 4.1.1). The system showed that the temperature drop across the wafer was of the order of 100°C. The cooling system forces the attached device surface to be at a chosen temperature and does not affect the temperature distribution within the laser, merely shifting the field by a controlled value of temperature [68]. The cooler requires therefore to be controlled by the temperature of the heat source, to stabilize the laser operation and to prevent a degradation of the device. The laser junction should therefore be positioned close to

fig.3.39. Home made bonder for precision bonding of small laser chips using conductive epoxies or a solder.

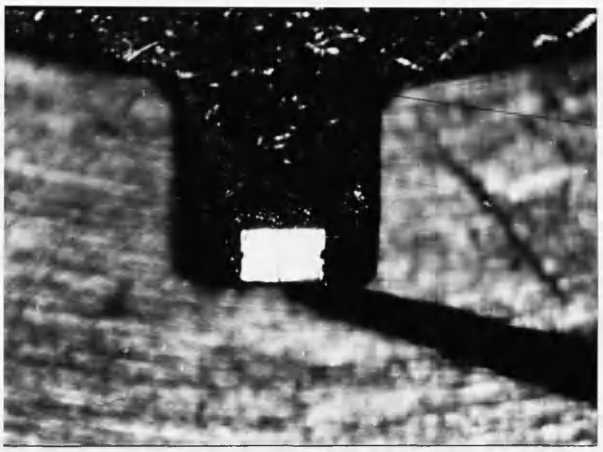

Fig.3.40. Bonding of the laser chip.

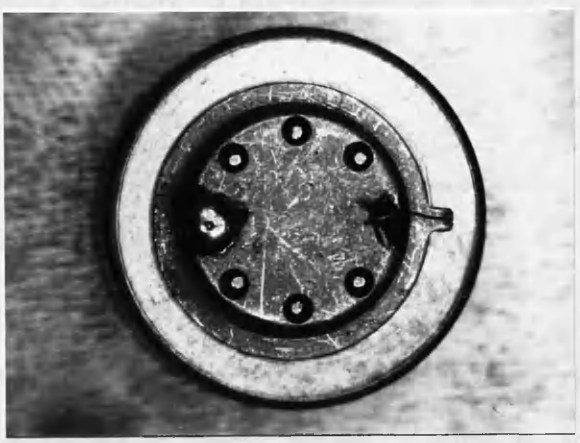

Fig.3.41. Laser chip mounted onto the TO−5 package.

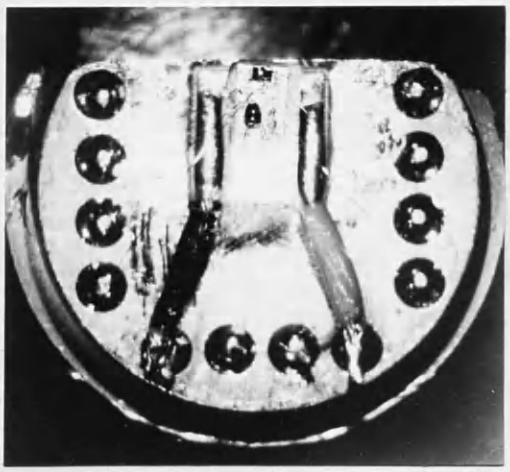

Fig.3.42. Thermoelectrically cooled package.

the cooler (i.e. mounted up–side–down) or its temperature could be sensed by the small thermocouples, presented above. The temperature controller was driven with a much larger and slow responsing thermistor placed near the device (fig.3.42), degrading the cooling properties. The temperature of the whole system increases if the heat sink capability is smaller than the input power. The performance of the laser cooled with a cooler is presented in Appendix 2.

3.8. REFERENCES.

[1] Piotrowska A., Guivarch A., Pelous G.: Ohmic contacts to III–V compound semiconductors: a review of fabrication techniques, Solid State Electr., Vol.26, pp.179–197 (1983).

[2] Chang C.C., Citrin P.H., Schwartz B.: Chemical preparation of GaAs surfaces and their characterisation by Auger electron and X–ray photoemission spectroscopies, J.Vac.Sci.Techn., Vol.14 (4), pp.943–952 (1977).

[3] Stewart C.E.E.: Preparation of GaAs surfaces for epitaxial deposition, Solid State Electr. 10, pp.1199–1200 (1967).

[4] Ing S.W., Minden H.T.: Open tube epitaxial synthesis of GaAs GAP, J.Electrochem.Soc. Solid State Science and Techn., Vol.109, pp.995–997 (1962).

[5] Adams A.C., Pruniaux B.R.: Gallium Arsenide surface film evaluation by ellipsometry and its effect on Schottky barriers, J.Electrochem.Soc. Solid State Science and Techn., Vol.120 (3), pp.408 (1973).

[6] Howes M.J., Morgan D.V. eds.: Gallium Arsenide, John Wiley & Sons Ltd (1985).

[7] Sze S.M, ed.,: VLSI Technology, McGraw–Hill, New York, (1983).

[8] Ghandi S.K.: VLSI Fabrication Principles, Wiley, NY (1983).

[9] Vossen J.L., Kern W., eds.: Thin Film Processes, Academic, NY (1978).

[10] Encyclopedia of Chemical Technology – Gallium, J.Wiley & Sons NY (1978).

[11] Thompson G.H.B.: Physics of semiconductor lasere devices, J.Wiley & Sons (1980).

[12] The Shipley Chemicals ltd.: Shipley AZ Photoresists, Information Sheets, Coventry, U.K. (1988).

[13] Hatzakis M., Canavello B.J., ShawJ.M.: Single–step optical lift–off process, IBM J.Res.Dev., 24, 4, pp.452–460 (1980).

[14] Mimura Y.: The mechanism of overhang formation in diazide/ novolak photoresist film by chlorobenzene soak process, J.Vac.Sci.Technol. B4 (1), pp.15–21, (1986).

[15] Lee K.Y., Frost J., Stanley C., Patrick W., Mackie W.S., Beaumont S.P.

Wilkinson C.D.W.: Fabrication of ultrasmall devices on thin active GaAs membranes, report. Glasgow University (1986).

[16] Kratschmer E.: Verification of a proximity effect correction problems in electron–beam lithography, J.Vac.Sci.Techn., 19(4), pp.1264–1268, (1981).

[17] Mackie W.S.: Techniques and applications of very high resolution electron beam lithography, PhD Thesis, Glasgow University (1984).

[18] Mackie S., Thoms S., Adams J.: DESIGN manual, Glasgow University (1988).

[19] Benson T.M.: Integrated optical components produced in GaAs and InP epitaxial layers using the photoelastic effect, PhD Thesis, University of Sheffield (1982).

[20] Benson T.M., Murotani T., Robson P.N, Houston P.A.: A nowel electro–optically controlled directional coupler switch in GaAs epitaxial layers at 1.15μm, IEEE Trans.Electr.Dev., Vol.ED–29 9, pp.1477–1483 (1982).

[21] Kirkby P.A., Selway P.R., Westbrook L.D.: Photoelastic waveguides and their effect on stripe geometry GaAs/ GaAlAs lasers, J.Appl.Phys. 50(7) pp.4567–4579 (1979).

[22] Liu H.D., Feng Z.C., Gno Z.Z.: The stresses and photoelastic effects in stripe geometry GaAs–GaAlAs DH lasers with masked and selective thermal oxidation (MSTO) structure, IEEE J.QE–19 (6) pp.1016–1020 (1983).

[23] Liu H.D.: GaAs–GaAlAs DH lasers with photoelastic index – guiding, a proposal and preliminary experimental results, report, Glasgow University (1984).

[24] Jezierski A.F.: Integrated Semiconductor GaAlAs laser device technologies, report, Glasgow University (1985).

[25] Gupta R.P., Khokle W.S.: Transport across a high–low barrier and its influence on specific contact resistivity of a metal – n–GaAs ohmic contact, IEEE Elect.Dev.Lett., Vol.EDL–6 (6), pp.300–303 (1985).

[26] Braslau N.: Ohmic contacts to GaAs, Thin Solid Films, 104, pp.391–397(1983).

[27] Marlow G.S., Das M.B., Tongson L.: The characterisation of Au–Ge based ohmic contacts to n–GaAs including the effect of aging, Solid State Electr., Vol.26, 4 pp.259–266 (1983).

[28] Nowicki R.S., Wang I.: Improvement of the diffusion barrier properties of rf–sputtered molybdenum, J.Vac.Sci.Technol., Vol.15(2), pp.235–237 (1978).

[29] Wiley J.D., Perepezko J.H., Nordman J.E., Guo K.J.: Amorphous metallizations for high–temperature semiconductor device applications, IEEE Trans.Ind.Electr., Vol.IE–29 (2), pp.154–157 (1982).

[30] Shappiro J.R.: Diffusion barrier in advanced semiconductor device technology, Solid State Techn., pp.161–166 (1985).

[31] Nicolet M.A.: Diffusion barrier in thin films, Thin Solid Films, Vol.52, pp.415–443 (1978).

[32] Anderson W.T., Christou R.A., Davey J.E.: Amorphous thin film diffusion barriers on GaAs and InP, Thin Solid Films, Vol.104, pp.57–67 (1983).

[33] Allan D.A.: Stability of Schottky barriers at high temperatures for use in GaAs MESFET technology, IEE Proc.pt.I, Vol.133, pp.18–24 (1986).

[34] Gupta D., Campbell D.R., Ho P.S.: Grain boundary diffusion, Thin film interdiffusion and reactions. J.M.Poate, K.N.Tu, J.W.Mayer eds., New York, Wiley, ch.7 (1978).

[35] Cox R.H., Strack H.: Ohmic contacts for GaAs, Solid State Electr., Vol.10, pp.1213–1218 (1967).

[36] Cohen S.S.: Contact resistance and methods for its determination, Thin Solid Films, 104, pp.361–379 (1983).

[37] Kuphal E.: Low resistance ohmic contacts to n– and p–InP, Solid State Electron., Vol.24, pp.69–78 (1981).

[38] Fang Y.K., Chang C.Y., Su Y.K.: Contact resistance in metal–semiconductor systems, Solid State Electron., Vol.22, pp.933–938 (1979).

[39] Papanicolau N.A., Christou A.: Au–Mg improved contacts to p–GaAs, Electr.Lett., Vol.19, 11, pp.419–420 (1983).

[40] Sebestyn T., Mojzes I., Szigethy D.: Use of Ga in metal GaAs contacts to eliminate large As loss peaks, Electr.Lett., Vol.16, 13, pp.504–505 (1980).

[41] Patrick W., Mackie W.S, Beaumont S.P., Wilkinson, C.D.W.: Low temperature annealed contacts to very thin GaAs epi–layers, report, Glasgow University (1985).

[42] Henry H.G., Dawson P.E., Lennlos Z.J., Kim H.: Hot plate alloying for ohmic contacts to GaAs, IEE Trans.Electr.Dev. Vol.ED–31, 8 pp.1100–1103, (1984).

[43] Tegart :The electrolytic and chemical polishing of metals, (1978).

[44] Stark J.G., Wallace H.G.: Chemistry data book, J.Murray ltd., London, pp.85 (1978).

[45] Maisell L.I., Glang R. (eds): Handbook of thin film technology, Mc Graw Hill, N.Y. (1970).

[46] Stirland D.J., Straughan B.W.: A review of etching and defect characterisation of GaAs substrate material, Thin solid films, 31, pp.139–170 (1976).

[47] Walsh R.J. at al.: Process for polishing semiconductor material, U.S. patent: 3, 170, 273, Feb.23, (1965).

[48] Olsen G.H., Ettenberg M.: Universal stain/etchant for interfaces in III–V compounds, J.Appl.Phys., Vol.45 (11), pp.5112–5114 (1974).

[49] Doughty G.D.F.: Dry etching of III–V semiconductor materials, Semiconductor International'85 Conference, NEC Birmingham (1985).

[50] Webb A.P.: Dry processing GaAs for integrated optics, Semiconductor International'83 Conference, NEC Birmingham (1983).

[51] Doughty G.D.F., Thoms S., Cheung R., Wilkinson C.D.W.: Dry etching damage to GaAs and InP, proceedings of IPAT87, Brighton (1987).

[52] McCaughan D.V., Murphy V.T.: Low-energy ion bombardment of silicon dioxide film on silicon, 2. inert ambient annealing of degradation in MOS devices, J.Appl.Phys.44, pp.3182 (1973).

[53] McCaughan D.V., Murphy V.T.: Low-energy ion bombardment of silicon dioxide films on silicon, J.Appl.Phys.44, pp.2008 (1973).

[54] Mogab C.J.: Ion beam, plasma and reactive ion etching, Inst.Phys.Conf.Ser. 53, pp.37-54 (1980).

[55] Hofler K., Wellerdieck K. : RF sputtering for substrate cleaning, R & D Lab., Balzers A.G., Furstentum, Liechtenstein, Technical report BB800 015DE (8310).

[56] Johnson D.: Plasma etching processes, European Semicond. Design & Production, pp.37-39 (1984).

[57] Mogab C.J.: The loading effect in plasma Technology, J.Electrochem.Soc., 124 (8), 1262-1268 (1977).

[58] Thoms S., Beaumont S.P., Wilkinson C.D.W., Frost J., Stanley C.R.: Ultrasmall device fabrication using dry etching of GaAs, Microelectronic Engineering 5, pp.249-256 (1986).

[59] Flamm D.L., Donnelly V.M.: The design of Plasma Etchants, Plasma Chemistry and Plasma Processing, Vol.1 (4), pp.317-373 (1981).

[60] Poate J.M., Tu K.N., Mayer J.W.: Thin films - interdiffusion and reactions, Wiley, NY, 1978.

[61] Rieck H.: Semiconductor lasers, MacDonald, London (1974).

[62] Fergusson I.: private communication, University of London, U.K. (1990).

[63] Reiner R.: VLSI packaging, Electr.Comm., Vol.58, 4, pp.440-446 (1984).

[64] J.Matthews Chemicals: Conductive Adhesives Catalogue, Royston, Hertfordshire, U.K. (1986).

[65] Beiser R.B.: A technique of soldering to thin metal films, The review of Sci.Instr., Vol.25, 2, pp.180-183 (1954).

[66] BTRL, private communication (1987).

[67] Encyclopedia of Chemical Technology: Solders and brazing alloys, J.Wiley & Sons NY 1978.

[68] Chen W.: Thermal problems in semiconductor ring lasers, B.Sc. thesis, Glasgow University (1989).

4. STRIPE RIB RING LASER DEVICES.

4.0. INTRODUCTION.

The Fabry–Perot resonator configuration puts a constraint on the incorporation of semiconductor lasers with other integrated optical devices in a monolithic optical circuit, and various solutions have been proposed [Mertz–1]. We have been investigating the lasing waveguide formed in a continous ring, thus eliminating the need for any other optical feedback mechanism and increasing its integration ability [Matsumoto–2, Liao–3, Wang–4]. An integrated Y–junction may then be used to couple part of the light out of the ring. The laser ring resonator with a Y–junction branching output guide is to be discussed throughout this work (fig.4.1).

4.1. DESIGN AND DEVELOPMENT OF THE RIB RING LASER.

The original designs for the rib ring lasers consisted of a circular lasing ring waveguide, with a Y–junction to an actively pumped output waveguide, defined by the top metallic ohmic contact (fig.4.1); Pill–box resonators were also fabricated, as were structures with etched reflecting facets, consisting of a hollow square with reflectors at 45^{o}, at the corners, providing a light path parallel to the sides of the square [Jezierski–5]. In addition, insulated from the semiconductor, bonding pads with thin bridges to the contacts of the optical structures were provided, since the waveguide pattern was too fine to bond to contact wires. All the structures were defined by a single etching process by reactive ion etching through the semiconductor heterostructure layers, using the metallic contact pattern as a self–aligned mask.

The etched outer boundary to the laser waveguide rings maximised the index step of the guide, thus reducing considerably the radiation loss of the bent guide [Austin–6, Marcatili–7] (section 1.6.1). The high index step enabled production of ring laser structures between 10 and 100μm in diameter (fig.4.2), reduced by a factor of 100 compared to weakly guiding, low loss, diffused passive ring waveguides [Walker–8, Walker–9]. Two alternative confinement mechanisms have been applied on the inner side of the ring: either an etched inner boundary to the waveguide (to maximise the confinement), or weak stress and carrier induced confinement (to suppress higher order modes) [Jezierski–10]) (fig.4.3) resulting in "whispering gallery" modes (section 1.6).

The ring loss and the gain around the laser ring necessary to sustain oscillation are

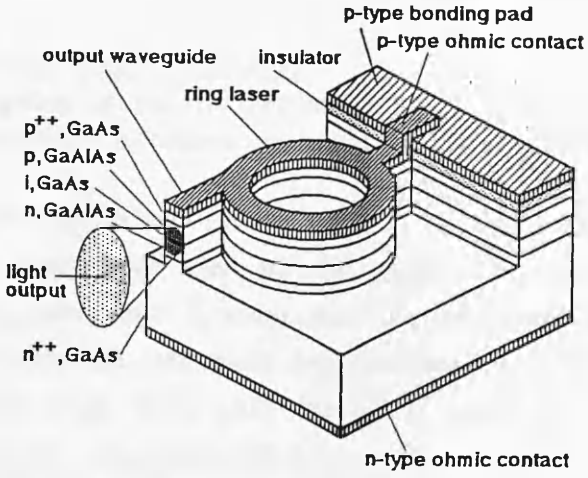

Fig.4.1. Ring rib laser device.

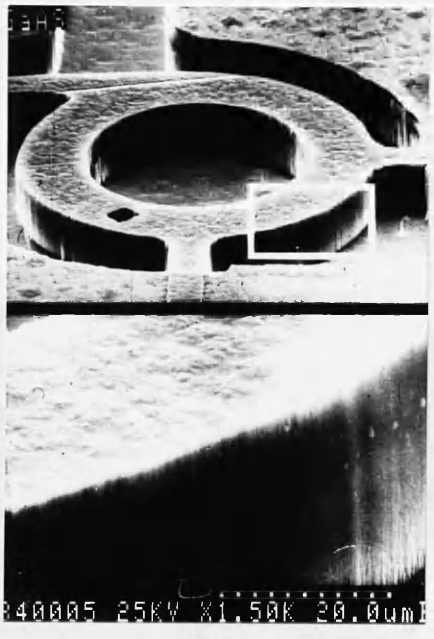

Fig.4.2. Ring rib laser devices produced using photolithography.

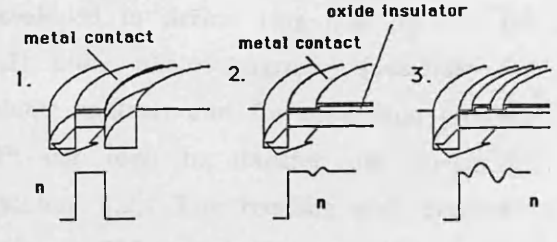

Fig.4.3. Light and carrier confinement mechanisms within the stripe of the active layer on the outer and inner boundary of the ring waveguides:
1) rib, index guiding confinement,
2) single stripe carrier– and stress–induced confinement for inner boundary of the ring,
3) double stripe carrier– and stress–induced confinement for inner side of the ring.

increased by the splitting ratio of the Y– junction and its loss (fig.4.1) (section 1.7). The coupling loss is reduced by the high index step of the guide. The ring oscillations are enhanced within the ring guide which is wider than the output guide (section 1.7). In addition, wider guides reduce the total guide loss (sections 1.6, 1.7). The ring guides used were between 4 and 10μm wide, while the output guides were between 3 and 5μm, easily made using photo– lithography (fig.4.2).

The bonding pads of the original ring laser design were unsatisfactory; the conductive bridges to the ohmic laser contacts were unable to carry the high currents needed and fused under all but very short current pulse operation. The distribution of the current around the ring was also uneven, since the resistance of the patterned metallic conductors is not negligible. An alternative design placed the bonding pad within the ring, but the rings were so small that the bonding process was unsuccessful.

The ring lasers were therefore developed further, improving the definition of the device and making narrower waveguides (down to 0.6μm) by using electron– beam lithography. In a new design of laser (fig.4.4), the raised bonding pads have been dispensed with, removing the bonding pad masking, insulation and metallisation stages. An insulating polyimide layer was formed over the entire substrate, windows were opened to expose the ohmic contacts to laser and output guide, and subsequent gold evaporation then provided a continuous contact to the top of the waveguide, leaving a large area to which wire bonds can be made (fig.4.5). The relatively straightforward process has been shown to be successfull and lasing of the devices has been demonstrated [Jezierski– 11].

4.2. FABRICATION OF THE RIB RING LASER.

4.2.1. Air surrounded rib ring laser fabrication.

A set of three masks (section 3.2.1) was developed to define ring laser devices on heterostructure semiconductor material (fig.4.2) using photolithography [Jezierski– 5]. These were: for bonding pads, for p– type ohmic contacts and for separation grooves of contacts and devices (fig.4.6). "Lift– off" was used to transfer the waveguide design from resist to metal contact pattern (section 3.2). The bonding pads consisted of 30nm of Ti and 200nm of Au deposited on 200nm of SiO_2 insulating layer (section 3.3.3.6). The ohmic contacts consisted of 30nm of Au, 30nm of Zn, 30nm of Au, 100nm of Mo and 200nm of Au (section 3.3), and partly covered the

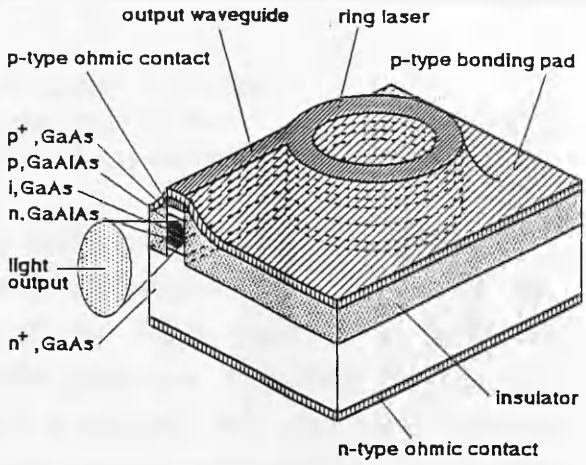

Fig.4.4. Polyimide embedded ring rib laser device.

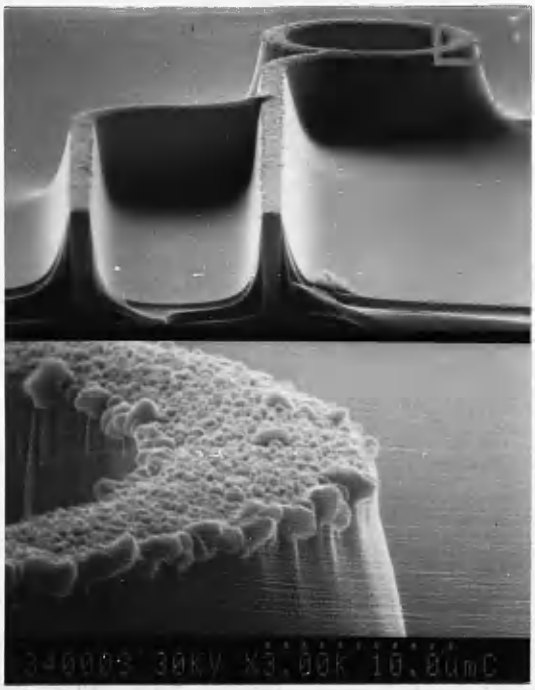

Fig.4.5. Polyimide embedded ring rib laser device produced with electron– beam lithography.

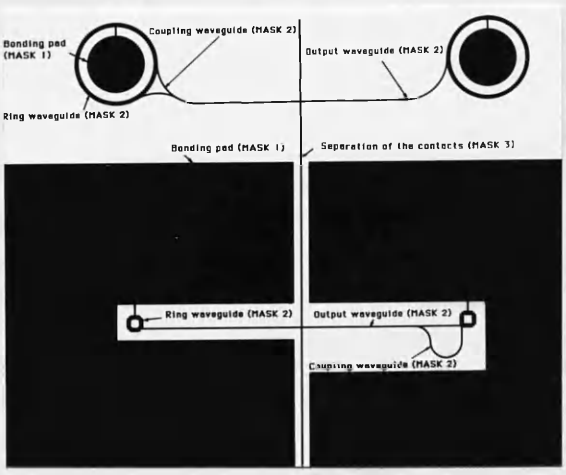

Fig.4.6. Masks and patterns used in ring rib laser fabrication.

bonding pads. Both contacts and bonding pads were covered with 100nm of a protective NiCr layer, which was used as a self–aligning mask for reactive ion etching of the rib ring lasers using $SiCl_4$ (section 3.5.2) (fig.4.7). The NiCr was etched away during the dry etching process (etch rate GaAs/NiCr > 80). The resulting etched wall, up to 7μm deep, had a roughness less than 10nm (figs.4.2) ensuring low optical scattering loss. Separation of the contacts and the devices was performed using a selective Au/GaAs wet chemical etch (section 3.4).

The substrate incorporating the high aspect ratio ring device pattern was lapped from the back down to 100μm thickness (section 3.6) and the n–type ohmic bonding pad was deposited (section 3.3). It consisted of 40nm of Ge, 30nm of Au, 20nm of Ni, 30nm of Au, 100nm of Mo and 200nm of Au. Finally, the sample was annealed in reducing gas for 5sec at a temperature of 400°C (section 3.3.3.4.2) and cleaved into separate devices (section 3.6).

4.2.2. Polyimide embedded rib ring laser fabrication.

The polyimide embedded ring laser eliminated the raised bonding pads of the original air–surrounded structure, thus simplifying its fabrication [Jezierski–11]. The definition of the laser structures involved either photolithography (section 3.2.1) or higher resolution e–beam lithography (section 3.2.2) (fig.4.5), and a "lift–off" method to transfer the waveguide design from resist to ohmic contact pattern. Only one lithographic step was required, followed by some self–aligned steps. The ohmic contact consisted of 30nm of Au, 30nm of Zn, 30nm of Au, 100nm of Mo and 200nm of Au (section 3.3) and was covered with Ni/Cr protective layer, acting as a self–aligned mask for subsequent reactive ion etching using $SiCl_4$ (section 3.5.2). The high quality 6μm deep etched walls promoted low scattering loss of the ring laser devices (fig.4.5).

The etched pattern was covered with a spun polyimide insulator, with the self–aligned depth of 2μm on the bottom of the structure and only 0.15μm deep on the top of the rib (fig.4.5) (section 3.3.2). Oxygen plasma etching (section 3.5.3) removed this thickness of polyimide, exposing the waveguide metallic contact, but continuing to insulate the substrate and the walls of the etched rib waveguide (approximately 0.1 to 0.2μm thick on the side of the active layer). A final 0.5 μm contact layer of Au was evaporated over the whole structure forming a bonding pad.

The substrate was then lapped, the n–type ohmic bonding pad was deposited, the

sample was annealed and cleaved into separate devices, as presented in section 4.2.1.

4.3. EXPERIMENTAL RESULTS AND DISCUSSION OF THE AIR SURROUNDED RIB RING LASERS.

Experimental measurement systems were presented in section 2.4.1. The current duty cycle was limited, as explained earlier, by the current–carrying capacity of electrical connections between the bonding pads and the ohmic contact on the rib waveguide structure.

The lasers measured showed hysteresis of the optical power versus current characteristics and maintained high current optical modes at decreased current values of approximately 10mA. At increased currents, changes of the slope of the power versus current characteristics occured due to mode hopping. We have calculated the mode separation in ring waveguides taking account of the dispersive nature of the waveguiding structure [Thompson–12] and have compared the calculated mode spacings (Appendix 1) with experimental measurements.

4.3.1. A 107μm diameter ring laser.

A typically larger laser device tested was a ring of 10μm–wide waveguide with 107μm outside diameter and stress– and gain–induced index step on the inner waveguide boundary [Jezierski–5] (fig.4.8). A 150μm long and 5μm wide output rib waveguide was coupled to the ring by a Y–junction. Above the threshold current of 180mA (4.5kA/cm^2), the laser operated in single–longitudinal–mode at a wavelength of 889.6nm (fig.4.9). At higher currents multimode operation was observed with a longitudinal–mode spacing of 0.56nm. This is comparable with the calculated mode spacing of 0.57nm of the ring structure (Appendix 1), implying ring oscillations and that the output guide merely transfers and amplifies part of the light to the output of the device.

The ring laser exhibited both TE and TM polarisation, unlike a Fabry–Perot laser which supported a dominant TE mode due to its higher reflection coefficient [Reinhart–13, Ikegami–14]. The cleaved output termination has therefore little influence on the lasing action. The far field was represented by a horizontal two–dot pattern of the E_{10} optical mode.

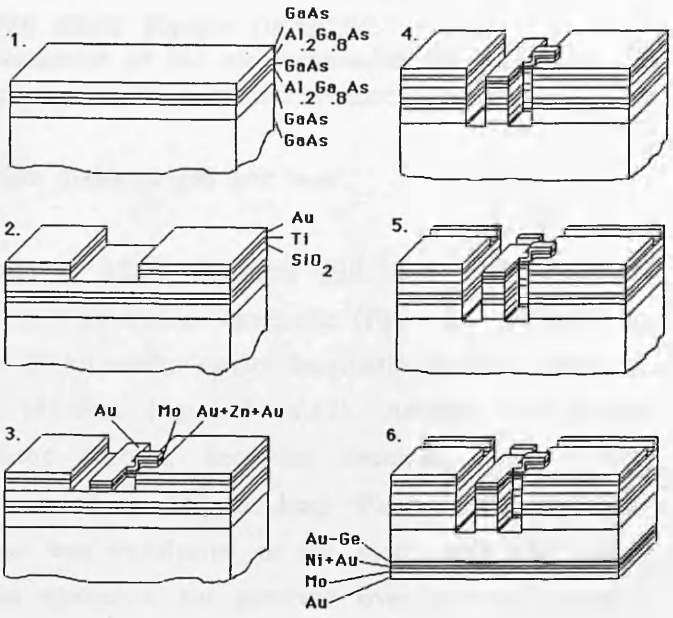

Fig.4.7. Ring rib laser fabrication process steps:
1) Cleaning,
2) Deposition of the bonding pads,
3) Deposition of the p− type contacts for the lasing structure,
4) Etching of the rib laser waveguide structures,
5) Etching − separation of the contacts and devices,
6) Thinning of the substrate and deposition of the n− type contact and the bonding pad.

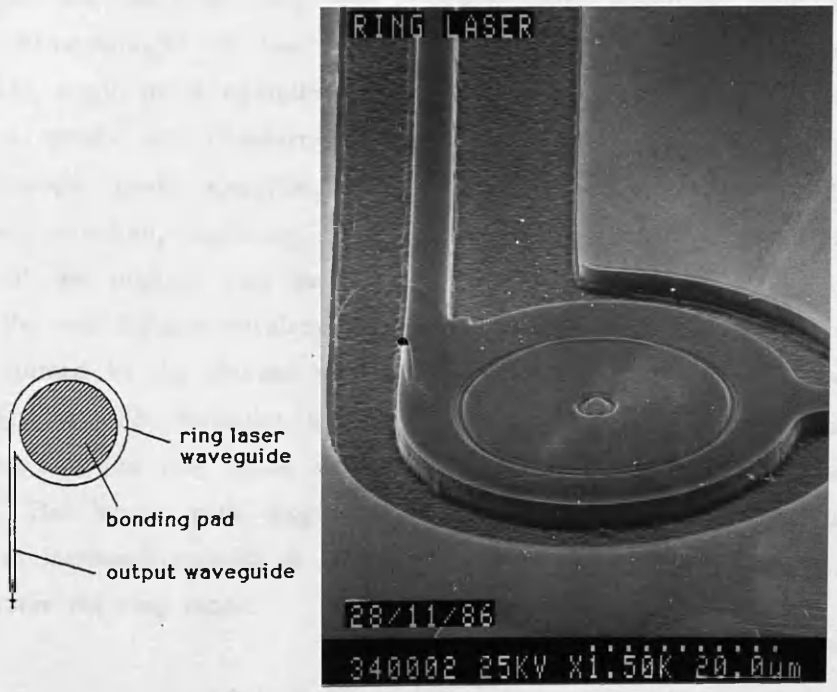

Fig.4.8. A structure consisting of a ring laser of 10μm− wide waveguide with 107μm outside diameter and stress− and gain− induced index step on the inner waveguide boundary and coupled via a Y− junction to a 150μm long and 5μm wide output waveguide. Also, a photograph of a similar structure.

4.3.2. A 12μm diameter pill box laser.

A typical smaller laser device was a 12μm diameter pill box coupled via a Y– junction to a 207μm long by 4μm wide output waveguide (fig.4.10) [Jezierski– 5]. At a threshold current of 200mA (21kA/cm^2), single– longitudinal– mode operation was observed at a wavelength of 888.6nm (figs.4.11, 4.12). Another two modes, 0.46nm apart, appeared at increased current, becoming dominant. The spacing corresponds to the calculated cavity of a 207μm long Fabry– Perot resonator (Appendix 1). Above 240mA, power was transferred to the mode with the longest wavelength and almost– single– mode operation was observed over a large range of currents.

The above laser device measured after having a partly scratched pill– box (fig.4.10) stopped lasing (fig.4.11), still producing large optical luminescence with a 22nm wide spectral half– width. The spectral peak shifted from 882nm to 877nm at increased current from 160mA to 420mA.

The pill– box laser structure was compared with a 270μm long and 4μm wide Fabry– Perot straight rib laser. Above the threshold current of 220mA (20kA/cm^2) (fig.4.11), single mode operation was observed at a wavelength of 889nm. At higher currents, power was transferred into a second mode, which became dominant in almost– single– mode operation. The spectrum was similar to that of the complete ring laser structure, neglecting the first mode at 888.6nm of the ring laser. The first mode of the original ring structure may have corresponded to a ring resonance, while the two longer– wavelength modes may have been modes of a Fabry– Perot cavity formed by the cleaved end of the output waveguide and the wall of the pill box (fig.4.10). The reflection losses in the Fabry– Perot path are larger than around the ring and the ring mode appeared at a lower threshold than the Fabry– Perot modes. The longer path length of the Fabry– Perot cavity provides higher gain, which at increased currents is sufficient to overcome its cavity losses and eventually to overtake the ring mode.

4.3.3. A 23μm wide octagonal ring laser.

A typical octagonally shaped laser structure was a square ring of 8μm– wide waveguide with 23μm sides with the corners cut off at 45^o to form reflecting facets (fig.4.13) [Jezierski– 5]. Two coupling waveguides 4μm wide were connected to the ring in opposite directions via Y– junctions and were joined together via another

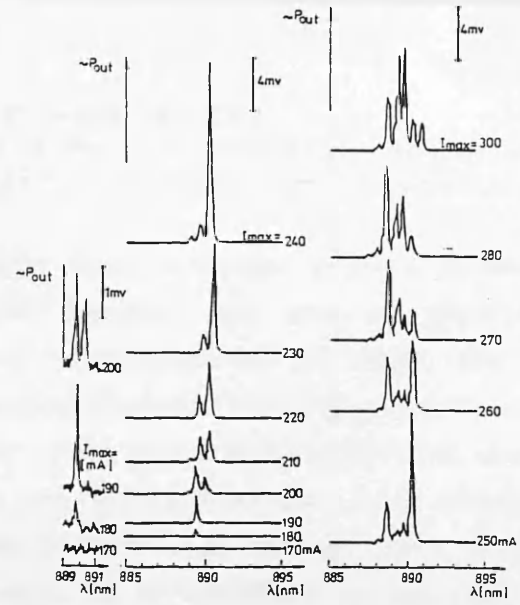

Fig.4.9. Spectra of the ring laser of fig.4.8.

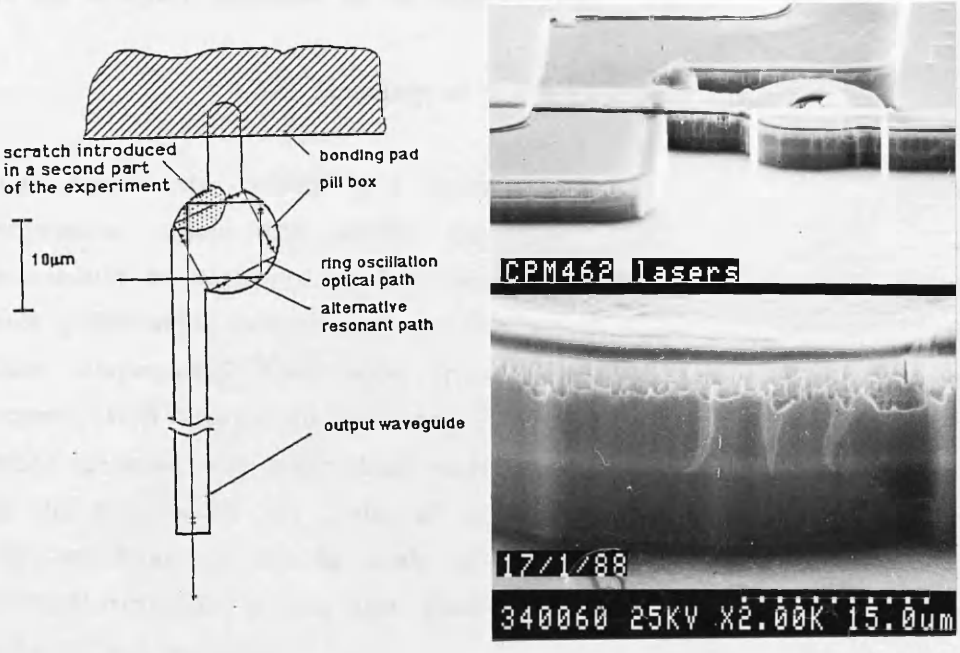

Fig.4.10. A structure consisting of a 12μm diameter pill– box coupled via a Y– junction to a 207μm long by 4μm wide output waveguide and connected to a bonding pad. Also, a photograph of a similar structure.

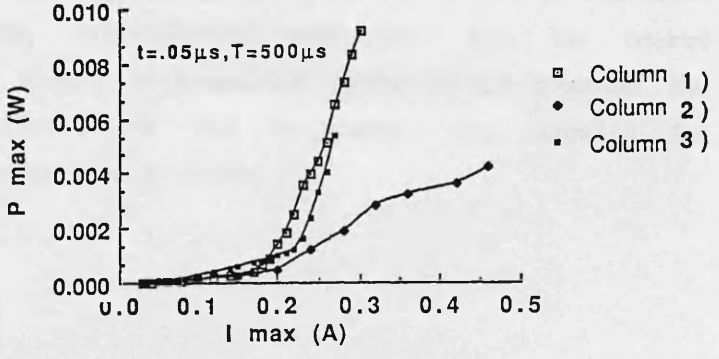

Fig.4.11. Output optical power versus current characteristics of:
1) non– scratched 12μm diameter pill– box structure of fig.4.10,
2) structure of fig.4.10 witha partly scratched pill box,
3) 270μm long by 4μm wide straight rib Fabry– Perot laser.

Y– junction to the 50μm long and 4μm wide output waveguide. Above a threshold current of 120mA (9kA/cm^2), multimode operation was observed (fig.4.14). Multimode operation may have consisted of superimposed sets of modes, due to several distinct optical paths within the resonator (fig.4.13): two contra– rotating ring optical paths (each giving mode spacings of 3.1nm) and a Fabry– Perot– like closed optical path around the ring and along the two coupling waveguides, using reflection at the termination of the output waveguide (0.72nm mode spacing). Some of the spectral lines were fitted to these mode spacings, but correspondence was not clear.

The far field of the device was represented by a single dot pattern of a fundamental transverse optical mode. Some of the similar structures did not couple the light out of the octagonal resonator to the output guides.

4.3.4. Summary of the air surrounded ring lasers.

The experimental results have shown that GaAs/AlGaAs heterostructure ring rib waveguides, either with smooth bends or with reflecting facets, may be used successfully as resonators for laser structures [Jezierski– 5]. Lasing has been observed with pulsed drive current and was comparable to that of the straight Fabry– Perot laser. Single– longitudinal– mode operation has been observed above the threshold current. With substantially increasing current the power is transferred into a multiple mode spectrum, with longitudinal mode spacing corresponding to calculated resonances in the ring, within the limits of experimental accuracy. Rings of 12μm diameter pill– box form can also be made to lase, with the lasing mode controlled by the resonant structure, proving that bending and reflection losses around such a small pill– box are negligible.

The lasers exhibit both TE and TM polarisation, unlike the cleaved cavity lasers, implying that the cleaved output termination has little influence on the lasing action. Some of the structures exhibit additional lasing resonances attributable to alternative Fabry–Perot– like optical paths, unintentionally incorporated into the devices (figs.4.10, 4.13). To limit the number of longitudinal modes in the spectrum, the output power should be collected via one Y– junction, thus avoiding the superimposed spectra of non– symmetrical structures.

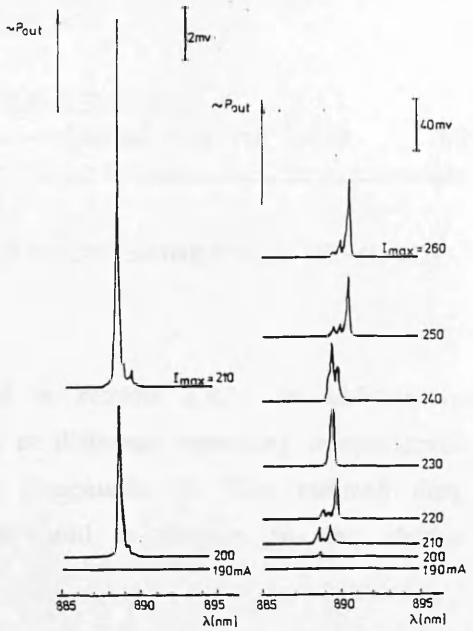

Fig.4.12. Spectra of the non−scratched 12μm diameter pill−box structure of fig.4.10.

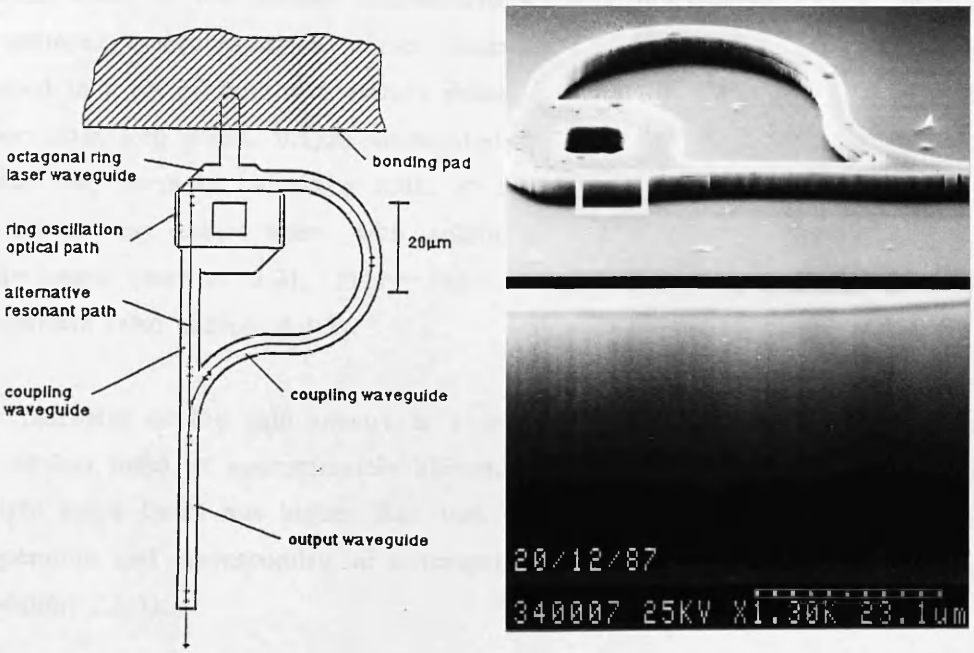

Fig.4.13. A structure consisting of a square ring of 8μm−wide laser waveguide with 23μm sides and corners cut off at 45^{o} to form reflecting facets, with two coupling waveguides 4μm wide connected to the ring in opposite directions via Y−junctions and joined together via another Y−junction to a 50μm long and 4μm wide output waveguide. the structure is connected to a bonding pad. Also, a photograph of a similar structure.

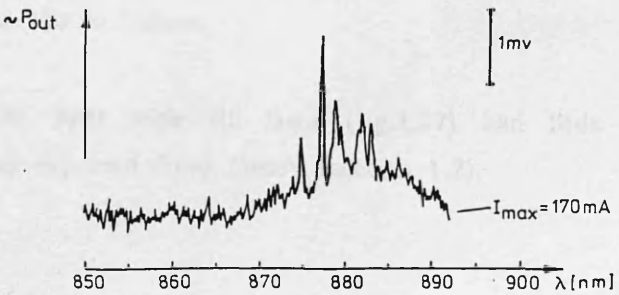

Fig.4.14. Spectrum of the octagonal ring laser of fig.4.13.

4.4. EXPERIMENTAL RESULTS OF THE POLYIMIDE EMBEDDED RING RIB LASERS.

Experimental measurement systems were presented in section 2.4.1. In addition to those, the behaviour of the lasers was investigated at different operating temperatures and at various repetition periods of the current (Appendix 2). The reduced duty cycle resulted in an increase in heat produced and a change in the device characteristics.

4.4.1. Double heterostructure ring lasers.

Devices made of two double heterostructures were investigated. These devices, made of material incorporating a higher index step guide of 0.2μm GaAs/$Al_{.4}Ga_{.6}As$, resulted in a lower threshold current density than the others made of material with a lower index step guide, 0.1μm GaAs/$Al_{.2}Ga_{.8}As$. Table 4.1 presents the performance of the ring lasers in increasing order of threshold current density. Ring laser can be treated as any other laser, with additional losses due to bends and short ring path–length (section 2.2). Fabry–Perot laser results are therefore presented for comparison (also section 2.4.2).

The halfwidth of the gain spectra is 8 to 16nm and above the threshold current all the devices lased at approximately 889nm. The emitted wavelength of both ring and straight stripe lasers was higher than that calculated for the device operating at room temperature and corresponded to a temperature of 70 to 95°C [Chen–15] (Appendix 2, section 2.4.2).

Multiple longitudinal mode operation was observed for broad area devices (section 2.4.2). Both ring and straight stripe lasers resulted in single longitudinal mode operation above the threshold current within the large range of currents and multiple mode operation, at much higher currents (fig.4.15). Very lossy, narrow guide and short–cavity ring lasers (fig.4.16) (sections 1.3, 1.5, 2.2.1) resulted in multiple mode operation and a very weak luminescence. The narrower devices possess luminescence spectra with an additional peak at about 730 to 740nm.

The edge roughness of 0.15μm of the 3μm wide rib laser (fig.4.17) had little influence on threshold current density, as expected from theory (section 1.3).

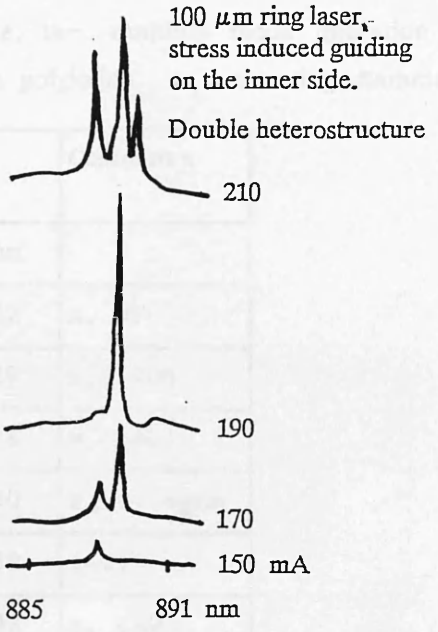

Fig.4.15. Spectra of the polyimide embedded DH ring laser device.

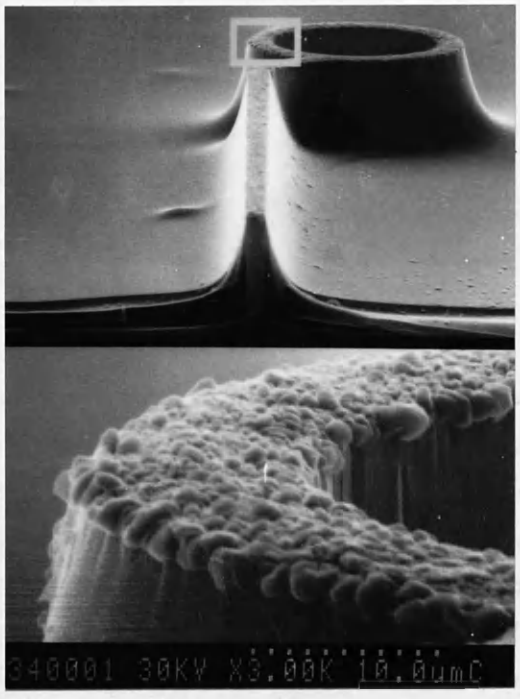

Fig.4.16. Polyimide embedded narrow– guide and short– cavity ring laser.

Table.4.1. Double heterostructure lasers (s – single, m– multiple mode operation, 40 – structure with a smaller index step, NP – no polyimide , Φ is the ring diameter)

guide width	length	output guide	I_{th}	J_{th}	λ	Comments
μm	μm	μm*μm	mA	kA/cm^2	nm	
270	370	-	1700	1.7	882	m, NP
10	Φ107	150*4	180	4.5	889	s, (40)
8	oct4*23	180*4	120	9	878	m, (40)
3	400	-	200	17	880	s, r. egde
4	270	-	220	20	889	(40)
6	pill Φ12	207*4	200	21	889	s, (40)
3	350	-	250	24	890+740, r.edge	
1	330	-	115	34	889+730, m,	
1	320	-	170	53	887	s, (40)
1	400	-	250	62	881	s,
1	Φ20	200*1	420	160	884	m, 1. light
1	Φ12	175*1	450	220	880	m, 1. light
1	up Φ40	did not lase up to 450mA, 1. light (40)				

Both ring and straight rib lasers suffered an increased threshold current density with a decreased width of the guide and with a decreased length of the closed optical path of the resonator, confirming the theory – sections 1.3, 1.5, 2.2.1. The broad area device lased at a threshold density approximately 2kA/cm^2, while a 10μm wide rib forming a 100μm diameter ring lased at 4 to 5kA/cm^2. This increased 4 to 5 times for a pill– box structure of diameter 12μm. Similarly, for 1μm guides, a 12μm ring lased at a threshold density of 220kA/cm^2, approximately 4 to 5 times that of a straight device, 320μm long, comparable to a 100μm diameter ring with a small radiation loss. The increased threshold density corresponds to increased loss due to the reduced length of the laser resonator (sections 1.6, 2.2.1), and increased scattering and absorption of the bent guide. From the results, the threshold current density increased approximately 10 times with the decreased width of the guides from 10 to 1μm. This corresponds to increased scattering and absorption losses of the

increased part of the optical wave, which travels outside the guide. The combination of the 10 times reduced width of the guide and reduced ring diameter from 100μm to 12μm, resulted in a 40 to 50 times increased threshold current. The very lossy small ring devices, with very large threshold current densities emitted very little light and could be easily damaged with excessive currents, even at a very small repetition rate (fig.4.18).

4.4.2. Localized gain region separate confinement quantum well ring lasers.

Two localized gain region material ring lasers were compared: the first with a 22.7nm single well sandwiched between the $Al_{.25}Ga_{.75}As$, and a second with a narrower, 7.6nm single quantum well.

4.4.2.1. Ring lasers made of 22.7nm SQW material.

The operation of the typical ring lasers made of 22.7nm SQW material is presented, in order of increasing threshold current density, in table 4.2. For comparison, straight Fabry Perot lasers are also presented.

Table.4.2. 22.7nm quantum well lasers (s – single mode, m – multiple mode operation, NP – no polyimide, Φ is the ring diameter)

guide width	length	output guide	I_{th}	J_{th}	λ	Comments
μm	μm	μm*μm	mA	kA/cm^2	nm	
300	400	-	750	0.7	858	m, NP
7	Φ100	30*4(+90)	60	2.2	874+868	s,
4	Φ100	350*4	80	3	856	s,
8	rec4*23	320*4	110	6	860+848+844	s,
4	Φ107	100*4	225	12	858	s,
4	Φ40	160*4	150	13		l. light
8	rec4*23	60*4	200	26	871	

Multi– mode operation was observed for broad area devices (section 2.4.3). All the ring and straight stripe lasers lased in single longitudinal mode within a large range

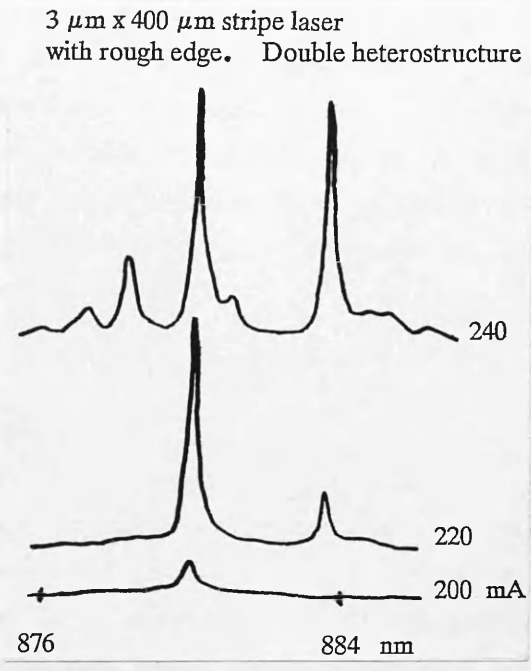

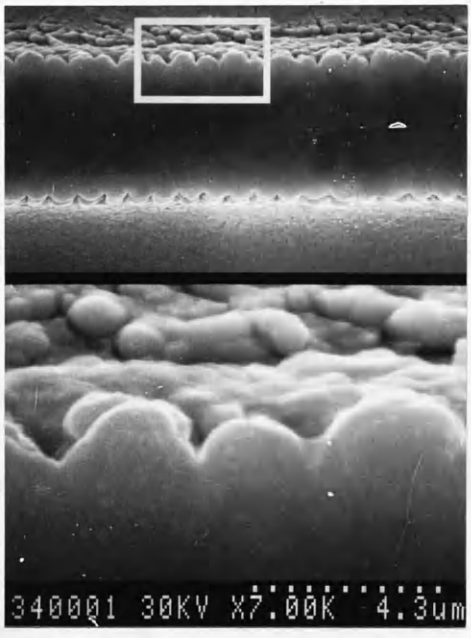

Fig.4.17. The 3 μm wide stripe laser with a roughness of the etched edges of 0.15 μm every 0.5 μm and the spectra of the device.

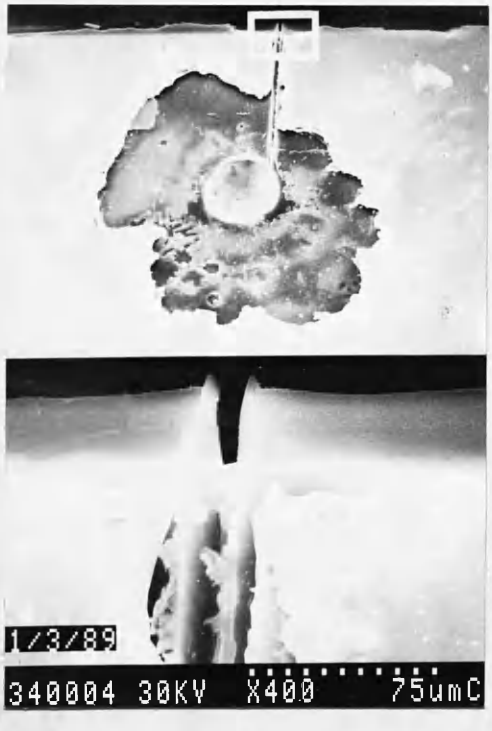

Fig.4.18. Damage to the contact metallisation or the semiconductor material due to high currents.

of the currents, at a wavelength of about 860nm (fig.4.19). This was similar to the calculated wavelength for the devices operating at room temperature (sections 2.3, 2.4.3, Appendix 2). At higher currents, another mode, spaced by 4 to 6nm, appeared. The broad area devices lased at 700A/cm^2, while typical ring lasers of 4μm wide guide, in a 100μm diameter ring operated at current density between 3 and 12kA/cm^2.

4.4.2.2. Ring lasers made of 7.6nm SQW material.

The performance of the lasers made of 7.6nm QW material is presented, in order of increasing threshold current density, in table 4.3. Short ring path, narrow guide and consequently very lossy ring lasers (sections 1.3, 1.5) produced very little light and did not lase (section 2.2.2), although still showing interesting properties. For comparison, straight Fabry– Perot lasers are also presented (also section 2.4.3).

Table.4.3. Lasers made of 7.6nm quantum well material (s – single mode, m – multiple mode operation , Φ is the ring diameter)

guide width	length	I_{th}	J_{th}	λ
μm	μm	mA	kA/cm^2	nm
100	800	220	0.27	844,s
50	300	70	0.46	840,m
50	250	90	0.72	840,m
50	110	370	6.7	840,m
50	100	did not lase,		
1	600	120	20	782,s
1	400	did not lase, peaks at 785 and s. at 835nm		
4	Φ40	did not lase, peaks at 840nm, 726 and 676nm		
1to2	Φ40	did not lase, peaks at 775 and 840nm (also weak at 725 and 680nm), little light		
1to4	Φ10	did not lase, little light,		

With an increased optical loss in the structure, the threshold current density of the devices made of thin well material increased at a much higher rate than in the case

of double heterostructures. This was critical for narrow guides, sharp bends and also for short lengths of the structures, preventing lasing action (Section 2.2). Low loss devices lased at 840nm (fig.4.20). With increased loss of the narrow guides, a single longitudinal mode in the second quantised state operation at 782nm was observed [Jezierski–11] (section 2.2.4). The ring lasers which introduce excessive losses could not be made to lase and emitted very little light. They produced spectra with peaks at 840nm and 775nm, coresponding to both first and second quantised state operation. The first dominated at low and the second at higher currents (fig.4.20) [Jezierski–11] (section 4.4.4). Similar changes were observed at the increased current duty cycle; the first peak dominated at low and the second at high repetition rates (fig.4.21).

4.4.3. Discussion of the polyimide embedded ring lasers.

Ring lasers can be treated as any other laser with additional losses due to bends, Y–junction and short–cavity–length. Guides narrower than 4μm result in a considerable part of the optical field travelling outside the guide, particularly for higher order modes (section 1.3). This increases not only with reduced guide width but also is aggravated by the bends, where the field is pulled outside the bent guide (section 1.6.1). The spread of the field outside the guide is susceptible to loss, particularly in embedded structures (fig.4.5), where the spread for the narrow guides is significant, while polyimide on the sides of the guide is of thickness 0.1 to 0.2μm only, and is coated with a high–loss gold bonding layer (section 4.2.2). The loss of the ring laser structure may be enhanced by the guide wall damage and imperfection (sections 3.2, 3.5.2) and the coupling loss at a Y–junction (section 1.7).

The high loss of waveguide structures contributes to the high threshold current density of the ring laser devices (sections 2.2). In the DH, the threshold current density increases almost proportionally to the increased loss (sections 2.2.1, 2.2.3). This is aggravated in the QW structures due to the almost exponential dependence of current on losses (sections 2.2.2, 2.2.3). This dependence was confirmed with experimental results using a variety of both ring and straight lasers, with varying widths and lengths of guides. Narrow–guide and short–cavity stripe lasers, particularly in ring configuration, aggravated the guide loss and increased the threshold current density.

For the lasers made from double heterostructure material, the loss and the threshold current density increased 4 to 5 times with the decreased ring diameter from 100μm

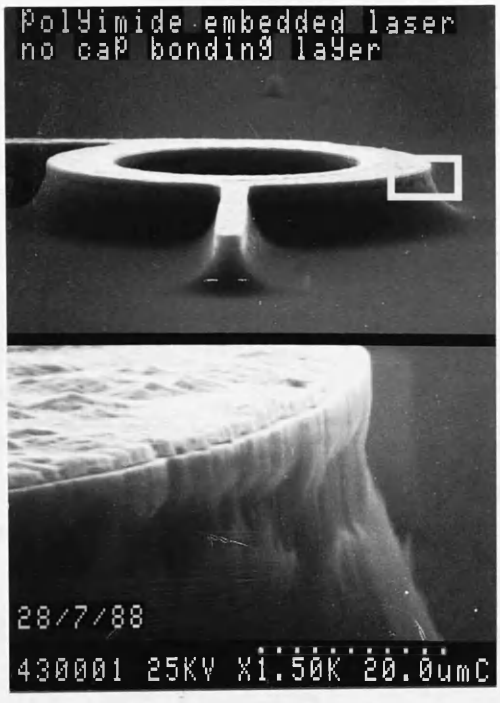

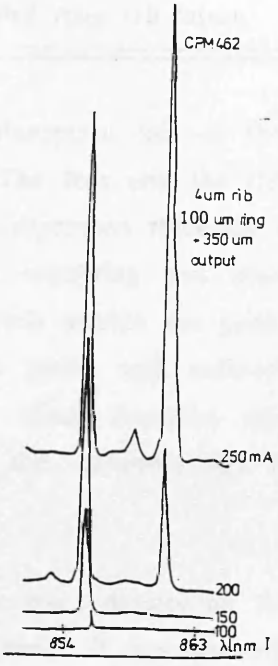

Fig.4.19. Spectra of a polyimide embedded structure incorporating a 4μm wide rib of 100μm diameter ring laser with 350μm long output guide, incorporating a 22.7nm thick single quantum well. Also, a photograph of a similar structure.

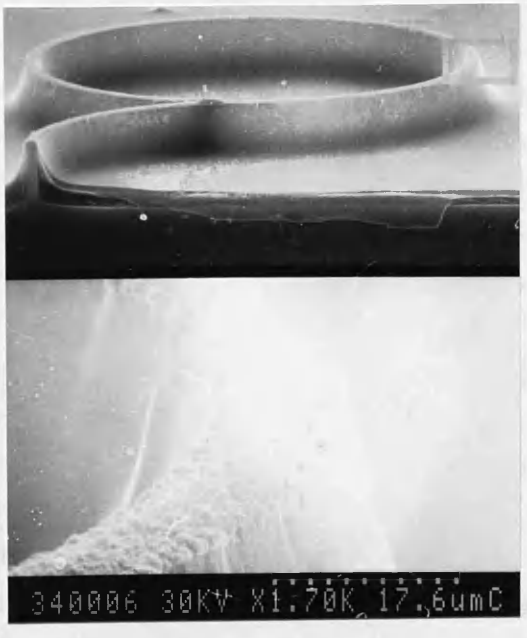

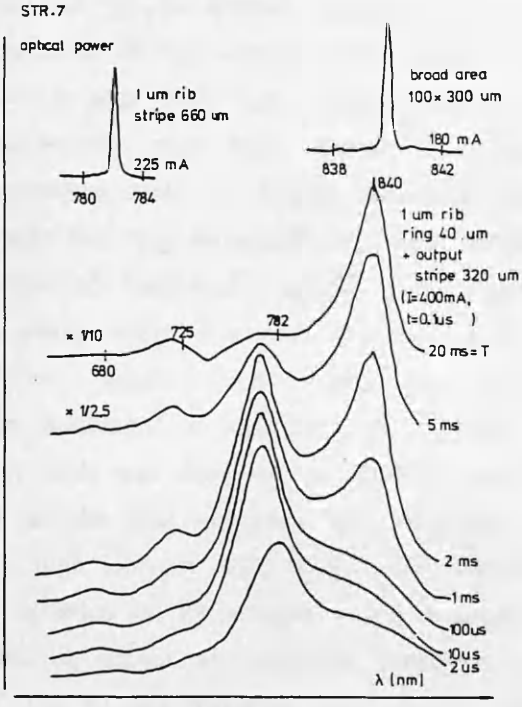

Fig.4.20. Spectra of the lasers made of 7.6nm SQW material:
1. broad area, 2. narrow stripe polyimide embedded rib, 3. 1μm rib 40μm diameter ring laser embedded in polyimide. Also, a photograph of a similar structure.

to 12μm. This corresponds to increased scattering and absorption loss of the bent guide, as well as reduced length of the laser resonator. The loss and the threshold current density increased approximately 10 times with the decreased thickness of the guides from 10 to 1μm. This corresponds to increased scattering and absorption losses of an increasing part of the optical wave, which travels outside the guide. The combination of the 10 times reduced thickness of the guide and reduced ring diameter from 100μm to 12μm, resulted in 40 to 50 times increased threshold density. This ring laser, operating at 220kA/cm^2, indicated the extremely high loss of the narrow guide.

Considering the exponential dependence of the threshold current density on the loss within lasers made of narrow quantum well material (<15nm), it was not suprising to find that very lossy, narrow–guide and short–path ring lasers made of 7.6nm SQW material did not operate successfully. A narrow, 1 μm wide, rib laser required a very long, 1200μm closed–path for the lasing action. The laser operated at a wavelength of 782nm, shifted from that calculated for the first quantised state and experimentally proved for broad area devices to be 840nm, sections 2.3, 2.4, 4.4.2.2). This wavelength shift is further evidence of high optical losses, since it has been suggested that in a single quantum well laser with high cavity losses, where lasing threshold current densities are necessarily very high, there is a major contribution to gain from the second quantised state at largely increased lasing photon energy (section 2.2.4). Extremely high–loss ring waveguide structures made in 7.6nm SQW material, while not lasing, exhibited luminescent spectra with peaks at wavelengths of 840 and 775nm. The first peak, corresponding to the first quantised state operation, dominated at lower drive current levels while the second, corresponding to the second quantised state, dominated at high drive levels and high temperature operation. No such wavelength shift was observed in devices made in DH material. In addition, the dominance of the first quantised state operation at low, and the second quantised state at high current duty cycle was observed (fig.4.21). This might have been due to a variation in temperature which depends on the duty cycle, since the temperature will be higher at increased repetition rate (Appendix 2). The luminescent spectra of the 40 μm diameter ring laser structure (fig.4.20) showed a remarkable similarity to the theoretical gain spectra of Mittelstein et al.(29) of second quantised state gain in a single quantum well short cavity laser (fig.4.22) (section 2.2.4).

The lasing threshold current of the lossy guide made of 22.7nm wide SQW material, is greatly reduced compared to that of narrow well material (section 2.2.2), and the

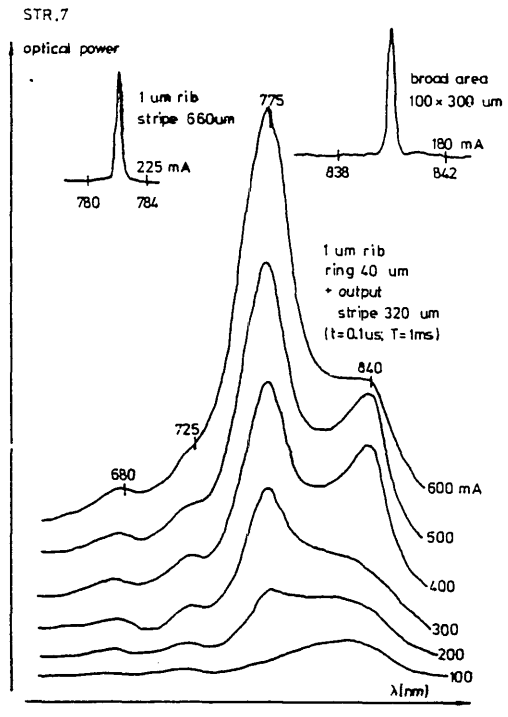

Fig.4.21. Spectra of the 1 μm rib 40μm diameter ring laser embedded in polyimide, made of 7.6nm SQW material. Spectra was observed at increased current duty cycle.

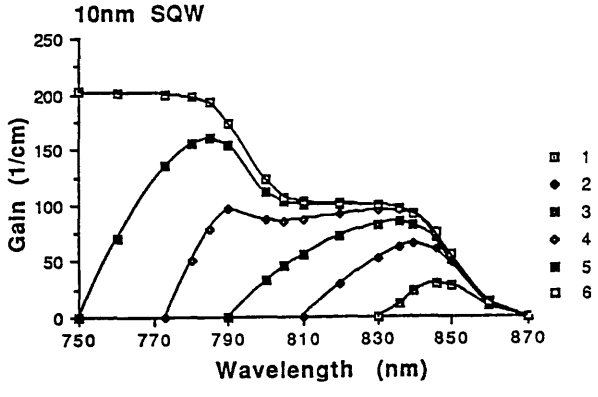

Fig.4.22. Theoretical gain spectra of a single quantum well short cavity laser (After Mittelstein– 29).

practical ring lasers of this material, operated succesfully.

For all the laser materials, low loss and consequently acceptable low threshold current densities may be provided by using wider guides and larger diameter ring structures, low–loss medium surrounding the guide and low scattering loss of the guide surface. The factors have been presented already in section 1.5, 1.8, 1.9, 2.2 and will be mentioned in section 5.

4.5. REFERENCES.

[1] Merz,J.: Monolithic integration of optical sources and detectors, Proc. SPIE, Vol.239, pp.53–60 (1980).

[2] Matsumoto,N., Kawaguchi,H., Kumabe,K.: Oscillation characteristics of semiconductor lasers with circular waveguides, Proc. IOOC'77, Vol.B1.2, pp.189–192 (1977).

[3] Liao,A.H., Wang,S.: Semiconductor injection lasers with a circular resonator, Appl.Phys.Lett., Vol.36, pp.801–803 (1980)

[4] Wang,S., Choi,H.K., Fattah,I.H.A.: Studies of semiconductor lasers of the interferemetric and ring types, IEEE J.Q.E.–18, pp.610–617 (1982).

[5] Jezierski A.F, Laybourn P.J.R.: Integrated semiconductor ring lasers, IEE Proc., Vol.135, Pt.J (1) pp.17–24 (1988).

[6] Austin,M.W.: GaAs/GaAlAs curved rib waveguides, IEEE J.Q.E.–18, pp.795–800 (1982).

[7] Marcatilli,E.A.J.: Bends in optical dielectric guides, BSTJ, Vol.48, pp.2103–2132 (1969).

[8] Walker,R.G., Wilkinson,C.D.W.: Integrated optical ring resonators made by silver ion–exchange in glass, Appl.Optics, Vol.22, pp.1029–1035 (1983).

[9] Walker,R.G., Wilkinson,C.D.W.: Integrated optical waveguiding structures made by silver ion–exchange in glass.2: Directional coupler and bends, Appl.Optics, Vol.22, pp.1929–1936 (1983).

[10] Jezierski A.: Integrated semiconductor GaAlAs laser device technologies, report, Glasgow University (1985).

[11] Jezierski, A.F. Laybourn, P.J.R.: Polyimide–embedded semiconductor ring lasers, 5th European Conference on Integrated Optics, Paris, Paper no.3 (1989). Published in proceedings of SPIE, 1141, 7–11 (1989).

[12] Thompson G.H.B.: Physics of semiconductor laser devices, J.Wiley & Sons, (1980).

[13] Reinhart F.K., Hayashi I., Panish M.B.: Mode reflectivity and waveguide properties of double heterostructure injection lasers, J.Appl.Phys., Vol.42, pp.4466–4479 (1971).

[14] Ikegami T.: Reflectivity of mode at facet and oscillation mode in double heterostructure injection lasers, IEEE J.Q.E–8, pp.470–476 (1972).

[15] Chen, W., Laybourn, P.J.R., Jezierski, A.F. and Webb, P.W.: Thermal characteristics of semiconductor ring laser sources for integrated optical sensor devices, Arditty H.J., Dakin J.P. & Kersten R.Th. (Eds.): Optical Fibre Sensors, Springer proceedings in Physics, 44, pp.302–312, Heidelberg: Springer (1989). (Proceedings of 6th Optical Sensors Conference, Paris, (1989)).

5. CONCLUSIONS.

Ring waveguide and pill– box laser structures down to 12μm in diameter with a Y– junction branching output guide, were investigated and successfully produced. This type of structure is suitable for use as a light source in monolithic integrated optics.

Optical properties of the component structures: slab guide, straight stripe guide, curved guide, and both directional and Y– junction guide couplers, were analysed using finite difference and other methods. Most of the losses within the optical waveguides considered could be reduced substantially by using low– loss media, strong confinement and wider guides, to reduce a proportion of the decaying field travelling outside the guide. A rib configuration was proposed to maximise light confinement and to minimise bending loss at small cavity circumferences. The resonator with Y– junction output guide requires the ring guide to be wider than the output guide for constructive oscillation of the extractable optical wave.

The threshold current increases with loss of the laser guides. The threshold conditions of guides made of a double heterostructure, localised gain region quantum well structure and a structure with additional passive guide coupled to the lasing layer were discussed and compared with experimental results of the broad area and the narrow stripe devices. The standard broad area lasers operated at relatively low threshold current densities of 0.4kA/cm^2 for a 7.6nm thick QW, 0.7kA/cm^2 for a 22.7nm thick QW and 1.7kA/cm^2 for a 0.2μm thick region of a double heterostructure. The broad area devices made of a material incorporating an additional passive guide lased at an increased threshold current density of 1.8kA/cm^2 and in single mode, due to restricted oscillation conditions, while other structures oscillated in multimode.

The original rib ring laser waveguides were defined in GaAs/AlGaAs heterostructure materials by reactive ion etching, through the pattern of metal ohmic contacts connected to the bonding pads. The fabrication was then simplified by embedding the etched rib guide structures in polyimide and overcoating with a gold bonding layer. Good quality curved patterns down to 0.4μm were produced using photo– and e– beam lithography. Ohmic contacts were designed that were capable of operation at 350^{o}C, and improved the reliability of the final devices. The investigations into the contacts were supported with a specially developed controlled annealer. Wet and highly anisotropic dry etching were used extensively throughout the device fabrication

to selectively remove various parts of the material and to produce high aspect ratio, low damage, smooth surface ring laser rib patterns down to 0.4μm wide, 7μm deep and up to 400μm long. Separation and packaging of the fragile ring laser pattern devices completed the fabrication.

The performance of the rib ring laser structures was comparable to those of straight lasers of similar size. The lasers made of 0.2μm thick double heterostructure operated at 882nm. Those with a reduced active layer thickness of 22.7nm operated at 860nm while those with 7.6nm QW lased at 840nm. Single mode operation was frequently observed and the lowest threshold current achieved was 60mA. Losses and threshold current densities of the devices increased with a reduced width of the rib guide below 3 to 4μm, where a considerable part of the light spread outside the guide, and was affected by the scattering loss on the guide boundary and the absorption loss of the outside media. (Polyimide covering the sides of the structure was only 0.1μm thick and was covered with a highly absorbing gold layer.) The threshold current density also increased with the reduced length of the laser cavity. This affected strongly confined small rib ring guides, even though they should produce acceptable radiation loss.

The dependence of the threshold current density on loss is almost linear for lasers made of double heterostructure and almost exponential for devices made of quantum well structure material. Very lossy DH devices of 1μm narrow guide and short cavities of 12μm diameter, were lasing, although at a threshold density increased from 1.7 to 220kA/cm^2. Similar structures made in QW material did not operate. The advantage of the QW lasers of providing lower threshold curent density than the DH lasers applies therefore to low loss devices only (0.4kA/cm^2). Second quantised state operation was observed for high-loss QW lasers, and peaks of the spectra related to both first and second quantised state operation were visible for excessively lossy, non-lasing QW devices; the first dominated at low, and the second at high currents.

In conclusion, the work has shown that ring waveguide semiconductor laser structures can be fabricated in a straightforward way with relatively few process steps. They can be created at any position on the semiconductor substrate and their processing is compatible with that of other optical devices built on the same monolithic integrated optical circuit chip. Devices were demonstrated with threshold currents down to 60mA and single mode operation was frequently present. It was shown that the ring

lasers can be treated as other standard straight lasers, where the waveguide losses determine their threshold current density, which increased with reduced length of the closed optical path and reduced width of the guides, particularly for quantum well devices. An interesting observation was demonstrated of gain at second quantised state in high loss quantum well devices. Losses within the laser structures should be minimised to avoid excessive threshold currents in the devices and subsequent heat sinking problems.

6. PROPOSED FUTURE WORK.

The investigations proved that a Fabry–Perot laser may be successfully replaced with a ring resonator structure with a Y–junction branching output guide. Some improvements into the design are essential.

Material and pattern configuration improvements and heat sinking will be required for CW operation. Because lasing of the double heterostructure occurs near the absorption edge of GaAs, the output waveguide had to be pumped to reduce its large absorption loss; the use of a single quantum well increases the loss of the short cavity lasers; a multiple quantum well structure will be needed to render pumping of the passive circuitry unnecessary. The single quantum well material used introduced excessive loss and threshold current density for short–cavity ring lasers. Increasing the number or width of wells is necessary to avoid the problems. The spread of the field away from the waveguide, the loss of the rib laser guides and high threshold current density can be considerably reduced by producing guides wider than 4μm, or even pill–box–type structure , and reducing the coupling to the output guide by producing a ring laser guide wider than the output guide. The reduction of the output coupling may be also achieved by the alternative output coupling scheme involving a lower passive waveguide investigated in section 2.1.3. The optical field spreading outside the guide should be enclosed within low–loss media and a much thicker layer of polyimide (or regrown AlGaAs) should therefore cover the sides of the rib guide than that used in the present structures. The process may be eased by reducing the height of the rib, which in addition would improve heat sinking. An alternative solution to the optimisation of performance of a short–cavity ring laser is to design longer guide ring lasers, with the length optimised from other parameters of the device

The frequency stability of the output optical power of the devices produced requires a stable temperature of operation. The usual techniques of temperature stabilisation and drive current control can be used. The configuration of the rib ring laser device enables introduction of a separately pumped output guide or a part of the ring with the help of additional electrodes. The first structure may produce very short optical pulses. With a properly chosen phase shift between "on"–time of the waveguide (which is "off" until the laser is building up) and "off" time of the laser, stimulated emission within the active layer could start immediately, without a time delay in photon creation, due to the life time of electrons. The second device introduces

tunable attenuation of the gain into the ring (and a controlled refractive index change) to introduce a phase change to lock the chosen mode of the laser. Fine tuning of the resonant cavity frequencies and hence laser output may be achieved by current injection or electro–optic phase shifting. Modifying the structure, two separately tuned coupled rings may be used to increase control over the mode selection. In addition, transverse mode selection within the ring structures will occur, because of differential bending losses between the modes, so that a very narrow output spectrum may result. In this work only a basic ring laser configuration was discussed.

Future work, proposed above, may lead to the commercial application of the ring laser in monolithic integrated optical circuits.

APPENDIX 1. LONGITUDINAL SPACING OF THE LASER SPECTRAL LINES.

At current approaching the threshold, the spontaneous emission spectrum transforms into the peaks of stimulated emission corresponding to preferential optical modes with an integral number of wavelengths within the closed optical cavity [Thompson−1]. The optical resonant conditions must match the available eigen states of the semiconductor and the resulting lasing spectra may indicate the domination of chosen optical modes with discrimination against the other intermediate modes.

The longitudinal spacing $\delta\lambda$ between subsequent optical modes at wavelengths around λ_0 (fig.A.1.1) , relates to the number of wavelengths that can be accommodated within the closed optical cavity of length L, giving:

$$\delta\lambda = \frac{\lambda_o^2}{L*n_e} \qquad (A.1.1)$$

The effective refractive index n_e of the guide is a normalised average value of the effective indexes within the active n_{ea} and cladding n_{ec} layers:

$$n_e = \frac{d*n_{ea} + s*n_{ec}}{d+s} \qquad (A.1.2)$$

where: d and s are thickness of the active layer and the spread of the light in the cladding layer, dependent on the chosen structure and the normalised effective optical width S (derived from the normalised thickness of the active layer D [Thompson−1],

e.g. for D=1.7 s=0.4*d, while for D=1.4 s=d.

The effective refractive index of the active or cladding layers is:

$$n_{ea,c} = n_{a,c}(\lambda_o) - \lambda_o * \frac{\delta n_{a,c}(\lambda_o)}{\delta\lambda} \qquad (A.1.3)$$

where: $n_{a,c}$ is the refractive index of the active or cladding layer (section 2.3.2). Hence, the derivative of the refractive index of the $Al_xGa_{1-x}As$ material (section 2.3.2) can be calculated as:

$$\frac{\delta n_{a,c}(\lambda_o)}{\delta\lambda} = \frac{\lambda_o}{n(\lambda_o)} * \left\{ \frac{-0.97501}{[\lambda_o^2-(0.52886-0.735*x)^2]^2} - 0.002467*(1.41*x+1) \right\}$$

for $x \leqslant 0.36$,

$$= \frac{\lambda_o}{n(\lambda_o)} * \left\{ \frac{-0.97501}{[\lambda_o^2-(0.30386-0.105*x)^2]^2} - 0.002467*(1.41*x+1) \right\}$$

for $x > 0.36$, (A.1.4)

e.g. at 297K, for GaAs with n=3.6, n_{ea}=4.5, while for $Al_{.25}Ga_{.75}As$ with n=3.45, n_{ec}=4.0.
Then for D=1.4, n_e=4.25.
Subsequently at λ_o=0.868μm and L=800μm this will result in $\delta\lambda$=0.222nm. The value increases by a factor of ten with a similar decrease in length. Note that the lasing conditions may be very restricted for very short path lasers.

The calculated longitudinal spacing between the subsequent spectral peaks was in agreement with experimental results (sections 4.3, 4.4).

APPENDIX 2. TEMPERATURE PROPERTIES OF THE RING LASER DEVICES.

The threshold current of a ring laser is determined by temperature dependent factors, i.e. losses, gain, quantum efficiency and the structure configuration (fig.A.2.1) (sections 2.2.1, 2.2.2). The performance of practical lasers is evaluated with an approximate equation, assuming a temperature step of at least 60°C:

$$J_{thr}(T) = J_{thro} * \exp(\frac{T}{T_o}) \qquad (A.2.1)$$

$$T_o = \frac{T_1 - T_2}{\ln[\frac{J_{thr}(T_1)}{J_{thr}(T_2)}]} \qquad (A.2.2)$$

where: J_{thro} is a constant,

T is an absolute temperature,

T_o is a structure dependent parameter, increasing with temperature [Chinn– 2].

There is no available useful model of the process. The practical DH lasers result in a T_o of 120 to 220K, while the QW structures exhibit smaller temperature dependence ($T_o \approx$250 to 300K), increasing with cavity length and number of wells [Chinn-2].

The experimental DH devices resulted in a linear dependence of the threshold current on the temperature, with a shift in the emitted wavelength of approximately 0.26 to 0.3nm/°C (fig.A.2.2).

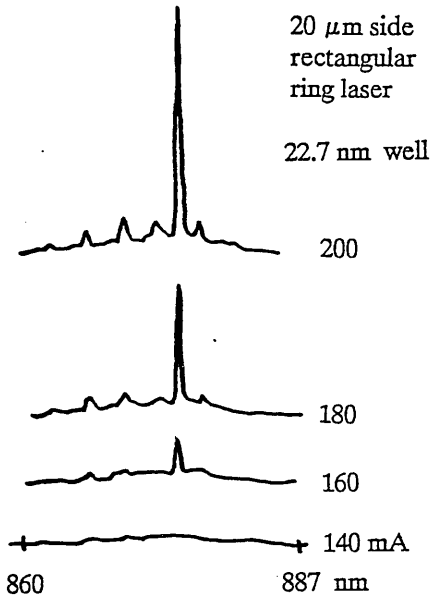

Fig.A.1.1. Spectra of the practical laser.

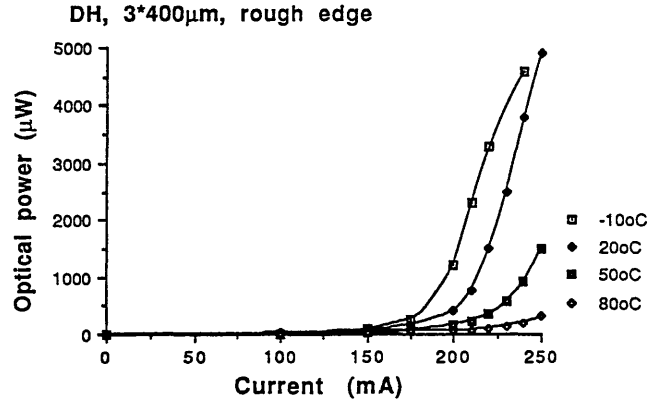

Fig.A.2.1. Optical power versus current characteristics at different temperatures.

Appendix 2.1. Temperature distribution within the ring laser.

Heat is transferred from the hotter to cooler regions of the solid laser device by conduction and at a much slower rate, by convection and radiation [3]. Peltier cooling devices are therefore often used to pump the heat away from the device.

The conduction, q, is proportional to the temperature gradient ΔT across the distance ΔX and the area of the transfer A, with a thermal conduction constant k:

$$q = -k*A*\frac{\delta T}{\delta X} \qquad (A.2.3)$$

At a steady state, the rate of heat generation q^* per unit time and unit volume, and the conduction rate per unit volume within the distance ΔX and ΔY, is equal to zero [Nakwaski– 3]:

$$q^* + \frac{\delta}{\delta X}\left(k * \frac{\delta T}{\delta X}\right) + \frac{\delta}{\delta Y}\left(k * \frac{\delta T}{\delta Y}\right) = 0 \qquad (A.2.4)$$

where: k is a thermal conduction coefficient, usually constant within the volume being considered.

In cylindrical coordinates the equation takes the form:

$$\frac{\delta^2 T}{\delta r^2} + \frac{1}{r} * \frac{\delta T}{\delta r} + \frac{\delta^2 T}{\delta z^2} + \frac{q^*}{k} = 0 \qquad (A.2.5)$$

The temperature distribution may be calculated numerically. A finite difference method (section 1.3) replaces the derivatives of the heat distribution equation with relations at the discrete mesh points, where the discrete values at each point depend on the values of the neighbouring points. The subsequently improved approximations of the field are calculated until the error reaches the tolerable value. The finite difference expression for most of the mesh points of a steady state rectangular (A.2.6) or cylindrical (A.2.7) system are respectively:

$$T_{i,j} = \left(\frac{T_{i+1,j}+T_{i-1,j}}{\Delta X^2} + \frac{T_{i,j+1}+T_{i,j-1}}{\Delta Y^2} + \frac{q^*}{k}\right) * \frac{1}{\frac{2}{\Delta X^2}+\frac{2}{\Delta Y^2}} \qquad (A.2.6)$$

$$T_{i,j} = 1/4*\left(T_{i,j-1}+T_{i,j+1}+T_{i-1,j}*\left[1-\frac{1}{2*i}\right]+T_{i+1,j}*\left[1+\frac{1}{2*i}\right]+q^*_{i,j}*\frac{\Delta X^2}{k}\right) \qquad (A.2.7)$$

The temperature of the laser junction, where the heat is created depends on the configuration of the device and is higher than that of the heat sink (fig.A.2.2). Operation at a reduced repetition rate greatly increases junction temperature and threshold current and shifts the emitted wavelength, thus preventing CW operation

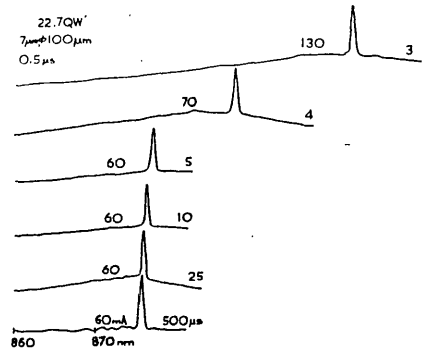

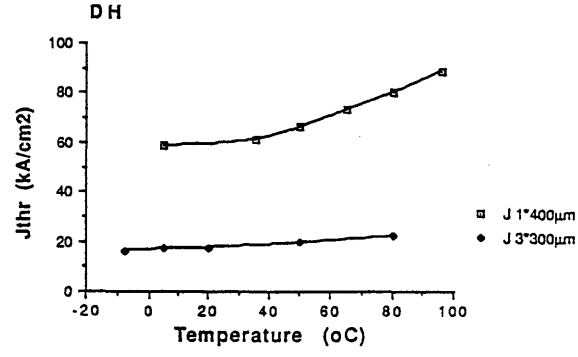

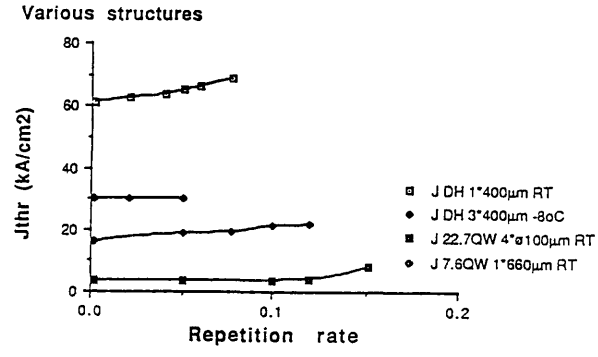

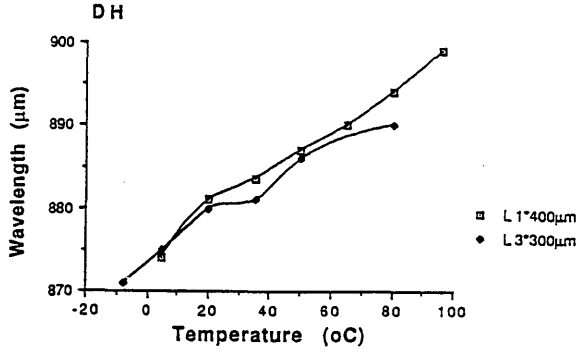

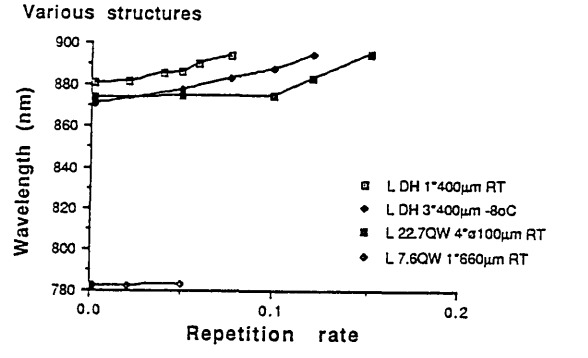

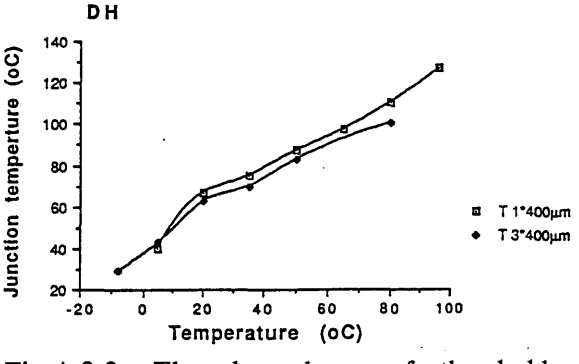

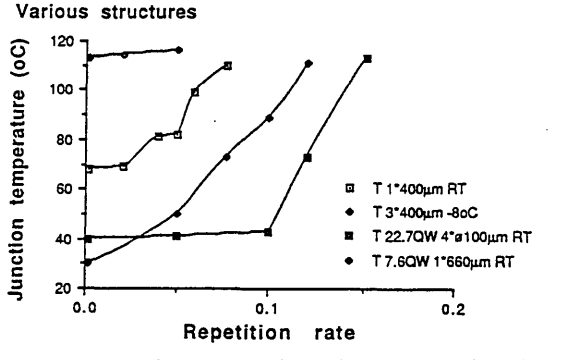

Fig.A.2.2. The dependence of threshold current density, wavelength and related junction temperature on the temperature of the heat sink and on the repetition rate of the driving current. Note that the 3*400μm laser (second graph) was kept at -8^{o}C. Note also that the 7.6nm QW laser operated at a second quantised state. The operation at a first quantised state resulted in a much lower threshold current and much lower junction temperature.

(fig.A.2.2). The difference in the temperatures across the sample per unit power P_{input}, determines the thermal resistance R_{th}, which should be smaller than 100°C/W, to avoid thermal problems [Chen– 4]. The equation describing the thermal resistance is not accurate under pulsed operation (fig.A.2.2):

$$R_{th} = \frac{T_{top}-T_{bottom}}{P_{input}} \ [^{o}C/W] \qquad (A.2.8)$$

The temperature distribution across the wafer incorporating a rib pattern (figs.A.2.3, A.2.4) may be obtained by superimposition of separate temperature fields across the substrate and the rib [Chen– 4, 5].

The temperature drop across the substrate increases with input power and reduces with the dimensions of the pattern as:

$$\Delta T_s \approx \frac{A_s * P_{input}}{\text{rib area}} \ [W/\mu m^2] \qquad (A.2.9)$$

where: A_s is a temperature coefficient, dependent on the rib width, due to spreading of the temperature field in the rib to match the much wider field of the substrate.

A practical examples of a 100μm thick substrate of the dimensions of 400*400μm, incorporating a ring waveguide rib are presented in table A.2.1. [After Chen– 4].

Table A.2.1. Substrate temperature coefficient A_s.

Rib width (μm)	2	4	8	10
A_s	45400	86200	156000	188000
Examples ΔT_s for 200mW	108°C for Φ12 36°C for Φ40 25°C for Φ60	14°C for Φ100		12.6°C for Φ100

The temperature drop across the rib is proportional to the input power density:

$$\Delta T_r \approx \frac{A_r * P_{input}}{\text{rib area}} \ [W/\mu m^2] \qquad (A.2.10)$$

where the rib temperature parameter A_r is independent of the width of the rib. For a rib height 3μm, the practical examples are presented in table A.2.2. [After Chen– 4].

Table A.2.2. Rib temperature coefficient A_r.

A_r	50000
Examples ΔT_r for 200mW	16°C for 2μm guide, Φ100μm 3.5°C for 10μm guide, Φ100μm

The calculations were compared with the observation of luminescence (0.6 to 0.9μm) using an IR viewer (fig.A.2.5) and the infrared thermal distribution across the ring laser [Chen–5] (fig.A.2.6), using a Barnes RM50 Infrared Microscanning Imager (2 to 5μm) [Wolfson laboratory, University of Birmingham]. The sample, with a Φ100μm ring of 2μm guide (fig.A.2.4) pumped with a 100mA current, was observed to produce a temperature drop between the heat sink and the top of the ring of 45°C, similar to the calculated value. The maximum temperatures within the ring were on the Y–junctions of the device, due to greater current concentration.

In a separate experiment, the temperature at various points of a 50μm wide and 400μm long stripe laser chip was measured, using small Au–Al wire thermocouples (section 3.7.2) insulated from the contacts with 200nm of SiO_2 (fig.A.2.7). The temperature of the laser was controlled with a Peltier cooling element. For D.C. pumping, the temperature drop across the laser wafer to the point on the top of the laser surface, 100μm away from the structure, depended on the current I as:

$$\Delta T[^{\circ}C] = 1.5 + 0.3 * I[mA] \qquad (A.2.11)$$

and the theoretically estimated temperature drop across the wafer to the junction was:

$$T_j - T_b = (1.5+0.3*I[mA])*1.25,\ R_{th}=160^{\circ}C/W; \qquad (A.2.12)$$

e.g. ΔT=12°C for I=25mA.

At currents higher than 30mA, the temperature increased considerable due to the limited heat sink capability.

The lasing wavelength of the standard ring laser device indicated a temperature drop across the wafer of 60 to 75°C for double heterostructures and of 10°C for quantum well devices (section 4.3.4).

The temperature drop across the rib and the substrate are catastrophic (fig.A.2.8) for higher power densities, narrow and high ribs (also section 5.2.4) and limited heat sink capability. The reduction of losses and thermal resistance may be achieved with

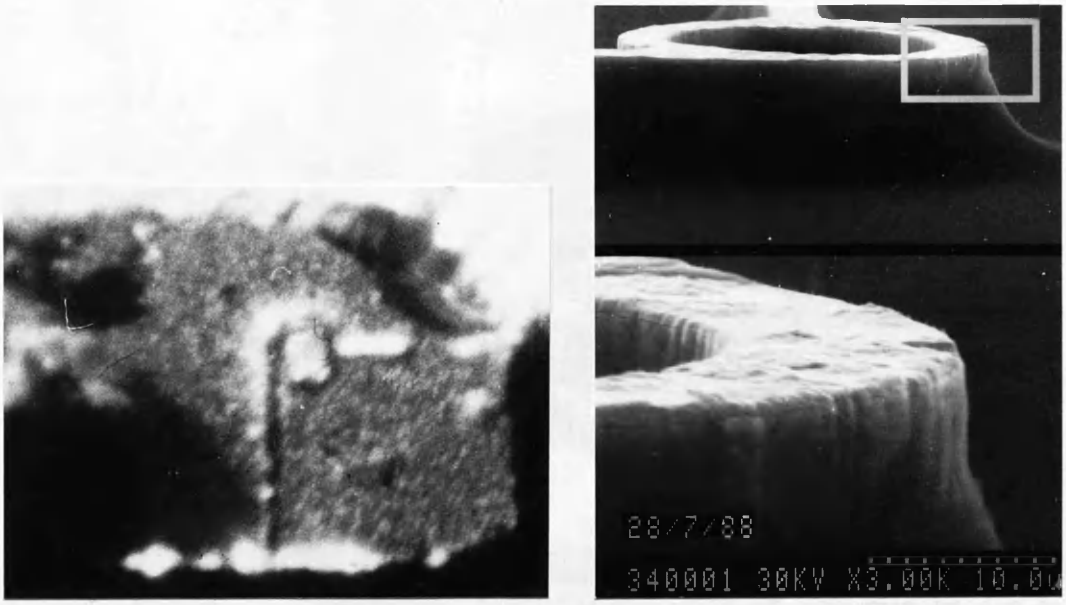

Fig.A.2.3. Polyimide embedded ring laser, similar to the one observed with a thermal imager.

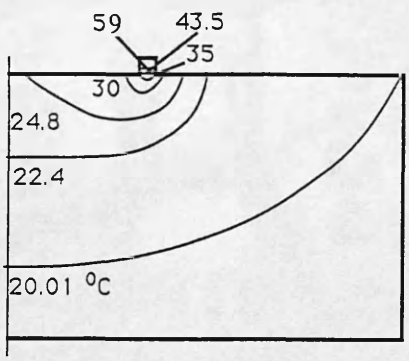

Fig.A.2.4. An example of a temperature distribution within a ring rib laser device [After Chen-4].

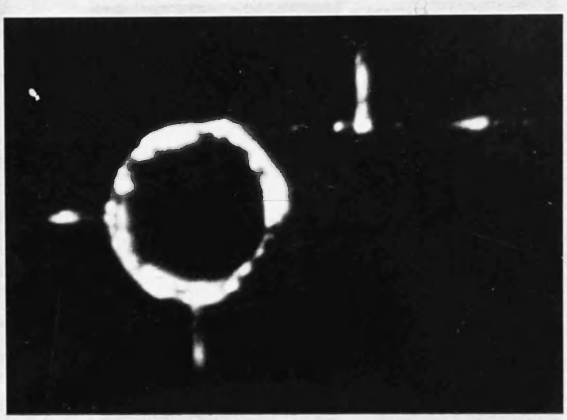

Fig.A.2.5. IR image of the photoluminescence of a 100μm diameter polyimide embedded ring laser.

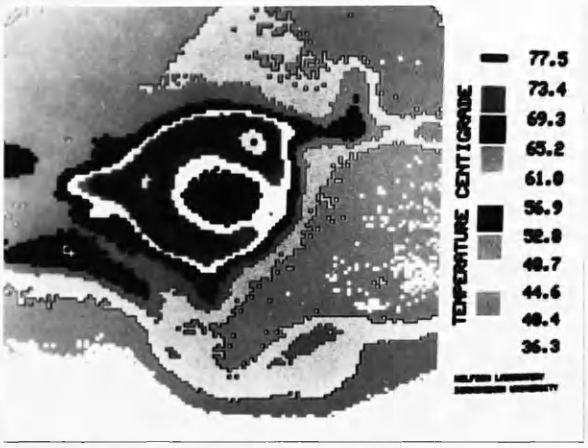

Fig.A.2.6. Thermal image of a 100μm diameter polyimide embedded ring laser. The increased temperature of the left hand–side of the measured ring may be due to a low thermally conductive epoxy (0.02W/cm^{o}C) placed on the left top corner of the chip (0.44W/cm^{o}C), and consequent heat dissipation problems.

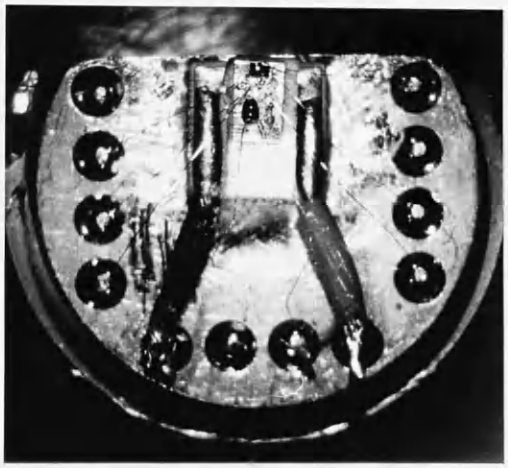

Fig.A.2.7. A temperature measurement system of the laser chip, using the Au–Al thermocouples.

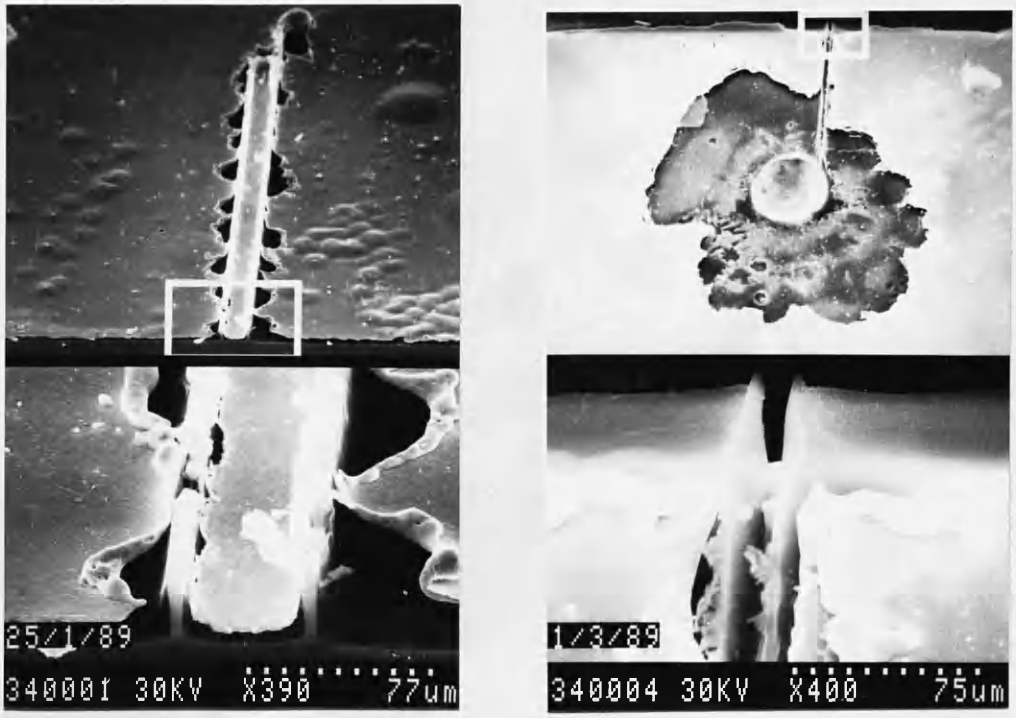

Fig.A.2.8. Damage to the semiconductor laser due to high power density within the narrow and high rib devices.

a low threshold current laser material, producing larger diameter devices made of wider guides e.g. 6μm guide of Φ100μm ring (314μm circumference) and reducing a rib height.

A. REFERENCES.

[1] Thompson G.H.B.: Physics of semiconductor laser devices, J.Wiley & Sons, (1980).

[2] Chinn S.R., Zory P.S., Reisinger A.R.: A model for GRIN–SCH–SQW diode lasers, IEEE JQE–24, 11, pp.2191–2214 (1988).

[3] Nakwaski W.: Dynamical thermal properties of stripe–geometry laser diodes, IEE Proc., 131, pp.49–102 (1984).

[4] Chen W.: Thermal problems in semiconductor ring lasers, B.Sc. thesis, Glasgow University (1989).

[5] Chen, W., Laybourn, P.J.R., Jezierski, A.F. and Webb, P.W.: Thermal characteristics of semiconductor ring laser sources for integrated optical sensor devices, Arditty H.J., Dakin J.P. & Kersten R.Th. (Eds.): Optical Fibre Sensors, Springer proc. in Physics, 44, pp.302–312, Heidelberg: Springer (1989). (Proceedings of 6th Optical Sensors Conference, Paris, (1989)).